NEW STRATEGIES FOR MAINTAINING POST-SEISMIC OPERATIONS OF LIFELINE CORRIDORS

PROJECT REPORT

by

David Trejo
André R. Barbosa
Tim Link
Oregon State University

Marc O. Eberhard
Charles W. Roeder
Dawn E Lehman
Max Stephens
Hung V. Tran
John F. Stanton
University of Washington

for

Pacific Northwest Transportation Consortium (PacTrans)
USDOT University Transportation Center for Federal Region 10
University of Washington
More Hall 112, Box 352700
Seattle, WA 98195-2700

Disclaimer

Technical Report Documentation Page

1. Report No.
2012-M-0001

2. Government Accession No.
01542816

3. Recipient's Catalog No.

4. Title and Subtitle
NEW STRATEGIES FOR MAINTAINING POST-SEISMIC OPERATIONS OF LIFELINE CORRIDORS

5. Report Date
October 14, 2014

6. Performing Organization Code
PACTRANS 12-03

7. Author(s)
David Trejo, André R. Barbosa, Tim Link, Marc O. Eberhard, Charles W. Roeder, Dawn E Lehman, Max Stephens, Hung V. Tran, John F. Stanton

8. Performing Organization Report No.
1-739437

9. Performing Organization Name and Address

PacTrans

Pacific Northwest Transportation Consortium, University Transportation Center for Region 10

University of Washington More Hall 112
Seattle, WA 98195-2700

Pacific Northwest Transportation Consortium (PACTRANS)

Oregon State University 101 Kearney Hall,
Corvallis, OR 97331

10. Work Unit No. (TRAIS)

11. Contract or Grant No.
DTRT12-UTC10

12. Sponsoring Organization Name and Address

United States of America

Department of Transportation

Research and Innovative Technology Administration

13. Type of Report and Period Covered
Research 10/1/2012-10/13/2014

14. Sponsoring Agency Code

15. Supplementary Notes
Report uploaded at www.pacTrans.org

16. Abstract

This project furthered the development of three strategies that could positively impact maintaining post-seismic operations of lifeline corridors. In Year 1, most of the focus was on the development of the three individual strategies. In Year 2, a follow-up project will include more formal assessments of the situation in which each strategy might be preferred.

The first part of the investigation, performed at Oregon State University, assessed the use of high strength reinforcement (HSS) for use in reinforced concrete (RC) columns. HSS is not currently allowed in RC due to lack of information on the material characteristics and lack of performance information when used in columns. But potential benefits in construction, performance, and economics justify the need for research, especially for critical corridors. Results indicate that a column constructed with Grade 80 HSS reinforcement performs similar to column constructed with conventional Grade 60 reinforcement.

The second part of the investigation, performed at the University of Washington, focused on a new type of connection between a precast concrete column and a cast-in-place drilled shaft. The column is precast with a roughened outer surface at the bottom of the column which will be embedded in the cast-in-place shaft. The connection can be built rapidly and allows generous construction tolerances. Building on two previous tests, a third quasi-static scaled connection test between a precast bridge column and a drilled shaft was performed to investigate the seismic performance of the new connection. The geometry of the test specimen was based on the minimum practical difference between the diameters of the shaft and the column, and so represented the most critical cases. The performance of the system was investigated up to a drift ratio of 10%. The experimental results showed that, if adequate confining steel is included in the splice zone, the plastic hinging mechanism forms in the column, without incurring damage in the splice zone or shaft. If the confinement is insufficient, the strength of the splice zone deteriorates rapidly with cyclic loading. Recommendations for transverse reinforcement in the transition area are provided to ensure desirable performance.

The third part of the investigation, also performed at the University of Washington, focused on the performance of concrete filled steel tubes (CFST), with specific focus on connections to precast concrete piers and piles caps. CFSTs have the potential to improve performance in seismic events and decrease overall costs. CFSTs may be used for bridge piers, shafts, caissons, and columns, but their use is limited because AASHTO design specifications for CFSTs are dated and few validated, constructible connections exist. Part 3 of this report (Part 3) compares current CFST design provisions to experimental results, noting limitations and deficiencies. Improved provisions proposed for the AASHTO specifications and partly based on the AISC provisions are summarized. CFST connections are also addressed. A foundation connection capable of developing the full composite capacity of a CFST was evaluated experimentally and initial study of CFST column-to-cap beam connections was conducted using numerical simulation. Both are effective in developing and transferring the full capacity of the CFST and are summarized.

17. Key Words
Seismic performance; high-strength steel; reinforced concrete; concrete filled steel tube.

18. Distribution Statement
No restrictions.

19. Security Classification (of this report)
Unclassified.

20. Security Classification (of this page)
Unclassified.

21. No. of Pages

22. Price
NA

Form DOT F 1700.7 (8-72) **Reproduction of completed page authorized**

EXECUTIVE SUMMARY

Following an earthquake, it is essential that critical corridors remain usable so that emergency responders can deliver aid, and if necessary, people can evacuate affected areas in reasonable times. The continued functionality of lifeline corridors is also critical to the economic recovery of a region subjected to an earthquake. The post-event functionality of lifeline corridors can be affected by many types of events (e.g., landslides), but most often, the functionality of the corridor depends strongly on the resilience of its bridges.

A team of researchers from Oregon State University and the University of Washington is developing and assessing new strategies for maintaining post-seismic operations of bridges in the Pacific Northwest (PNW). During Year 1, this team investigated three strategies that could positively impact maintaining post-seismic operations of bridges: (1) High-Strength Reinforcement in Bridge Columns , (2) Precast, Pretensioned Bridge Column Supported on Drilled Shafts, and (3) Concrete-Filled Tubes for Bridge Columns. The team members met by teleconference to discuss each other’s strategies and to exchange suggestions, but for the first year, most of the effort was devoted to the development of the three systems individually. A follow-up Pactrans project in Year 2 continues the development of the systems and explicitly includes the comparative evaluation of the three systems by the overall team.

High Strength Reinforcement in Bridge Columns (Part 1)

The first project of this overall program, performed at Oregon State University, assessed the use of high strength reinforcement (HSS) for use in reinforced concrete (RC) columns. HSS is not currently allowed in RC columns due to lack of information on the material characteristics and due to lack of performance information when used in RC columns. But potential benefits in construction, performance, and economics have been identified. These benefits justify the need for research, especially for bridges on critical corridors. This research investigated the performance of HSS (Grade 80 reinforcing bars) embedded in RC columns. Designs followed standard design methodologies used by State Highway Agencies (including AASHTO). Results indicate that a column constructed with Grade 80 HSS reinforcement performs similar to column constructed with conventional Grade 60 reinforcement. Additional columns are being tested and preliminary results indicate that the use of Grade 80 steel reinforcement may be acceptable with some modifications to the design codes.

Connection Between Precast Column and Drilled Shaft (Part 2)

A new type of connection between a precast concrete column and a cast-in-place drilled shaft has been developed for Accelerated Bridge Construction (ABC) in seismic regions. The column is precast with a roughened outer surface at the bottom of the column which will be embedded in the cast-in-place shaft. The connection can be built rapidly and allows generous construction tolerances.

Three quasi-static scaled connection tests between a precast bridge column and a drilled shaft were performed to investigate the seismic performance of the new connection. The geometry of the test specimens was based on the minimum practical difference between the diameters of the shaft and the column, and so represented the most critical cases. The performance of the system was investigated up to a drift ratio of 10%. The experimental results showed that, if adequate confining steel is included in the splice zone, the plastic hinging mechanism forms in the column, without incurring damage in the splice zone or shaft. If the confinement is insufficient, the strength of the splice zone deteriorates rapidly with cyclic loading. Recommendations for transverse reinforcement in the transition area are provided to ensure desirable performance.

Concrete-Filled Tubes (Part 3)

Concrete-filled steel tubes (CFSTs) consist of a steel tube with concrete infill, and have increased strength, stiffness, and deformability relative to a comparably sized reinforced concrete column. The steel is at its optimal location, thus maximizing strength and stiffness while minimizing weight and material requirements. The concrete infill is confined by the steel tube, resulting in an increased strength and strain capacity of the concrete; in turn, the infill delays local and global buckling of the tube. In addition to their high resistance and stiffness properties, CFSTs are easily and rapidly constructed, eliminating the need for formwork and reinforcement.

In bridge design, CFSTs may be used for bridge piers, shafts, caissons, and columns. However, their use is limited in part because AASHTO design specifications for CFSTs are dated and in part because few validated, constructible connections exist. Relative to AASHTO, AISC includes more recent updates to CFST design provisions. This report compares current CFST design provisions to experimental results, noting limitations and deficiencies. Proposed provisions, which are improvements on the AISC provisions, are introduced. These improved provisions are used as the basis of new AASHTO specifications for use of CFST in bridge design. As noted, a second limitation in CFST design is the connections. This is also addressed herein. A foundation connection capable of developing the full composite capacity of a CFST was evaluated experimentally, resulting in design expressions; both are presented in the report. A preliminary study of CFST column-to-cap beam connections was conducted using numerical simulation. Both are effective in developing and transferring the full capacity of the CFST. In its totality this part of the report presents significant advancement and practical methods for use of CFST in bridge design.

PART 1:

SEISMIC PERFORMANCE OF REINFORCED CONCRETE BRIDGE COLUMNS CONSTRUCTED WITH GRADE 80 REINFORCEMENT

Table of Contents: Part 1

List of Figures: Part 1

List of Tables: Part 1

List of Symbols: Part 1

a = Depth of compression zone in the column cross section (in, mm)

a_1 = Angle of compression strut s1 measured from the horizontal (degrees)

A_{1A} = Area under bearing device for step 6-A of the footing design (in^2, mm^2)

A_{1B} = Area under bearing device for step 6-B of the footing design (in^2, mm^2)

A_{1C} = Area under bearing device for step 6-C of the footing design (in^2, mm^2)

a_2 = Angle of compression strut s2 measured from the horizontal (degrees)

A_{2A} = A notational area defined by AASHTO LRFD Bridge Design Specifications 6th Ed. Sec. 5.7.5 for step 6-A of the footing design (in^2, mm^2)

A_{2B} = A notational area defined by AASHTO LRFD Bridge Design Specifications 6th Ed. Sec. 5.7.5 for step 6-B of the footing design (in^2, mm^2)

A_{2C} = A notational area defined by AASHTO LRFD Bridge Design Specifications 6th Ed. Sec. 5.7.5 for step 6-C of the footing design (in^2, mm^2)

a_3 = Angle of compression strut s3 measured from the horizontal (degrees)

a_4 = Angle of compression strut s4 measured from the horizontal (degrees)

a_5 = Angle of compression strut s5 measured from the horizontal (degrees)

a_6 = Angle of compression strut s6 measured from the horizontal (degrees)

A_b = Area of individual reinforcing steel bar (in^2, mm^2)

A_c = Area of core measured to the outside diameter of the spiral (in^2, mm^2)

A_{cs1} = Conservative approximate area of compressive strut s1 (in^2, mm^2)

A_{cs2} = Conservative approximate area of compressive strut s2 (in^2, mm^2)

A_{cs3} = Conservative approximate area of compressive strut s3 (in^2, mm^2)

A_{cs4} = Conservative approximate area of compressive strut s4 (in^2, mm^2)

A_{cs5} = Conservative approximate area of compressive strut s5 (in^2, mm^2)

A_{cs6} = Conservative approximate area of compressive strut s6 (in^2, mm^2)

A_{dyw} = Area of Dywidag bar (in^2, mm^2)

A_e = Effective shear cross-sectional area (in^2, mm^2)

A_g = Gross cross-sectional area of column (in^2, mm^2)

A_{sl} = Cross-sectional area of longitudinal reinforcement (in^2, mm^2)

A_{st} = Cross-sectional area of transverse reinforcement (in^2, mm^2)

A_{st1} = Required area of steel for tie t1 (in^2, mm^2)

A_{st2} = Required area of steel for tie t2 (in^2, mm^2)

A_{st3} = Required area of steel for tie t3 (in^2, mm^2)

A_{st4} = Required area of steel for tie t4 (in^2, mm^2)

A_v = Area of shear reinforcement perpendicular to flexural tension reinforcing (in^2, mm^2)

b_f = Footing width (ft, m)

b_h = Width of reinforced concrete header (in, mm)

b_{s1} = Width of compression strut s1 (in, mm)

b_{s2} = Width of compression strut s2 (in, mm)

b_{s3} = Width of compression strut s3 (in, mm)

b_{s4} = Width of compression strut s4 (in, mm)

b_{s5} = Width of compression strut s5 (in, mm)

b_{s6} = Width of compression strut s6 (in, mm)

b_v = Effective web width taken as the minimum web width, measured parallel to the neutral axis, between the resultants of the tensile and compressive forces due to flexure, or for circular sections, the diameter of the section, modified for the presence of ducts where applicable (in, mm)

C_1 = Internal column compression force resulting by the applied axial load (kips, kN)

C_2 = Internal column compression force resulting by the horizontal actuator force (kips, kN)

C_c = Internal column compression force (kips, kN)

c_c = Column concrete clear cover (in, mm)

c_{cf} = Footing clear cover (in, mm)

c_{ch} = Concrete clear cover of the reinforced concrete header (in, mm)

C_{sf} = Resultant compression force from the strong floor (kips, kN)

c_{smin} = Minimum spiral clear spacing defined by AASHTO LRFD Bridge Design Specifications 6th Ed. Sec. 5.10.6.2 (in, mm)

D' = Cross-sectional diameter of confined concrete core measured between the centerline of the peripheral hoop or spiral (in, mm)

d_1 = Distance from column internal tension force to nearest edge of column (in, mm)

d_2 = Distance between column internal tension and compression forces (in, mm)

D_b = Nominal diameter of reinforcing bar (in, mm)

D_{bl} = Nominal diameter of longitudinal reinforcing bar (in, mm)

D_{bt} = Nominal diameter of transverse reinforcing bar (in, mm)

D_c = Column diameter (ft, m)

D_{cc} = Diameter of column core, measured out-to-out of spiral (in, mm)

D_{dyw} = Diameter of Dywidag bar (in, mm)

d_e = Effective depth from extreme compression fiber to the centroid of the tensile force in the tensile reinforcement (in, mm)

D_r = Diameter of the columns core, taken from center-to-center of longitudinal reinforcement (in, mm)

D_{sl} = Diameter of longitudinal rebar (in, mm)

d_v = Effective shear depth taken as the distance, measure perpendicular to the neutral axis, between the resultants of the tensile and compressive forces due to flexure; it need not be taken to be less than the greater of 0.9 d_e or 0.72 (in, mm)

e_M = Eccentricity caused by the applied external moment (ft, m)

F_A = Horizontal force applied by the actuator (kips, kN)

f'_c = Nominal compressive strength of concrete (psi, MPa)

f_{cus1} = Limiting concrete compressive stress for design by strut-and-tie model for strut s1 (ksi, Mpa)

f_{cus2} = Limiting concrete compressive stress for design by strut-and-tie model for strut s2 (ksi, Mpa)

f_{cus3} = Limiting concrete compressive stress for design by strut-and-tie model for strut s3 (ksi, Mpa)

f_{cus4} = Limiting concrete compressive stress for design by strut-and-tie model for strut s4 (ksi, Mpa)

f_{cus5} = Limiting concrete compressive stress for design by strut-and-tie model for strut s5 (ksi, Mpa)

f_{cus6} = Limiting concrete compressive stress for design by strut-and-tie model for strut s6 (ksi, Mpa)

F_{ff} = Horizontal friction force action on the bottom surface of the footing (kips, kN)

F_{s1} = Force in compression strut s1 (kips, kN)

F_{s2} = Force in compression strut s2 (kips, kN)

F_{s3} = Force in compression strut s3 (kips, kN)

F_{s4} = Force in compression strut s4 (kips, kN)

F_{s5} = Force in compression strut s5 (kips, kN)

F_{s6} = Force in compression strut s6 (kips, kN)

F_{t1} = Force in tension tie t1 (kips, kN)

F_{t2} = Force in tension tie t2 (kips, kN)

F_{t3} = Force in tension tie t3 (kips, kN)

F_{t4} = Force in tension tie t4 (kips, kN)

f_{ydyw} = Nominal yield stress of Dywidag bar (ksi, Mpa)

f_{yl} = Nominal yield stress of the longitudinal reinforcing steel (ksi, Mpa)

f_{yt} = Nominal yield stress of transverse column reinforcement (hoops/spirals) (ksi, Mpa)

h_c = Column test height (ft, m)

h_f = Footing height (ft, m)

h_h = Reinforced concrete header height (ft, m)

L_{s1} = Length of compression strut s1 (in, mm)

L_{s2} = Length of compression strut s2 (in, mm)

L_{s3} = Length of compression strut s3 (in, mm)

L_{s4} = Length of compression strut s4 (in, mm)

L_{s5} = Length of compression strut s5 (in, mm)

L_{s6} = Length of compression strut s6 (in, mm)

m_A = Modification factor for step 6-A of the footing design

m_B = Modification factor for step 6-B of the footing design

m_C = Modification factor for step 6-C of the footing design

MSA = Maximum size aggregate (in, mm)

M_e = Expected moment capacity (kip-ft, kN-m)

M_n = Nominal moment capacity (kip-ft, kN-m)

n = Number of spirals in the structural member

n_{bf} = Number of reinforcing steel bars per direction in the footing, for both top and bottom mats of reinforcement

n_{dywfV} = Number of vertical Dywidag threaded bars used per end of the footing

N_f = Normal force acting on bottom surface of the footing (kips, kN)

n_{t1} = Required number of bars for tie t1

n_{t2} = Required number of bars for tie t2

n_{t3} = Required number of bars for tie t3

n_{t4} = Required number of bars for tie t4

P = Applied axial load on column (kips, kN)

P_d = Dead load resulting from reinforced concrete header and column self-weight (kips, kN)

P_{nA} = Nominal bearing resistance for step 6-A of the footing design (kips, kN)

P_{nB} = Nominal bearing resistance for step 6-B of the footing design (kips, kN)

P_{ns1} = Nominal resistance of a compressive strut s1 (kips, kN)

P_{ns2} = Nominal resistance of a compressive strut s2 (kips, kN)

P_{ns3} = Nominal resistance of a compressive strut s3 (kips, kN)

P_{ns4} = Nominal resistance of a compressive strut s4 (kips, kN)

P_{ns5} = Nominal resistance of a compressive strut s5 (kips, kN)

P_{ns6} = Nominal resistance of a compressive strut s6 (kips, kN)

P_{r1} = Factored axial resistance of strut s1 (kips, kN)

P_{r2} = Factored axial resistance of strut s2 (kips, kN)

P_{r3} = Factored axial resistance of strut s3 (kips, kN)

P_{r4} = Factored axial resistance of strut s4 (kips, kN)

P_{r5} = Factored axial resistance of strut s5 (kips, kN)

P_{r6} = Factored axial resistance of strut s6 (kips, kN)

s = Spacing of shear/transverse reinforcement measure along the longitudinal axis of the structural member (in, mm)

s_{bbf} = Center to center bar spacing for tension tie rebar of the bottom mat of the foundation (in, mm)

s_{bf} = Footing center-to-center bar spacing, for both top and bottom mats of reinforcement (in, mm)

s_{max} = Maximum spiral spacing/pitch (in, mm)

s_{min} = Minimum spiral spacing/pitch (in, mm)

s_{tbf} = Center to center bar spacing for tension tie reinforcement of the top mat for the foundation (in, mm)

T_1 = Internal column tension force caused by the applied axial load (kips, kN)

T_2 = Internal column tension force caused by the horizontal actuator force (kips, kN)

T_c = Internal column tension force (kips, kN)

T_{dywf} = Resultant tension force from vertical Dywidag bars per end of the footing (kips, kN)

v_c = Permissible shear stress carried by concrete (ksi, MPa)

V_c = Nominal shear strength provided by concrete (kips, kN)

V_e = Expected peak shear force (kips, kN)

V_n = Nominal shear force (kips, kN)

V_p = Component in the direction of the applied shear of the effective prestressing force; positive if resisting the applied shear; Vp = 0 when AASHTO LRFD Bridge Design Specifications 6th Ed. Article 5.8.3.4.3 is applied (kips, kN)

V_s = Nominal shear strength provided by shear reinforcement (kips, kN)

v_u = Factored shear stress (ksi, Mpa)

V_u = Factored shear force (kips, kN)

V_{uA} = Factored shear force demand according to AASHTO LRFD Bridge Design Specifications 6th Ed. Sec. 5.8.2.9 (kip, N)

x_C = Distance from internal compression resultant force to column centroid (in, mm)

x_{Csf} = Horizontal distance from the center of the column to the resultant compression force from the strong floor (ft, m)

x_T = Distance internal tension resultant force to column centroid (in, mm)

x_{Tdywf} = Horizontal distance from the center of the column to the location of the vertical Dywidag tie down bars in the footing (in, mm)

α' = Concrete shear stress adjustment factor

e_{1s1} = Principal tensile strain in cracked concrete of strut s1 due to factored loads (in/in, mm/mm)

e_{1s2} = Principal tensile strain in cracked concrete of strut s2 due to factored loads (in/in, mm/mm)

e_{1s3} = Principal tensile strain in cracked concrete of strut s3 due to factored loads (in/in, mm/mm)

e_{1s4} = Principal tensile strain in cracked concrete of strut s4 due to factored loads (in/in, mm/mm)

e_{1s5} = Principal tensile strain in cracked concrete of strut s5 due to factored loads (in/in, mm/mm)

e_{1s6} = Principal tensile strain in cracked concrete of strut s6 due to factored loads (in/in, mm/mm)

e_{s1} = Tensile strain in the cracked concrete at strut s1 in the direction of the tension tie (in/in, mm/mm)

e_{s2} = Tensile strain in the cracked concrete at strut s2 in the direction of the tension tie (in/in, mm/mm)

e_{s3} = Tensile strain in the cracked concrete at strut s3 in the direction of the tension tie (in/in, mm/mm)

e_{s4} = Tensile strain in the cracked concrete at strut s4 in the direction of the tension tie (in/in, mm/mm)

e_{s5} = Tensile strain in the cracked concrete at strut s5 in the direction of the tension tie (in/in, mm/mm)

e_{s6} = Tensile strain in the cracked concrete at strut s6 in the direction of the tension tie (in/in, mm/mm)

φ = Strength reduction factor

φ_{dyw} = Strength reduction factor applied to Dywidag bars

φ_{stm} = Strength reduction factor for compression forces in the strut and tie model, AASHTO LRFD Bridge Design Specifications 6th Ed. Sec. 5.5.4.2

λ = Moment over strength factor, to account for the increased moment capacity due to the increase in the actual material strengths compared to their nominal strengths

γ_c = Specific weight of reinforced concrete (lb/ft^3, kg/m^3)

ρ_l = Ratio of area of longitudinal reinforcement to gross area of concrete

ρ_t = Ratio of volume of spiral or hoop reinforcement to the core volume confined by the spiral or hoop reinforcement (measured out-to-out)

μ_D = Global displacement ductility demand ratio

μ_s = Conservative approximation of the static friction coefficient for concrete sliding on concrete

Acknowledgments

As with all projects, the success of the project is dependent on many dedicated people. We would like to thank Michael Dyson, James Batti, and Manfred Dittrich for their assistance in fabricating and testing the specimens. Students that assisted with the project include Jiaming Chen, Nicolas Matus, Greg Hendrix, Cody Tibbits, Lapyote Prasittisopin, Yicheng Long, Frank Porter, Amy Kordoska, and Drew Nielson. The assistance of Dana Ainsworth, our expert in all things financial, is duly noted. Special thanks to Thomas Murphy and Dennis Laubar from Cascade Steel (McMinnville, OR) for producing a special heat of the Grade 80 steel reinforcement. The authors sincere thank all those that assisted with the project.

Chapter 1

INTRODUCTION

1.1 Project Objective

Although high strength steel (HSS) reinforcement is commercially available, its use is limited. Current codes do not allow HSS reinforcement in plastic hinge regions (i.e., bridge columns). In general, higher steel strengths exhibit lower ductility. However, Grade 80 (80 ksi [550 MPa]) reinforcing steel (considered herein as HSS) meeting ASTM A706 has been reported to have adequate ductility. Even with these reports, there is an overall lack of data on the performance of reinforced concrete (RC) members fabricated with Grade 80 reinforcement. Therefore, the objective of this study is to assess the behavior of circular reinforced-concrete bridge columns constructed with Grade 80 (80 ksi [550 MPa]) reinforcing steel meeting ASTM A706 specifications subjected to reversed cyclic lateral loading.

1.2 Report Outline

This report includes 8 chapters. A brief description of the chapters follows.

1.2.1 Chapter 1

This chapter provides a general introduction to the overall HSS project and provides a brief overview of each chapter in the report.

1.2.2 Chapter 2

This chapter provides a brief literature review for the project. The literature review covers the history of Grade 80 reinforcement, a summary of the use of Grade 80 reinforcement reported in the code documents, and an overview of the performance of systems containing high HSS.

1.2.3 Chapter 3

Chapter 3 provides details on the experimental program and specimen design. This chapter includes details on the design for bending moment capacity, transverse reinforcement design, RC header design, and RC footing design. The chapter also contains details for the instrumentation of the specimens. This chapter also includes specifics on the test setup and testing procedure. Lastly it provides details on the construction of the test specimens.

1.2.4 Chapter 4

This chapter provides details on the materials used in the construction of the test specimens. The chapter is separated into two main sections: steel and concrete. The steel section provides mill sheet data for the reinforcement as well as material testing results from the materials testing program in this research. The section on concrete materials provides details on the concrete mix proportions and test results for the concrete.

1.2.5 Chapter 5

This chapter presents the experimental results of columns C1 and C2. Although limited preliminary analyses were performed on the raw data, no comparisons between the performance of columns C1 and C2 were made in this chapter. Items presented in this chapter include visual observations of cracking, concrete spalling, reinforcing bar buckling, reinforcing bar fracture, steel reinforcing strains, column curvature, column tilt, applied horizontal load, axial load, and footing displacements.

1.2.6 Chapter 6

This chapter presents the analysis of the experimental data collected in Chapter 5. The objective of this chapter is to compare columns C1 and C2 and determine the effects of using

Grade 80 reinforcement. The items presented in Chapter 5 are further discussed in this chapter along with energy dissipation, displacement ductility, and curvature ductility.

1.2.7 Chapter 7

This chapter presents an overview of a model of the columns developed using OpenSees. The models can be used to predict performance of RC columns reinforced with either Grade 60 or Grade 80 reinforcement.

1.2.8 Chapter 8

This chapter provides a summary and conclusion of the research.

Chapter 2

LITERATURE REVIEW

2.1 History of Grade 80 Reinforcement

The first specifications for reinforcing bar were developed by the American Association of Steel Manufacturers in 1910 (Concrete Reinforcing Steel Institute [CRSI] 2001). The following year the American Society for Testing and Materials (ASTM) adopted standard specification A15 for billet steel reinforcement, which, for structural grade reinforcement, required a yield strength of 33,000 psi (228 Mpa) (CRSI 2001). In 1959, the American Society for Testing and Materials (ASTM) developed specifications for reinforcing bars with yield strengths of 60 ksi (414 MPa) and 75 ksi (520 MPa) (Gustafson 2010). In 1967, Hognested gave a presentation at the CRSI Fall Business Meeting emphasizing that Grade 80 reinforcement needed to be produced and that it would soon be in demand (Gustafson 2010). It took several decades for the Grade 80 reinforcement to make its way into the standards. Gustafson (2010) reported that the allowable compressive strains in vertical reinforcement was limited to 0.40%f_y, and could not to exceed 30 ksi (207 MPa). This translated to a maximum allowable yield strength of 30/0.40, or 75 ksi.

In 1976, Rice and Gustafson (1976) assessed the effects of Grade 80 reinforcement in structural elements for buildings using code provisions at that time (Rice and Gustafson 1976). However, at that time an ASTM specification for Grade 80 steel reinforcement did not exist and Grade 80 reinforcing bars were not produced (Rice and Gustafson 1976). The study found that many code requirements restricted or prohibited the use of Grade 80 reinforcement. Through moment interaction diagrams the Rice and Gustafson (1976) showed that columns reinforced with Grade 80 reinforcing bars had a significant increase in moment capacity compared to columns reinforced with Grade 60 reinforcing bars when loaded dominantly in flexure. The authors also conducted an economic analysis and reported that the use of Grade 80 reinforcement could have a significant reduction in cost if large quantities were manufactured.

Due to the encouragement from structural engineers, contractors, bar producers and fabricators ASTM included specification to *ASTM A706/706M–13 Standard Specification for Low-Alloy Steel Deformed and Plain Bars for Concrete Reinforcement* for reinforcing bars with a minimum yield strength of 80 ksi (550 MPa) in December 2009 (Gustafson 2010). The encouragement was due to the fact that higher strength reinforcement could improve constructability by reducing the congestion of reinforcement in earthquake-resistant structures (Gustafson 2010).

2.2 High Strength Steel Material

ASTM A706/A706M provides standard specifications for bars with a minimum yield strength of 80 ksi (550 MPa) (ASTM 2012). The chemical composition requirements are the requirements specified for A706 Grade 60 reinforcement. Besides strength requirements, Grade 80 reinforcement requires a 2% lower minimum elongation for bar sizes 3, 4, 5, and 6 and requires a slightly larger pin diameter for the bend test requirements.

The yield strength is a critical design parameter for reinforced concrete elements. Paulson (2013) reported three main methods for measuring yield stress. These include:

(1) Observed Yield Point (YP), which defines the yield stress as the perfect-plastic horizontal portion of the stress-strain curve. This method is only acceptable for reinforcing steel that exhibits sharp yielding, where the stress-strain curve is

elastic, perfectly-plastic. ASTM A-15 Grade 40 (40 ksi [280 MPa]) reinforcement exhibited this behavior.

(2) Offset Method (OM), which specifies an offset of the elastic region of the stress-strain curve. The offset was initially specified as 0.1% but was later increased to 0.2%. This method was developed for more rounded stress-strain curves for which the YP method did not apply.

(3) Extension Under Load (EUL), which has a specified strain value under load. In this method, the stress corresponding to a strain value is defined as the yield stress. This method was initially recommended in 1967 by an ad-hoc group to replace the 0.1% offset method with a series of EUL strains. This was due to the lack of specialty instrumentation to make offset strain measurements on the reinforcing bars at the rolling mills.

ASTM A706 requires the use of the OM with a 0.2% strain offset and this is defined in ASTM A370-12a *Standard Test Methods and Definitions for Mechanical Testing of Steel Products* for reinforcing steel not exhibiting a “sharp-kneed or well defined type of yield point.” ASTM A706 also allows the user to determine yield following EUL. The standard states “the stress corresponding to a tensile strain of 0.0035 shall be a minimum of 60 000 psi [420 MPa] for Grade 60 [420] and a minimum of 80 000 psi [550 MPa] for Grade 80 [550].”

The general process of making reinforcing bars starts by processing scrap steel. This scrap steel along with added alloys is melted in a large vat and formed into billets. Billets are typically cooled and stored. Later, these billets are reheated and then pulled through dies, forming desired reinforcing bar sizes.

Two properties of reinforcing bars, strength and ductility, are directly related, by definition. An increase in the steel strength typically reduces the ductility and softens the strain hardening region of the stress-strain curve. Thus, most steel grades are a compromise between the desired strength and ductility (Selzer 2013).

Micro-alloying, the addition of specific alloys in small percentages can be used to induce grain refinement and strength of reinforcing steel. Specific alloy types can include niobium, vanadium, titanium, molybdenum, and other rare earth metals. During processing, steel develops grains that grow as the steel solidifies and cools. Micro-alloys that result in a larger number of smaller grains will increase the strength of the steel (Selzer 2013). However, micro-alloying decreases ductility of the steel, but not nearly as much as a conventional alloys (Selzer 2013). Vanadium is a commonly used micro-alloy (Selzer 2013). Vanadium carbide particles form and "pin" the grain boundaries, resulting in smaller grains (Nissen 2013). This "chemical grain refinement" tends to make the stress-strain curve rounder compared to conventional alloys. Selzer (2013) reported that the ductility trade-off for increased strength is reduced. Grain refinement can also be accomplished with the rolling/forming process. This process breaks down grains and allows them to regrow as smaller grains as the steel cools (Selzer 2013). Grain refinement is also affected by thermal conditions—high reheating temperatures induce grain growth, resulting in larger grains (Selzer 2013).

Micro-alloying requires a controlled cool after rolling. Selzer (2013) reported an ideal cooling rate of approximately 300 ^{o}F/min (149 ^{o}C/min) for maximizing strength gains. If the cooling rate is too slow, newly formed grains grow after forming, coarsening the grain structure, which results in lower strengths. If the cooling rate is too fast precipitates remain in solution, reducing the effectiveness of the micro-alloy (Selzer 2013). In mill production of reinforcing bars, smaller bar sizes are rolled more times than larger bar sizes, producing additional grain refinement. Increased rolling results in more rounded stress-strain curves in smaller bars sizes compared to larger bar sizes (Selzer 2013). Heat-treating bars generally tends to increase the yield strength faster than the tensile strength, resulting in a lower tension to yield ratio (T/Y) values (Selzer 2013). ASTM A706 reinforcing steel requires a T/Y ratio of 1.25. Grade 80 reinforcement strengths are achieved by using existing processes for producing Grade 60 reinforcement plus the addition of micro-alloys (Nissen 2013).

Producers of reinforcing steel have to consider requirements for both minimum and maximum yield strengths, ultimate tensile strengths, and elongations. Therefore, the reinforcing steel producers typically produce an average strength larger than three standard deviations to ensure that the bars produced meet minimum specified values. The key is to produce reinforcing bars with higher strengths, while still having the desired ductility levels and low-cycle fatigue performance.

Mander et al. (1994) reported on a study on the low-cycle fatigue behavior of conventional ASTM A615 Grade 40 ([40 ksi] 280 MPa) reinforcing bars and ASTM A722 Grade 157 (157 ksi [1080 MPa]) high-strength prestressing threaded bars. All bars were tested as-received to better represent and simulate their seismic behavior in structural concrete members. The researchers concluded that a stress greater than yield can be sustained over the entire compression range if the lateral support spacing is less than or equal to six longitudinal bar diameters in confined structural concrete members (Mander et al. 1994). If the spacing is larger than this then the reinforcing bars yield (Mander et al. 1994). The six longitudinal bar diameter spacing may prove to be an ultimate limit controlling the spacing of HSS reinforcement used as transverse reinforcement, but research is needed. Mander et al. (1994) also reported that the peak cycle stress dropped quickly in the first few cycles (softening occurs) for the high-strength prestressing bars, while the Grade 40 exhibited hardening over the first few cycles. This may provide insight on the use of HSS reinforcing bars. The test results indicate that the displacement ductility (e_{su}/e_y) of the HSS threaded bar is only 17% of the deformed mild-steel bar. This is likely a large contribution to the specification limits on the strength of reinforcing bars. However, the researchers made conclusions for the prestressing threaded bar (i.e., HSS). It should be noted that these bars are designed for ultimate tensile strengths and not yield properties. This indicates that HSS deformed bar designed for both ultimate and yield strengths has potential as a reinforcement for concrete if the desired displacement ductility can be achieved. The test results also indicated that HSS exhibited superior energy dissipation capacity when compared to the conventional strength steel (Mander et al. 1994). Although promising, the energy dissipation is also a function of the number of reinforcing bars. One objective of using HSS reinforcement could be to reduce the amount of reinforcing bars needed—reducing reinforcing bars could result in reduced energy dissipation. Further research is needed.

Dodd and Restrepo-Posada (1995) reported that the tension and compression cyclic stress-strain behavior of reinforcement is symmetric up to necking (point of plastic instability). The modulus of elasticity of mill produced steel reinforcement is reduced after the steel has been strained beyond the elastic limit—this is known as the Bauschinger effect (Bauschinger 1887). Dodd and Restrepo-Posada (1995) concluded that the shape of the Bauschinger effect is not dependent on the monotonic stress-strain curve. However the researchers did conclude that the shape of the Bauschinger effect is dependent on carbon content—an increase in carbon content softens (less bilinear) the Bauschinger curve. This is an important finding when assessing the effect of HSS. Historically, a common approach to increase the strength of the steel was to add more carbon.

Rodriguez et al. (1990) conducted a study expanding on the work of Dodd and Restrepo-Posada. The researchers further investigating the effects of buckling in the reverse cyclic loading of steel reinforcing bars. Longitudinal reinforcing steel in RC structural elements may undergo large tension and compression strain reversals during strong earthquakes (Rodriguez et al. 1999). If insufficient tie spacing exists and this is combined with large tension and compression strain reversals progressing into the inelastic range, buckling of longitudinal reinforcing bars can occur (Rodriguez et al. 1999). The researchers concluded that the onset of buckling of a reinforcing bar subjected to cyclic loading may occur after a reversal from tension and is dependent of the maximum value of the tensile strain prior to the reversal. When this occurs, buckling of the reinforcing bar is believed to occur on the tension side of the hysteresis cycle (Rodriguez et al. 1999). An important finding of the research was that the maximum available curvature could be overestimated when buckling is not included in the compression stress-strain steel model for a reinforced concrete element (Rodriguez at al. 1999). This indicates that the increased tensile capacity of the bar may not be fully utilized due to effect of buckling, which controls the fracture strain under reversed cyclic loading. Further research is needed.

2.3 ASTM A706 Grade 80 Reinforcement in Code Documents

Provisions for Grade 80 were added to the ASTM A706/A706M in December 2009. Since then state and federal codes have been adjusting their provisions to account for the new ASTM A706 Grade 80 reinforcement. The use of Grade 80 reinforcement has not yet been approved for use in columns, or more specifically members designed to plastically hinge. The following sections provide an overview of existing codes on the use of Grade 80 steel reinforcement.

2.3.1 2004 ODOT Bridge Design and Drafting Manual

The Oregon Department of Transportation’s (ODOT’s) Bridge Design and Drafting Manual (BBDM 2012) allows the use of A706 Grade 80 in bridge decks, drilled shafts, crossbeams and end beams, but specifically states “do not use A706 Grade 80 reinforcement in members designed for plastic seismic performance (such as bridge columns).” In this document, however, ODOT acknowledges that A706 Grade 80 reinforcement has similar ductility properties compared to Grade 60 reinforcement. It is reported that ODOT does not allow the use of A706 Grade 80 in members designed for plastic seismic performance due to a lack of testing of reinforcing bars and of full-scale structural elements (ODOT 2012).

ODOT also limits the maximum yield strength of spirals to 60 ksi (420 MPa) for determining the spiral pitch (ODOT 2012). Allowing a yield strength of spirals equal to 80 ksi (550 MPa) could potentially increase the spiral pitch resulting in a longer unbraced length of reinforcing bar after the column concrete cover spalls. Because bar buckling may govern, the increase in strength may not compensate for the increase in the braced length. Design modifications may be necessary.

2.3.2 AASHTO Load and Resistance Factor Design (LFRD) Bridge Design Specifications

The American Association of State Highway and Transportation Officials (AASHTO) LFRD Bridge Design Specifications (2012) limits the yield strength used for design purposes to 75.0 ksi (520 MPa). AASHTO limits the design strength of transverse reinforcement to the stress corresponding to a strain of 0.0035 and not to exceed 75 ksi (AASHTO 2012). Although not reported, these are likely a result of insufficient data on performance. Further research is needed.

2.3.3 AASHTO Guide Specifications for LRFD Seismic Bridge Design

Section 8.4.1 of the AASHTO Guide Specifications for LFRD Seismic Bridge Design (2012) states that reinforcing steel used for Seismic Design Categories (SDC) B, C, and D can have an ultimate tensile strength of up to 250 ksi (1,720 MPa) as long as it can be demonstrated through testing that the low-cycle fatigue properties are equal to or better than conventional grade reinforcement allowed by the code. AASHTO (2012) also requires A706 reinforcement to be used in any member where plastic hinging is expected for SDC D. This would prevent the use of all high strength steels except for ASTM A706 Grade 80 in elements such as bridge columns where plastic hinges are expected to form. Although technically, it seems as though Grade 80 reinforcement meeting ASTM A706 specifications is allowed, Grade 80 reinforcement has not been used due to lack of performance data.

2.3.4 Other State Highway Agencies

The Washington Department of Transportation (WSDOT) has nearly identical restrictions as ODOT on the use of A706 Grade 80 reinforcing bars (WSDOT 2012). The WSDOT Bridge Design Manual states "ASTM A706 Grade 80 reinforcing steel shall not be used for elements and connections that are proportioned and detailed to ensure the development of significant inelastic deformations for which moment curvature analysis is required to determine the plastic moment capacity of ductile concrete members and expected nominal moment capacity of capacity protected members." This statement describes members designed for inelastic seismic performance. WSDOT does not allow the use of Grade 80 reinforcing bars in these members due to a lack of research establishing the shape, model, and characteristic values of the stress-strain curve. Furthermore, there is also a lack of data on the expected reinforcing strengths and strain limits for concrete components constructed with ASTM A706 Grade 80 reinforcing steel (WSDOT 2012).

The California Department of Transportation (Caltrans) Seismic Design Criteria (SDC) Version 1.6 limits the range of the yield stress of ASTM A706 to between 60 ksi (420 MPa) and

78 ksi (540 MPa) in the *Materials Properties for Concrete Components* (CALTRANS 2012). This statement prohibits the use of ASTM A706 Grade 80 reinforcing steel (which is required to have a minimum yield stress of 80 ksi (550 MPa)).

2.4 Performance of Systems with HSS

2.4.1 Columns with Low Longitudinal Reinforcement Ratios

Priestley and Benzoni (1996) conducted a study to investigate the seismic performance of circular columns with low longitudinal reinforcement ratios. The researchers tested two 0.4:1 scale 24-inch diameter, 72-inch tall circular columns. One column had the minimum longitudinal reinforcement ratio of 1% and one column had a longitudinal reinforcement ratio of 0.5% (this is one-half of the minimum required reinforcement ratio). The researchers applied an axial load of 5.7% of the axial capacity of the column. The test results showed the elastic cracked-section stiffness average was 0.23 EI_{gross} for the two columns (Priestley and Benzoni 1996). This value is less than half of the commonly used value of 0.5 EI_{gross} value. If this reduction is due to the low longitudinal reinforcement ratio it may be a key design factor for designing a column with HSS, which could have lower reinforcement ratios when compared to a column containing conventional Grade 60 reinforcing. Test results indicated that the column with a longitudinal steel ratio of 0.5% exhibited a ductile response, adequate distribution of flexural cracking, and failed at a displacement ductility of $\mu_\Delta = 10$ due to shear failure. The maximum drift angle was reported to be 2.6% (Priestley and Benzoni 1996). Test results for the column with a longitudinal steel ratio of 1.0% indicated that failure was due to shear (Priestley and Benzoni 1996). The researchers did not report on the anticipated reduction in the capacity due to the low longitudinal reinforcement ratio. However, the authors did recommend that the strength of the concrete component should be considered independently from the reinforcement ratio. The authors concluded that results confirmed analytical predictions that 0.5% can safely be used as the lower longitudinal reinforcement ratio for circular bridge columns containing Grade 80 steel reinforcement. This conclusion may prove critical to the full implementation of the use of Grade 80 reinforcement because current codes limit the ratio to 1.0%.

Ziehl et al. (2004) conducted a study investigating the minimum longitudinal reinforcement requirements for concrete columns. However, this study evaluated 24 small-scale specimens and focused on the effects of the low longitudinal reinforcement ratio on the long-term performance of axially loaded columns. The columns tested had longitudinal reinforcement ratios ranging from zero to 0.72 percent. The researchers concluded that none of the reinforcement ratios prevented passive yielding of the longitudinal reinforcement for the concrete strengths and axial loads used in the study. This conclusion assumed compatibility of deformations for concrete and the longitudinal reinforcement and the authors used a rather liberal estimate of sustained service-level axial load ($0.4f'_cA_g$). The authors reported that under a smaller sustained loads with a low probability of exceedance (i.e., bridge columns), smaller, long-term deformations would be expected and it may be possible to safely use a lower longitudinal reinforcement ratio. This conclusion combined with the conclusions from Priestley and Benzoni (1996) indicate that the use of Grade 80 reinforcement in columns may hold promise.

2.4.2 Columns with HSS Longitudinal Reinforcement

The use of high-strength reinforcement (HSS) in concrete columns was evaluated by Rautenberg et al. (2010). The researchers reported that HSS reinforcing bars reduced bar congestion without significantly reducing the performance for RC columns with low axial loads. Test results indicated that columns reinforced with conventional A615 Grade 60 and HSS (ASTM A1035 Grade 120) exhibited drift ratios exceeding 4% and both had similar moment capacities (Rautenberg et al. 2010). Their results indicated that as long as the fracture strain of the longitudinal reinforcement exceeded 7% for a reference gage length (8 inches [0.203 m]) and the amount and detailing of the transverse reinforcement is adequate to prevent shear failure, bond failure, and bar buckling, then the amount of reinforcement can be reduced proportionally with the increased yield strength. The authors reported a noticeable difference in hysteretic energy dissipation between columns and noted that the difference was a result of the difference in stiffness. The column constructed with the high strength steel had about half the amount of longitudinal steel as the columns constructed with the conventional strength steel. This resulted in the columns reinforced with HSS having about half the stiffness compared to the columns containing conventional steel. The decrease in stiffness results in a smaller area contained in the hysteretic loop and therefore, the energy dissipated is smaller.

A reduction in energy dissipation will likely be observed with columns constructed with Grade 80 reinforcing steel because the amount of steel will be about a third less than a column reinforced with conventional ASTM A706 Grade 60. However the reduction in energy dissipation may be lower when using ASTM A706 Grade 80 reinforcement compared to ASTM A1035 Grade 120 reinforcement because of the difference in stress-strain performance. ASTM A706 Grade 80 exhibits more ductile behavior when compared with ASTM A1035 Grade 120 reinforcement. Columns constructed with Grade 80 will likely have a decrease in energy dissipation, however the extent of the reduction is unknown and further testing is needed.

2.4.3 Columns with HSS Transverse Reinforcement

Saatcioglu and Baingo (1999) reported on the effect of HSS transverse reinforcement on the performance of circular high-strength concrete columns subjected to simulated seismic loadings. The columns contained concrete ranging in strength from 8.7 ksi (60 MPa) to 18.9 ksi

(130 MPa). The transverse steel yield strength ranged from 60 ksi (420 MPa) to 145 ksi (1 GPa) and both hoops and spirals were used for the transverse reinforcement. The results from nine column tests indicated that the columns with higher strength transverse steel developed significantly higher deformability compared to the columns with reinforced with a conventional Grade 60 transverse steel. Test results showed a good relationship between the volumetric ratio and transverse yield strength, and thus the authors suggested the product of these two parameters could be an important factor in design using HSS reinforcement. With respect to the use of hoops versus spirals the hoops were observed to straighten in the plastic hinge region during testing while the spirals did not. The authors reported that instability of the longitudinal bars occurred due to the relaxation of the restraining action of the hoops. In general the authors concluded that spirals were more effective in controlling stability on the inelastic behavior of the longitudinal reinforcement. This observation supports Oregon DOT's requirement for spiral type reinforcement in columns designed for seismic loading.

Paultre et al. (2001) investigated the influence of concrete strength and transverse reinforcement yield strength on behavior of high strength concrete (HSC) columns. Concrete strengths investigated range from 11.6 ksi (80 MPa) to 17.4ksi (120 MPa) and the transverse steel yield stress ranged from 58 ksi (400 MPa) to 116 ksi (800 MPa). The results from eight columns indicated that the ductility of HSC columns is dependent on the concrete strength. The results showed good agreement with the results by Saatcioglu and Baingo (1999) in that the transverse steel can be decreased when the yield strength of the transverse steel is increased. The authors reported that the required amount of transverse reinforcement should be a function of volumetric ratio and the yield strength of the transverse reinforcement. It is important to note that the authors also concluded that high yield strength is not totally effective when columns are poorly confined. This indicates that the spacing of transverse reinforcement cannot simply be doubled if the yield strength of the transverse reinforcement is doubled.

2.5 Summary

Although Grade 80 reinforcing steel has the potential to make RC members more efficient, further research is needed. Early results indicate that Grade 80 reinforcement can reduce the required amount of longitudinal steel reinforcement and transverse reinforcement. However, these reductions are likely not a ratio of the increase in yield strengths. Further research is needed on characterizing Grade 80 reinforcement and on assessing the performance of columns (and other members) containing Grade 80 reinforcement.

Chapter 3

EXPERIMENTAL PROGRAM AND SPECIMEN DESIGN

An experimental program was developed to assess the performance of RC columns containing Grade 80 reinforcement meeting ASTM A706 requirements subjected to cyclic loadings. This experimental program consisted of testing six half-scale circular reinforced concrete bridge columns. Three of the experimental columns were reinforced with ASTM A706 Grade 80 reinforcement and the remaining three columns were reinforced with ASTM A706 Grade 60 reinforcement. Note that although this report provides information on the six columns, it only provides results for columns C1 and C2. Results from columns C3 – C6 will be provided in a report to ODOT and ODOT provided match funding to do the additional tests. In addition to the reinforcement grade, two additional variables were investigated:

1) Longitudinal reinforcement ratio;
2) Column shear span ratio.

The experimental plan is shown in Table 3-1.

Note that all six columns have the same spiral pitch of 2.50 inches (0.064 m). Spiral reinforcement is #3 (#10M) bar. This corresponded to a transverse reinforcement ratio of 0.82 percent. The longitudinal and transverse reinforcement ratios, p_l and p_t provided in Table 3-1 are computed using the following equations:

$$p_l = \frac{A_{sl}}{A_g - A_{sl}} \tag{3.1}$$

$$p_t = \frac{4A_{st}}{sD_{cc}} \tag{3.2}$$

where A_{sl} is the total cross-sectional area of the longitudinal reinforcing bars and A_g is the gross cross-sectional area of the column. A_{st} is the cross-sectional area of a single transverse reinforcing bar, s is the spiral pitch, and D_{cc} is the diameter of the column core, measured out-to-out of the spiral.

Table 3-1 Experimental test matrix

Tests	**Shear span ratio** M / VD	**Design Concrete Strength,** f'_c	**Longitudinal Reinforcement**	**Transverse Reinforcement**
C1	6	4 ksi (30 MPa)	ASTM A706 Grade 60 ksi (420 MPa) 16 #5 (#16M) ρ_l = 1.11%	ASTM A706 Grade 60 ksi (420 MPa)
C2	6	4 ksi (30 MPa)	ASTM A706 Grade 80 ksi (550 MPa) 12 #5 (#16M) ρ_l = 0.83%*	ASTM A706 Grade 80 ksi (550 MPa)
C3	6	4 ksi (30 MPa)	ASTM A706 Grade 60 ksi (420 MPa) 22 #6 (#19M) ρ_l = 2.19 %	ASTM A706 Grade 60 ksi (420 MPa)
C4	6	4 ksi (30 MPa)	ASTM A706 Grade 80 ksi (550 MPa) 16 #6 (#19M) ρ_l = 1.58%	ASTM A706 Grade 80 ksi (550 MPa)
C5	3	4 ksi (30 MPa)	ASTM A706 Grade 60 ksi (420 MPa) 22 #6 (#19M) ρ_l = 2.19 %	ASTM A706 Grade 60 ksi (420 MPa)
C6	3	4 ksi (30 MPa)	ASTM A706 Grade 80 ksi (550 MPa) 16 #6 (#19M) ρ_l = 1.58%	ASTM A706 Grade 80 ksi (550 MPa)

*The longitudinal reinforcement ratio for column C2 is lower than the 1% minimum reinforcement ratio defined in Sec. 5.10.11.4.1.a for seismic zones 3 and 4 (AASHTO 2012). This value was chosen to determine through testing if a value lower than 1% may be used. The value chosen does, however, meet the general minimum reinforcement ratio for compression members defined in Sec. 5.7.4.2, which does take into account the strengths of reinforcement and concrete materials (AASHTO 2012).

Figure 3.1 shows the test elevations for the six test columns. Figure 3.1(a) represents columns C1, C2, C3, and C4 and Figure 3.1(b) represents columns C5 and C6. The centroid of the axial load is applied through the center of the header (and column).

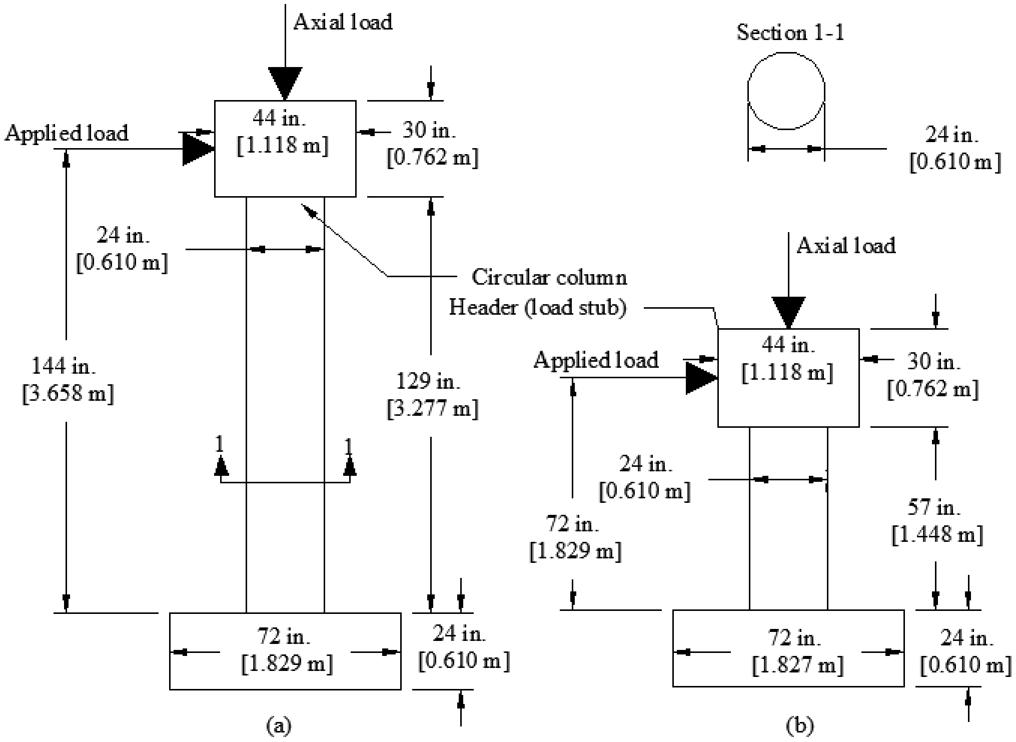

Figure 3.1 Test elevations for: (a) columns C1 through C4 and (b) columns C5 and C6

3.1 Design of Test Columns

The columns were tested as cantilever columns and corresponds to an aspect ratio of M/VD = 6 for columns C1, C2, C3 and C4 and M/VD=3 for columns C5 and C6 (M is the moment capacity, V is the shear capacity, and D is the column diameter). The test columns are representative of a bridge containing a single pier and the two different shear heights tested correspond to the behavior in the transverse and longitudinal directions of the bridge. Column C1 was designed with a reinforcement ratio just above the minimum requirement ratio of 1% defined by AASHTO Sec. 5.10.11.4.1.a. Column C2 was designed to provide approximately the same capacity as column C1 but using Grade 80 reinforcement. Columns C3 and C4 were designed to have a higher reinforcement ratios and columns C5 and C6 have the same reinforcement ratio as columns C3 and C4 but with half the shear span ratio. For the design verification, the following assumptions were made:

1) Axial Load: $P = 0.05 f_c' A_g$
2) where f'c represents the nominal concrete strength and Ag is the gross cross-sectional area of the column.
3) An over strength resistance factor of $\lambda = 1.4$ was applied to the nominal moment capacity.

The applied axial load is 90 kips (400 kN), 5 percent on the columns nominal axial capacity. Expected material strengths were not used in the design; instead an over-strength resistance factor was applied to the calculated nominal moment capacity of the columns. Designs included nominal material strengths for steel and concrete. Actual material strengths were determined with laboratory testing and these are described in Chapter 4.

The methodology for the design verification for each of the test specimens is presented in this chapter. Detailed computations are provided in Trejo et al. (2014).

The procedures and assumptions used in the design of the test columns, footings, and header are presented here. The longitudinal reinforcement ratios were pre-defined as shown in Table 3-1. Checks performed correspond to the verification of the peak expected shear force and peak expected bending moments, which are then used to back-calculate design forces which are then used in the verifications of the designs.

3.1.1Bending Moment Capacity

The column cross-section design procedures follow:

1) Assume an applied axial load: P = (5%)(Ag)(f'c)

2) Determine column cross section properties based on experimental plan and half-scale 1.25 inch (0.032 m) clear cover. Note that full-scale clear cover was assumed to be 2.5 inch (0.064 m), which is the minimum cover for a spiral as defined by BDDM Sec. 1.1.13.12 (ODOT 2012). Figure 3.2 shows the column cross-sections, note that columns C3 and C5 have identical cross-sections and columns C4 and C6 also have identical cross-sections.

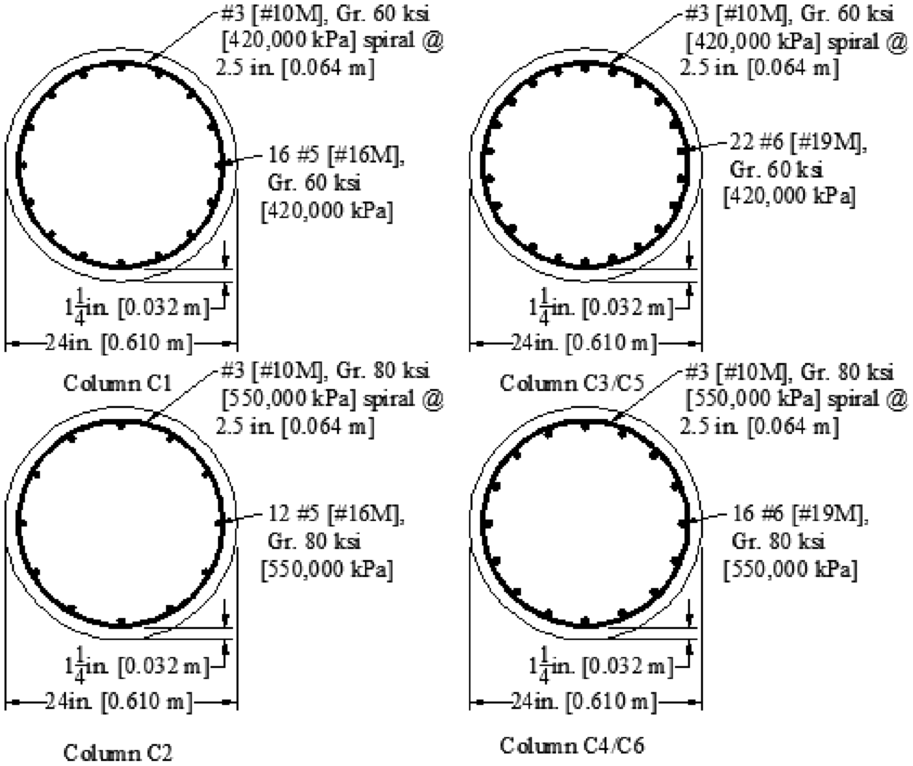

Figure 3.2 Tested column cross-sections

3) Determine the nominal moment capacity based on nominal material strengths. Response 2000 structural analysis software was used to determine these values. The material stress strain models used are summarized in Table 3-2. Trejo et al. (2014) provides details on Response 2000 inputs and sectional response output.

Table 3-2 Response 2000 material stress strain properties

	Steel	Concrete		
		Base Curve	Comp. Softening	Tension Stiffening
Model	Elastic-perfectly Plastic	Popovics/Thorenfeldt/Collins (Collins and Mitchell 1991)	Vecchino-Collins 1986 (Vecchio and Collins 1986)	Bentz 1999 (Bentz 2000)

4) Check solutions from step (3). DT Column (Texler 2001) and OpenSees (The Regents of the University of California 1999) were used to check this design.
5) Compute the expected bending moment capacity as the product of the nominal moment capacity and a bending moment over-strength factor to account for the increase in actual material strength. Results for all columns are shown in Table 3-3. Note that columns C3 and C5 have the same nominal moment capacity. Columns C4 and C6 also have the same nominal moment capacity. The slight difference in moment capacities between columns C3/C5 and columns C4/C6 results from columns C3 and C5 using 22 reinforcing bars while only 16 reinforcing bars are used in columns C4 and C6. The reduction in longitudinal reinforcement cross-sectional area from 22 to 16 reinforcing bars is greater than the increase in yield strength of the bars from 60 ksi (420 MPa) to 80 ksi (550 MPa), thus leading to the small differences.

Table 3-3 Column nominal and expected moment capacities

Column	Nominal moment capacity from Response 2000 ft-kip (m-kN)	Expected moment capacity ft-kip (m-kN)	Expected shear capacity ft-kip (m-kN)
C1	287.8 (212,300)	402.9 (297,200)	33.6 (45.5)
C2	284.7 (210,000)	398.6 (294,000)	33.2 (45.0)
C3	463.2 (341,600)	648.5 (478,300)	54.0 (73.3)
C4	448.2 (330,600)	627.5 (462,800)	52.3 (70.9)
C5	463.2 (341,600)	648.5 (478,300)	108.1 (146.5)
C6	448.2 (330,600)	627.5 (462,800)	104.6 (141.8)

6) Using the expected bending moment capacity from step (5), determine the internal compression and tension resultant forces of the cross section.
7) Check answer from step (6) by summing the internal forces and setting them equal to the applied axial load determined in step (1).

3.1.2 Transverse Reinforcement Design

Spiral reinforcement was used in the construction of all columns. Spirals were chosen over circular hoops because spirals are required by ODOT BDDM, and these are typically more economical than hoop reinforcement (ODOT 2012).

All spirals were fabricated with ASTM A706 reinforcing bars following common practice and following prescriptions in the Caltrans SDC (2012). The grade of the transverse reinforcement will be the same grade used for the longitudinal reinforcement for each column (i.e., either Grade 60 or Grade 80).

Following the guidelines from AASHTO (2012) Sec. 5.10.6.2, each end of the spiral will be anchored with at least an additional 1.5 extra turns. Actual construction of spirals included 2.0 extra turns. To determine the required pitch of the transverse spiral, the column can be divided into two regions: the plastic hinge region and the non-plastic hinge region. In the plastic hinge region, the pitch was designed to ensure it met the demands for confinement. The required pitch for the plastic hinge region is less than the non-plastic hinge region. To simplify the construction of the columns, a uniform pitch was used for the entire height of the column. This met the requirements of a constant spaced continuous spiral in Sec. 5.10.6.2 ODOT's BDDM (2012) and AASHTO's LRFD (2012). The length of the plastic hinge region, l_p, was calculated as the greater value of the maximum column dimension, column height divided by 6, or 18 inches (0.46 m) following ODOT's BDDM section 1.1.10.2-2 (2012). The plastic hinge length is considered to be 24 inches (610 mm) long measured from the face of the footing. Note this height is larger than the required analytical plastic hinge length computed following Caltrans SDC of 19.35 inches (0.4915 m).

Columns C2, C4, and C6 are transversely reinforced with HSS. A yield strength of 80 ksi (550 MPa) was used for the spiral reinforcement in the design. This value exceeds the maximum spiral yield strength value allowed in Sec. 1.1.9.5 of ODOT's BDDM (2012). The transverse reinforcement has the same pitch and termination details for all six columns. Detailed step-by-step calculations for the transverse reinforcement were performed using MATHCAD®. MATHCAD® calculations for the six columns are provided in Trejo et al. (2014). The procedure for the spiral design is as follows:

(1) Adjust input values according to column properties and loading conditions;
(2) Determine the shear force demand according to Sec. 5.8.2.9 AASHTO LRFD BDS (2012);
(3) Determine the maximum and minimum spiral pitch according to the current AASHTO code requirements;
    (A) Sec. 5.10.6.2 AASHTO LFRD BDS (2012)
    (B) Sec. 5.8.2.7 AASHTO LFRD BDS (2012)
    (C) Sec. 5.7.4.6 AASHTO LFRD BDS (2012)
    (D) Sec. 5.10.11.4.1d AASHTO LFRD BDS (2012)
    (E) Sec. 5.8.2.5 AASHTO LFRD BDS (2012)
    (F) Sec. 5.10.11.4.3 AASHTO LFRD BDS (2012)
    (G) Sec. 8.6.5 AASHTO LFRD SBD (2012)
    (H) Sec. 8.8.9 AASHTO LFRD SBD (2012)
    (I) Determine the controlling maximum and minimum spiral pitch
(4) Calculate the concrete contribution to shear capacity, V_c, according to Sec. 8.6.2 in the AASHTO LFRD SBD (2012);
(5) Calculate the maximum allowed reinforcing steel contribution to shear capacity, V_s, according to Sec. 8.6.4 in the AASHTO LFRD SBD (2012);
(6) Calculate V_s according to Sec. 8.6.1 in the AASHTO LFRD SBD (2012) and check against the maximum shear reinforcement calculated in step 5;

(7) Calculate the required pitch according to Sec. 8.6.3 in the AASHTO LFRD SBD (2012);

(8) Determine the final pitch to be used over the entire height of the column and the corresponding transverse reinforcement ratio,

3.1.3 Reinforced Concrete Header Design

The column header is designed to allow for the transfer of lateral forces from the actuator to the test specimen. The header also is used to transfer axial forces to the columns. The header was designed using the strut-and-tie method. The reinforcement details are the same for all test columns except for the spiral reinforcement within the header. Columns C1 and C2 have hoops instead of spirals, the spacing for both types of transverse reinforcement was kept constant. The reinforced concrete header has plan view dimensions of 44 inches (1.118 m) by 44 inches (1.118 m) and is 30 inches (0.762 m) deep, as shown in Figure 3.3 and Figure 3.4.

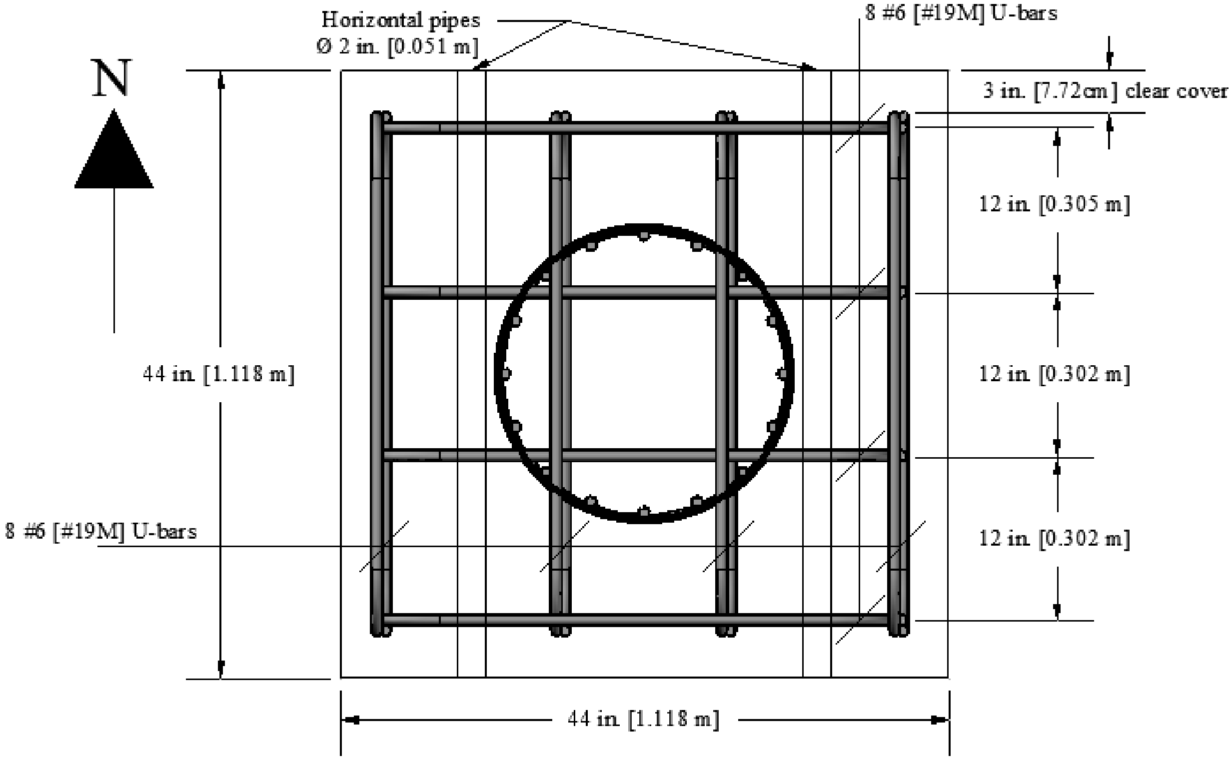

Figure 3.3 Plan view of header reinforcement

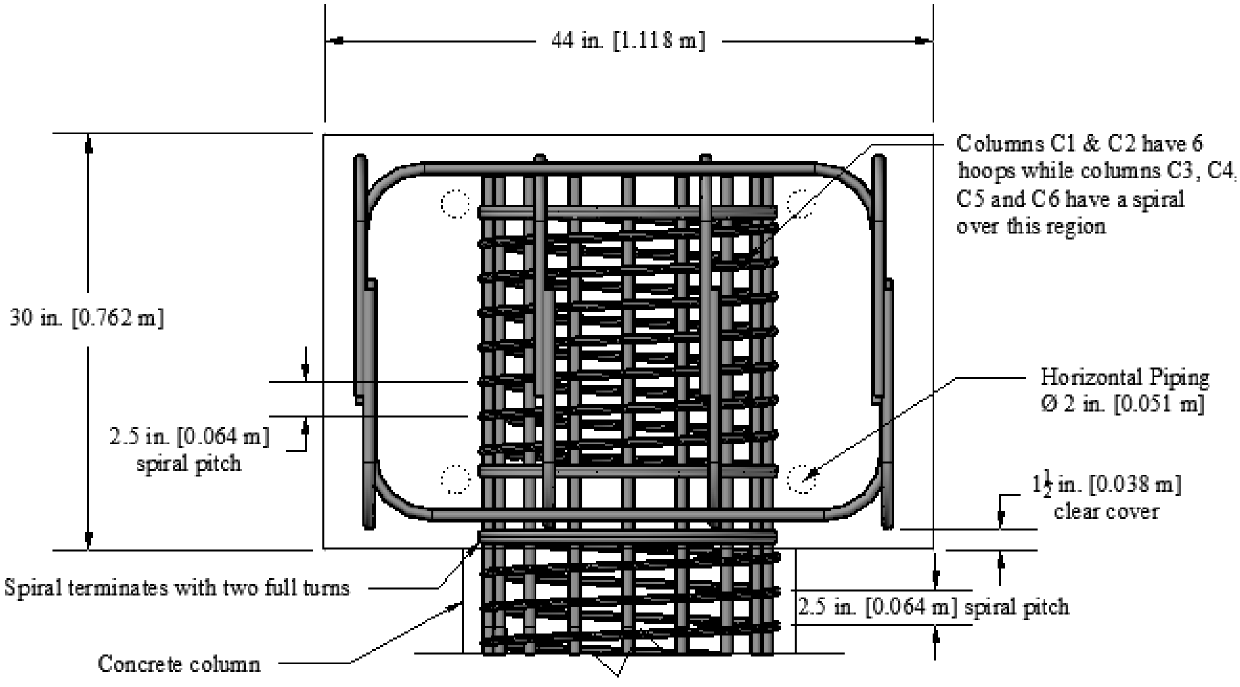

Figure 3.4 North-south Elevation view of header reinforcement

The spacing of reinforcement mats in the header is the same in both directions. A clear cover of 3 inches (0.076 m) is used to accommodate recesses used to attach the actuator to the header. Figure 3.4 shows an elevation view of the header reinforcement details for columns C1 and C2. Columns C3, C4, C5, and C6 have the same headers as shown in Figure 3.4 except a spiral was used for columns C3, C4, C5 and C6 instead of the 6 hoops used for columns C1 and C2. This was done for ease of fabrication. Detailed step-by-step calculations for the header were performed in MATHCAD® and these can be found in Trejo et al. (2014).

3.1.4 Footing Design

The test column footing was designed using a strut-and-tie method following ODOT's BDDM (2012) and AASHTO's LFRD (2012). The footing reinforcement consists of top and bottom reinforcement mats with additional horizontal and vertical bars. The additional reinforcing bars were added because the strut-and-tie model indicated that these were needed to transfer the footing tie down and axial load forces. All footing reinforcement is of #6 (#19M) ASTM A706 Grade 60 reinforcing bars. The longitudinal bars in the column extend down into the footing and terminate with 90 degree hooks at the bottom reinforcement mat. The legs of the hooks are 12 inches (0.305 m), as specified in Sec. 1.1.13.1.10 ODOT's BDDM (2012). Detailed step-by-step calculations preformed using MATHCAD® can be found in Trejo et al. (2014). Figure 3.5 and Figure 3.6 show the plan view and elevation view of the footing respectively.

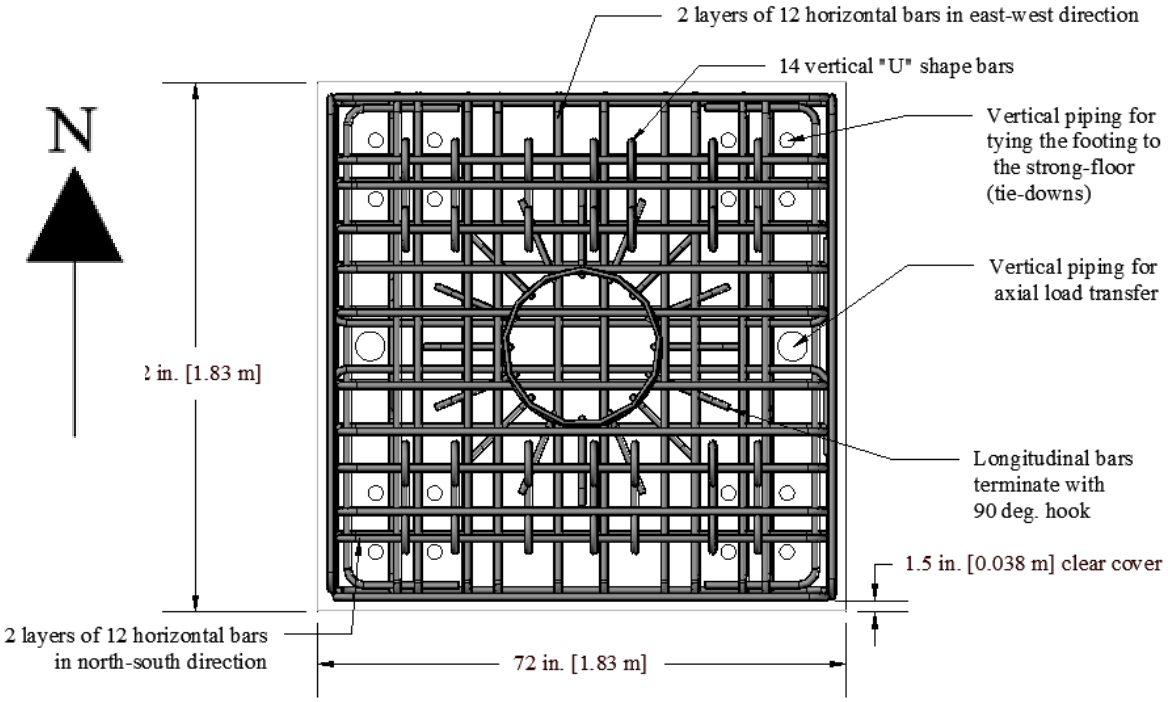

Figure 3.5 Plan view of footing reinforcement

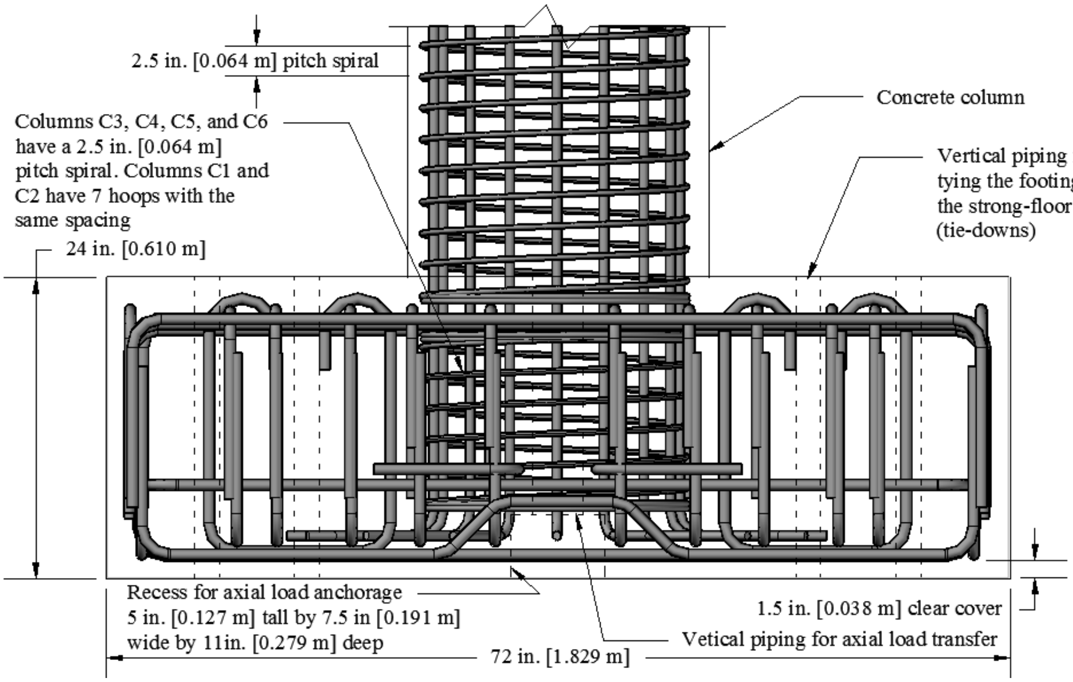

Figure 3.6 North-south elevation view of footing reinforcement

3.2 Instrumentation of Test Specimens

Each test specimen was instrumented to determine the performance of each column. A summary of instrumentation used for each column test is shown in Table 3-4.

Table 3-4 Summary of measure observations and instrumentation

Measured observation	Instrumentation	Drawing Label*
Column lateral deflection	6 string pots	(A)
Column curvature	20 string pots	(B)
Shear deformations	8 string pots	(C)
Longitudinal reinforcing steel strain	22 strain gages	(D)
Transverse reinforcing steel strain	7 strain gages	(E)
Column tilt	1 tilt sensor	(F)
Applied lateral load	1 load cell	(G)
Applied vertical load	1 load cell 2 pressure gages	(H) (I)
Footing movement	4 LVDTs (vertical) 2 LVDTs (horizontal) 2 string pots (horizontal)	(J) (K) (L)
Strong wall movement	2 string pots	(M)

*See Figure 3.7 through

Figure 3.11.

Locations for all instrumentation listed in Table 3-4 are shown in Figure 3.7 through Figure 3.11. All tests used a data sampling rate of five samples per second or greater. Two 3/8 inch (0.00953 m) diameter rods were cast into the column at each instrumentation levels (5 layers of 2 rods, 10 total). The rods were spaced at either 4 inches (0.102 m) or 5 inches (0.127 m) and were horizontally centered in the column. The 4 inch (0.102 m) spacing was the default spacing and the 5 inch (0.127 m) spacing was used when the longitudinal reinforcement prevented the default spacing from being used. Aluminum angles were attached to the thread rods and the string pots were attached to the aluminum angles.

Strain gages were placed on both longitudinal and transverse reinforcement. Strain gages on the longitudinal reinforcement were place on the farthest northern and southern bars -i.e., in the direction of the applied horizontal load. Two strain gages were placed in the plastic hinge zone on both the east and west sides of the bar. Duplicate gages were installed for redundancy. Single gages were placed outside of the plastic hinge zone on the east side of the bar. Transverse strain gages were placed on the outer most surface of the spiral reinforcement at approximately the same elevations as the strain gages on the longitudinal bars.

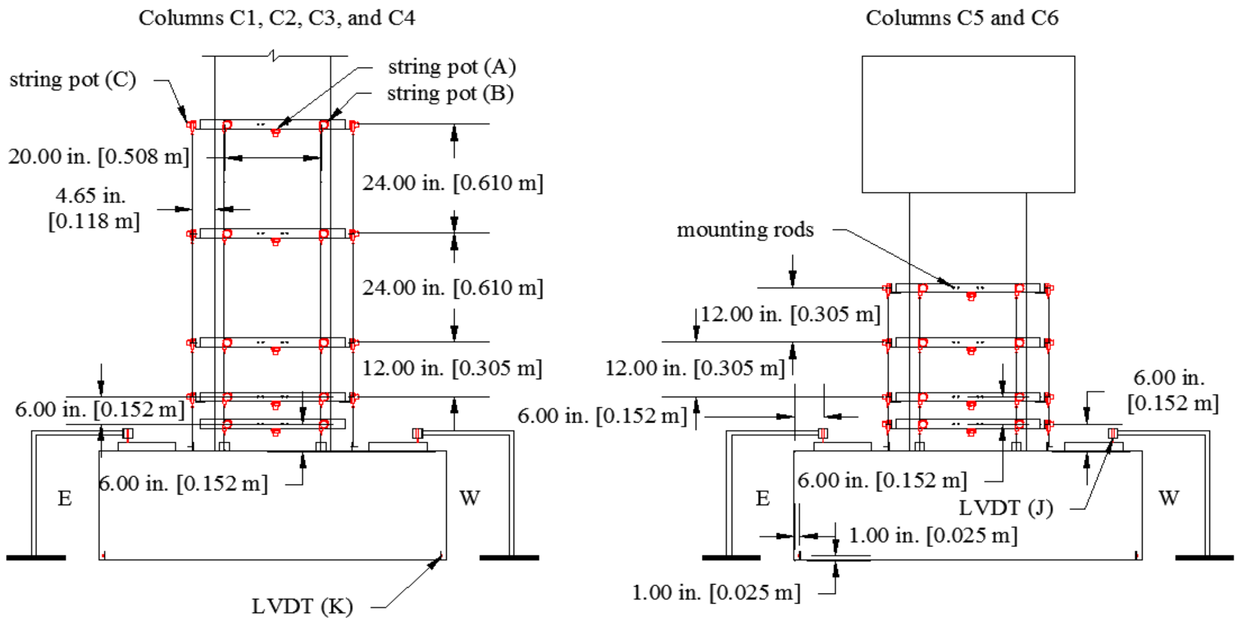

(a)

(b)

Figure 3.7 North elevation view of external instrumentation for (a) columns C1 through C4 and (b) columns C5 and C6

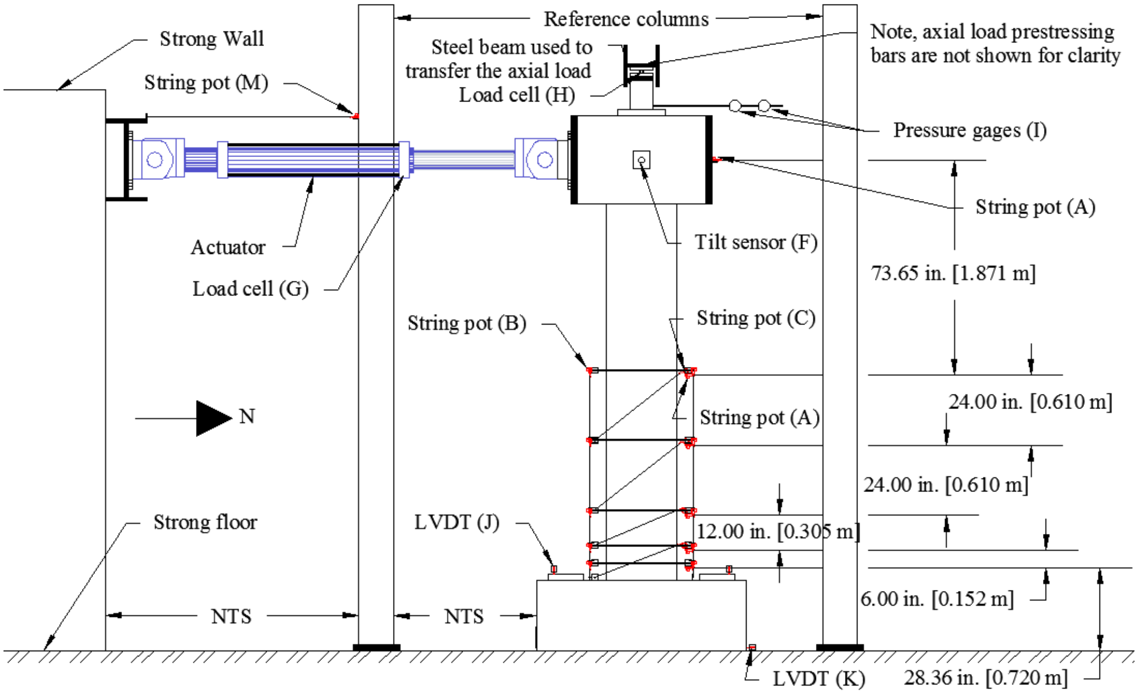

Figure 3.8 Elevation view of column C1, C2, C3 and C4 external instrumentation (NTS = not to scale)

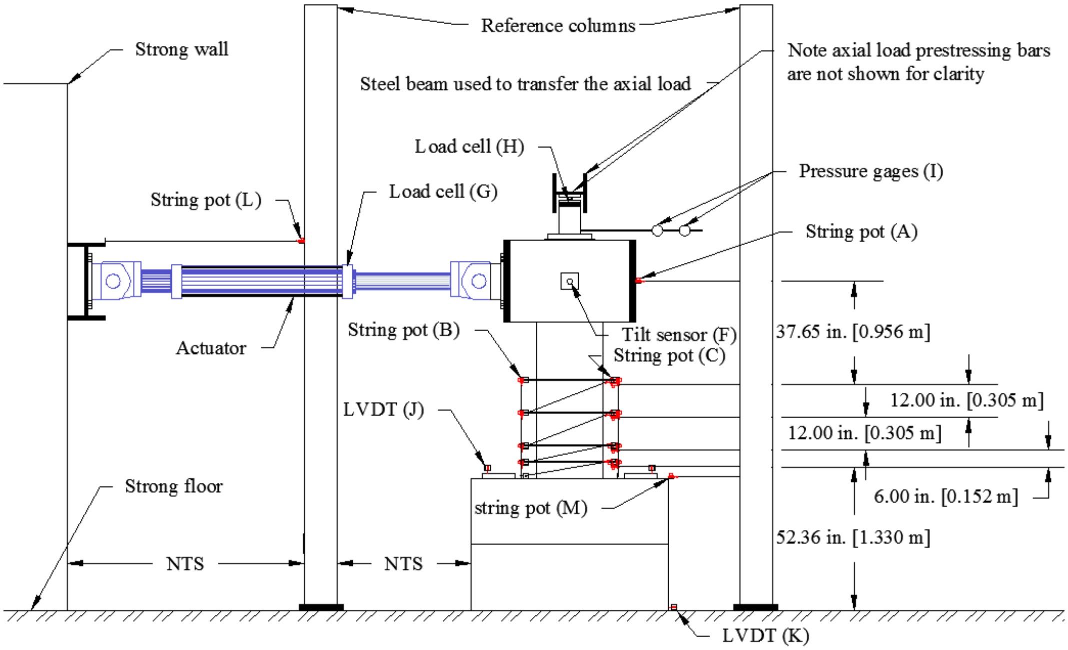

Figure 3.9 Elevation view of column C5 and C6 external instrumentation
(NTS = not to scale)

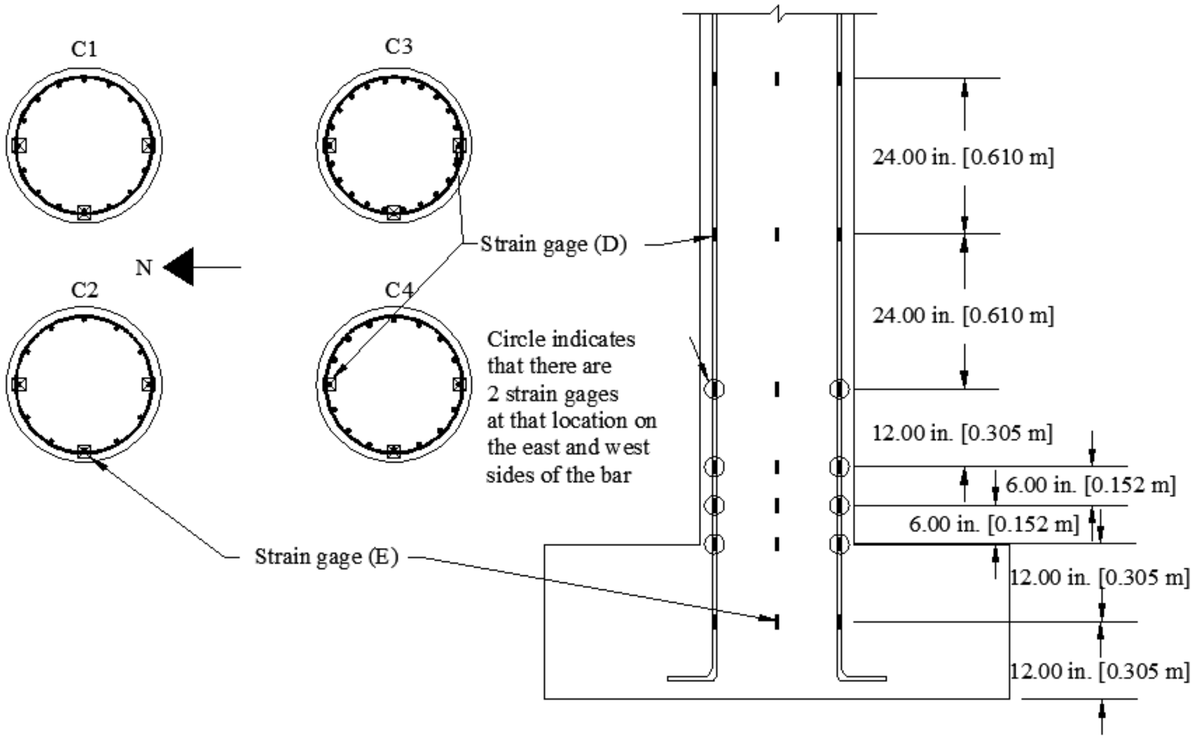

Figure 3.10 Column C1, C2, C3, and C4 internal instrumentation

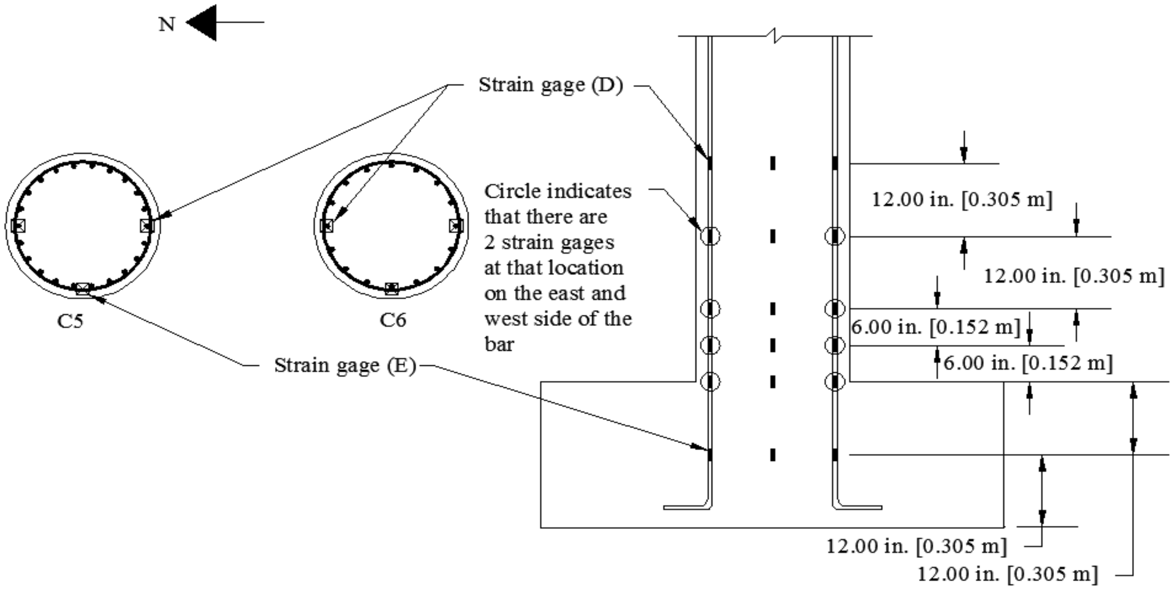

Figure 3.11 Column C5 and C6 internal instrumentation

3.3 Test Setup and Testing Procedure

Test set up initiated with stressing the column footing to the strong floor. The specified stress is defined by the footing capacity; the footing design can be found in Trejo et al. (2014). The hydraulic actuator was then bolted to the RC header. Lastly, the axial load system was assembled. Note that the researchers had concerns with changes in axial load when the specimen was laterally loaded. As a result, the test set-up included systems to minimize changes in axial loads. Figure 3.14 shows a photo of the concave plate and convex nut used to allow rotation and minimize changes in axial load. Additional details of the axial load system can be seen in Figure 3.15, Figure 3.16, Figure 3.17, and Figure 3.18.

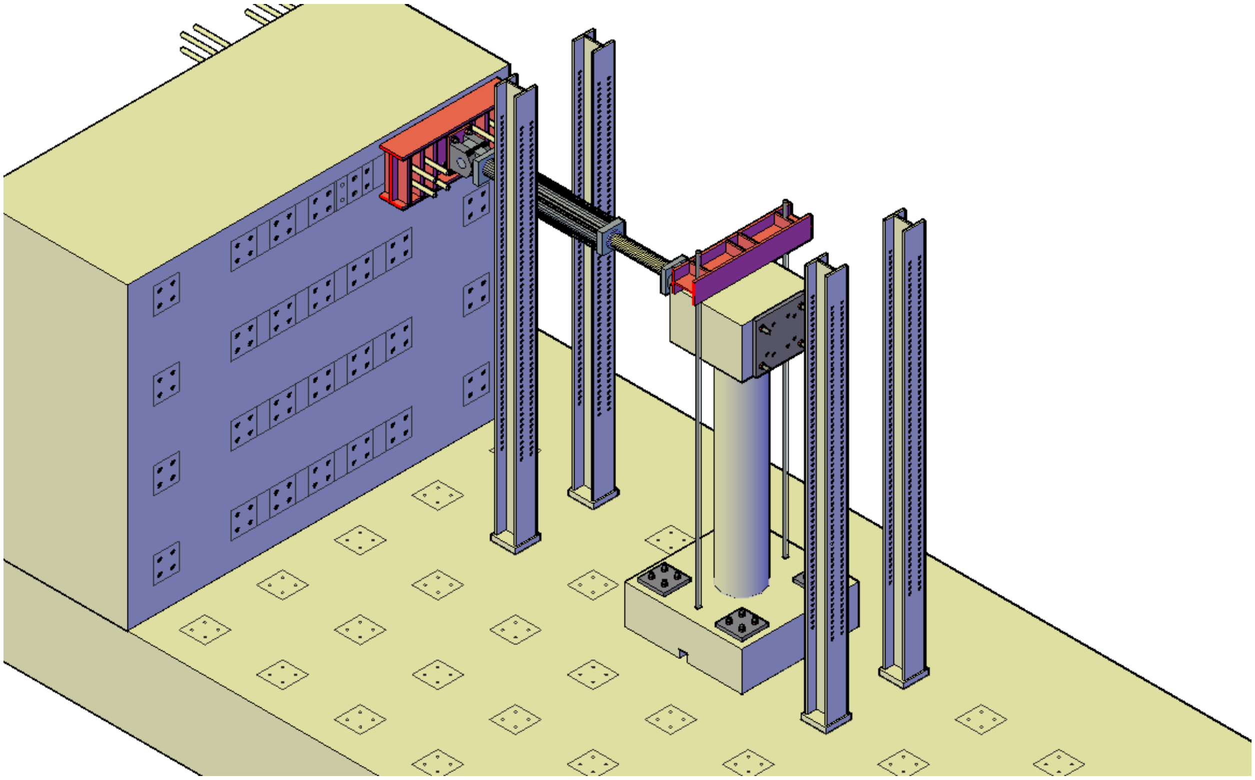

Figure 3.12 3D rendering of test setup for columns C1, C2, C3 and C4

Figure 3.13 Photograph of column during testing

Figure 3.14 Photograph of the concave plate and convex nut

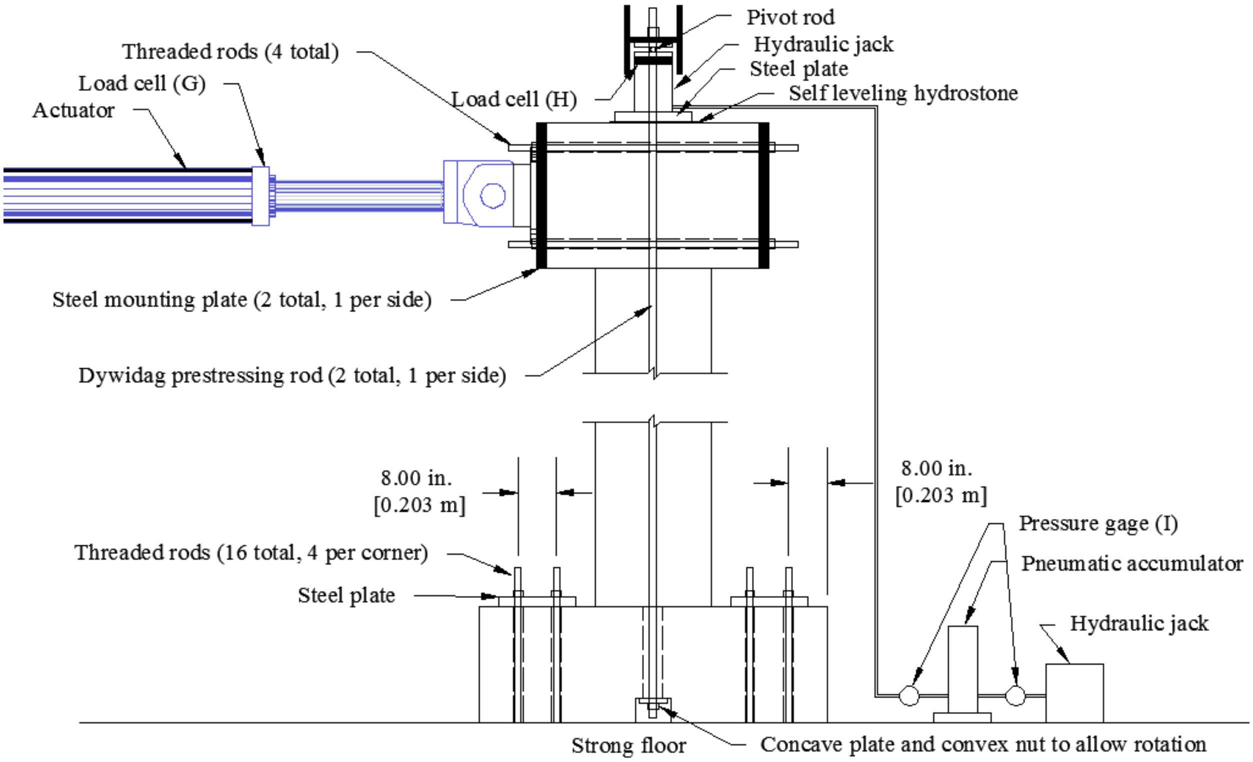

Figure 3.15 Column C1, C2, C3 and C4 east elevation view of test setup

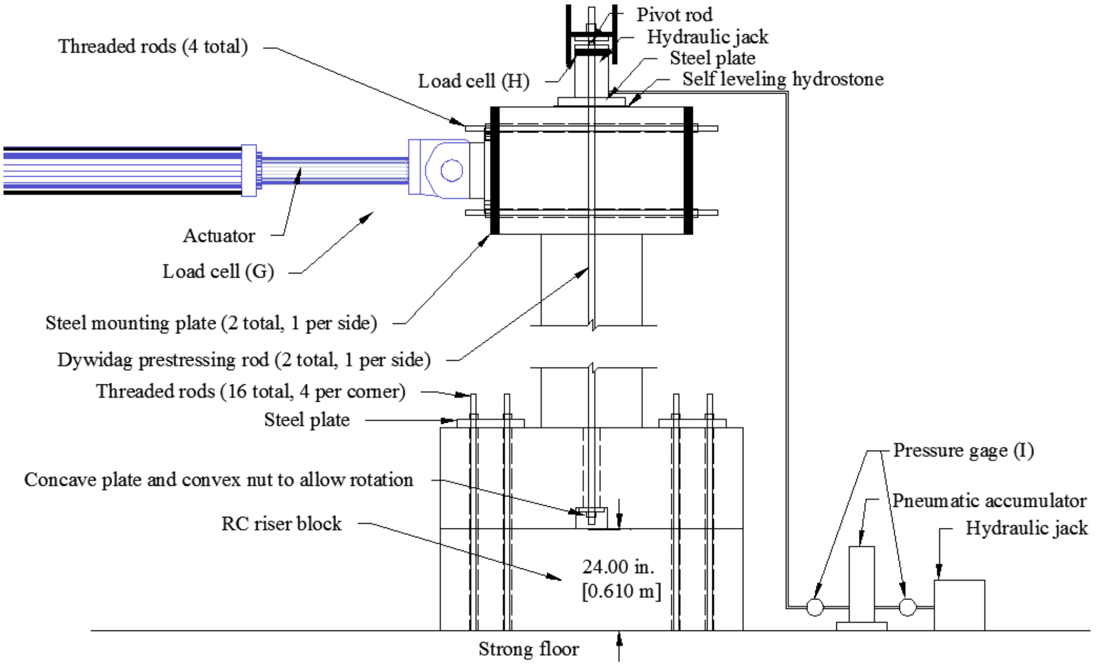

Figure 3.16 Column C5 and C6 east elevation view of test setup

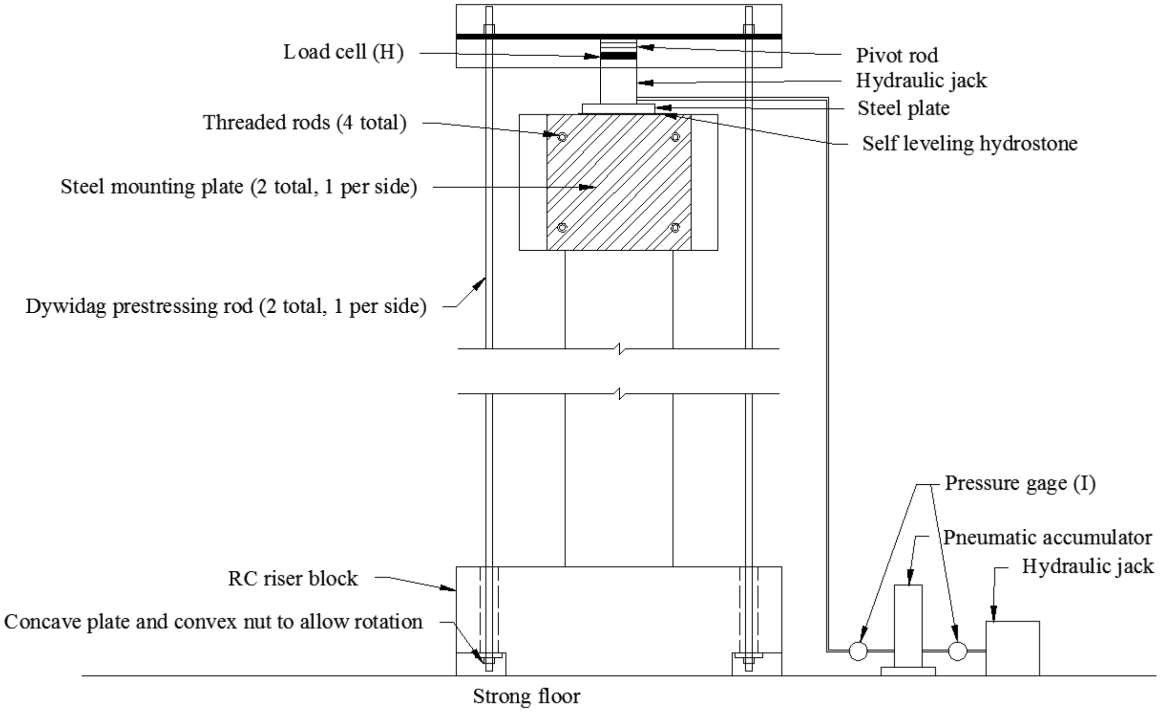

Figure 3.17 Column C1, C2, C3 and C4 south elevation of test setup

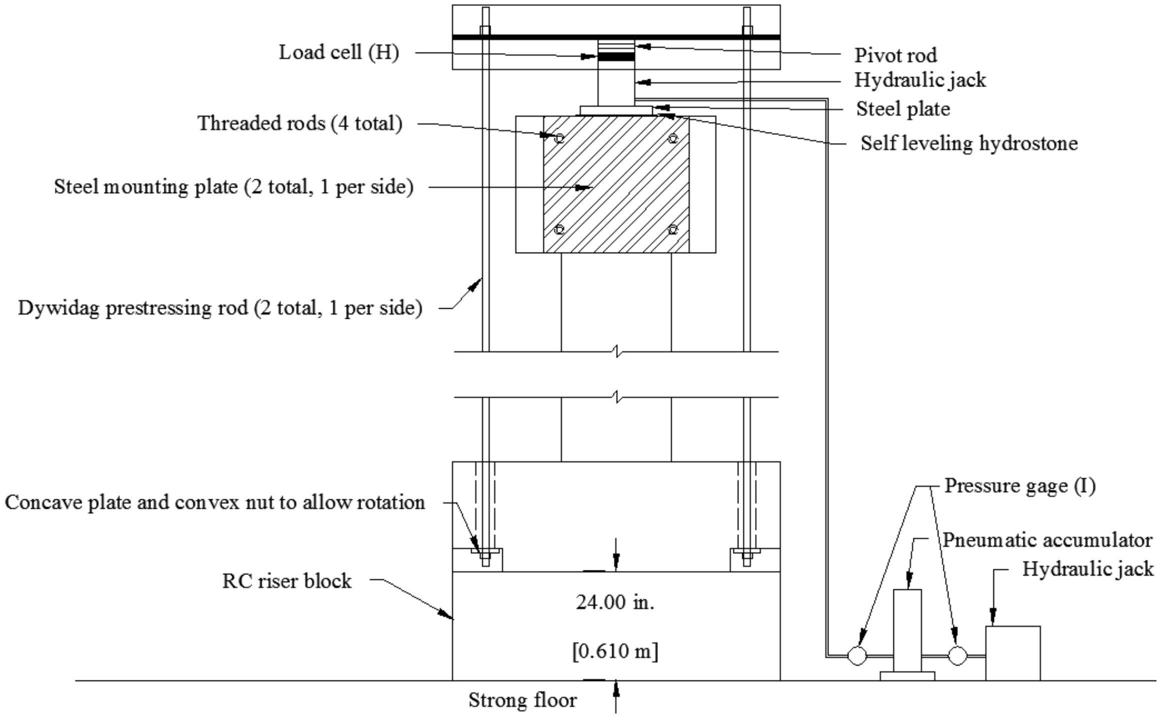

Figure 3.18 Column C5 and C6 south elevation of test setup

Horizontal loading consisted of pushing and pulling the column to predetermined displacement levels. Each displacement level consisted of three cycles: each cycle started at zero displacement, was then loaded in the positive maximum displacement (away from the strong wall), was then loaded in the negative maximum displacement (towards the strong wall), and was finally returned back to zero displacement. Table 3-5 shows the loading profiles for the columns. After all the instrumentation is installed and calibrated, the testing procedure is as follows:

1) Null all instrumentation;
2) Apply axial load;
3) Begin horizontal loading according to the cyclic loading profile listed in Table 3-5. The horizontal loading was paused at the last two peaks of each displacement cycle to visually inspect the column and perform crack mapping.

Table 3-5 Loading Profile for columns C1 through C4

Displacement Cycle, in. (m)	Number of Cycles	Loading Rate, in/s (m/s)
0.10 (0.003)	3	0.01 (0.0003)
0.25 (0.006)	3	0.01 (0.0003)
0.50 (0.013)	3	0.01 (0.0003)
0.75 (0.019)	3	0.01 (0.0003)
1.00 (0.025)	3	0.01 (0.0003)
1.25 (0.032)	3	0.02 (0.0005)
2.50 (0.064)	3	0.04 (0.001)
3.75 (0.095)	3	0.08 (0.002)
5.00 (0.127)	3	0.08 (0.002)
6.25 (0.159)	3	0.08 (0.002)
7.50 (0.191)	3	0.08 (0.002)
8.75 (0.222)	3	0.08 (0.002)
10.00 (0.254)	3	0.16 (0.004)
11.25 (0.286)	3	0.16 (0.004)

3.4 Construction Procedure

Each pair of columns (i.e., columns C1 and C2 in this report) was constructed at the same time. Thus, two sets of formwork were built and the concrete placements for both columns were done on the same day to minimize variability in the concrete. The construction of the test columns can be summarized in the following steps:

1) Application of strain gages on longitudinal column reinforcement

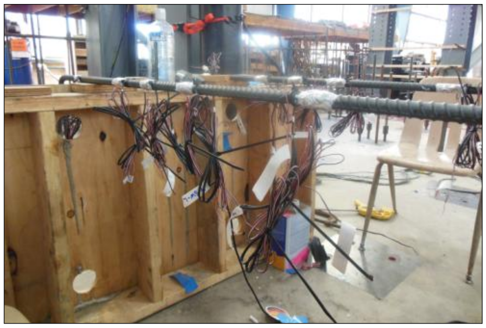

Figure 3.19 Photograph of strain gages on longitudinal column rebar

2) Tying the reinforcing bar cage and applying strain gages to column transverse reinforcement. A cross-section jig was used at both ends of the column reinforcing bar cage to maintain the cross-sectional geometry of the cage section. Note that an additional cross-section jig and temporary support were also placed at the mid span of the cage (not hown in photograph) to keep the cage straight.

Figure 3.20 Photograph of Column C2 rebar cage

3) Tie bottom mat of footing.

Figure 3.21 Photograph of Bottom reinforcing mat of the footing

4) Tie column reinforcing bar cage to bottom reinforcing bar mat of footing and finish tying the remaining footing reinforcement.

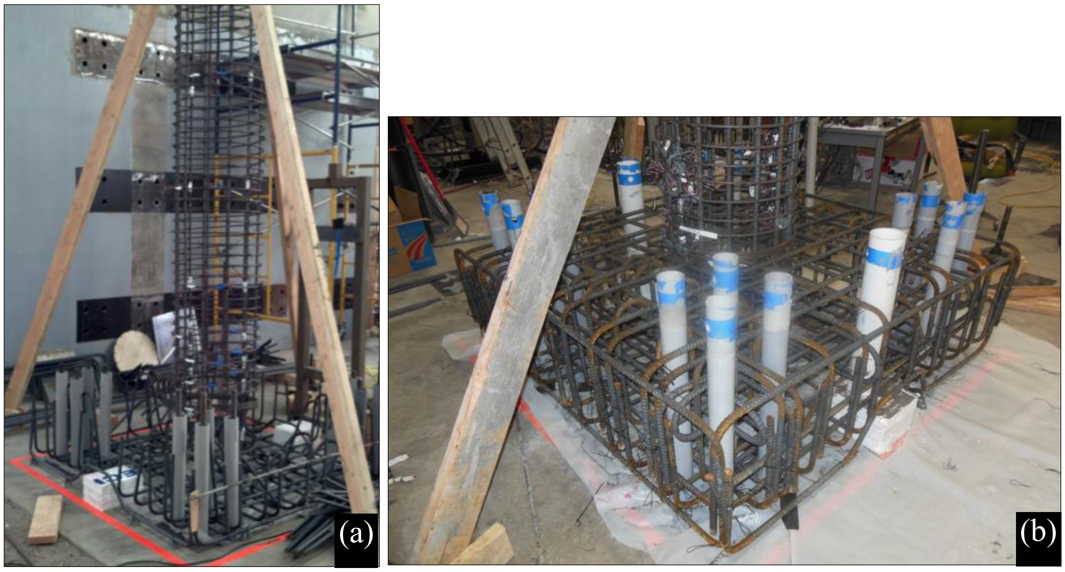

Figure 3.22 Photograph of the placement of reinforcement for: (a) column, and (b) footing

5) Construct footing formwork and place concrete for the footings. Note that two footings were cast at the same time. The concrete was pumped into the footing formwork and consolidated using a concrete vibrator.

Figure 3.23 Photograph of the footing formwork and concrete pour

6) Construct column header shoring and false decking. Sonotube was used for the column formwork. Holes were made on the East and West sides of the Sonotube to pass strain gage cables to the outside of the column.

Figure 3.24 Photograph of the header shoring and false decking

7) Tie header reinforcing bar cage.

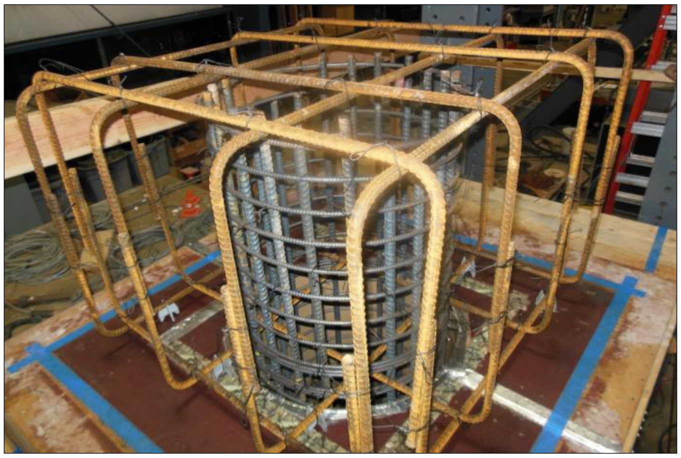

Figure 3.25 Photograph of the header reinforcing bar cage

8) Construct the header formwork and place pipes for actuator tie-rods. Then place the concrete in the columns and headers. Note that two columns (C1 and C2) and headers were cast on the same day and from the same concrete truck. The concrete was pumped

into position using a tremie tube. This prevented aggregate segregation. Concrete was consolidated using a concrete vibrator.

Figure 3.26 Photograph of the header and column formwork and shoring

Two columns, one containing Grade 60 reinforcement and the other containing Grade 80 reinforcement, were fabricated to assess the influence of high strength reinforcing bars on column performance. Figure 3.27 shows a photo of columns C1 and C2 fully constructed with all formwork and shoring removed.

Figure 3.27 Photograph of columns C1 and C2

Chapter 4

MATERIALS USED IN CONSTRUCTION OF TEST SPECIMENS

4.1 Reinforcing Steel

Two grades of reinforcing steel, Grade 60 and Grade 80 were used in the construction of the test specimens. Both steels met the relevant requirements for *ASTM A706/A706M Standard Specification for Low-Alloy Steel Deformed and Plain Bars for Concrete Reinforcement*. Three bar sizes, #3 (#10M), #5 (#16M) and #6 (#19M) were used in the construction of the test specimens. The #3 (#10M) bar was produced into a coil while the #5 (#16M) and #6 (#19M) bars were produced in 20 ft (6.1 m) long straight bars. The ASTM A706 Grade 80 was produced by Cascade Steel in McMinnville, OR as a special heat for this research project. Farwest Steel in Eugene, OR fabricated all the reinforcement and provided the Grade 60 material (also produced by Cascade Steel). Mechanical properties and chemical composition of the reinforcement are shown in Table 4-1 and Table 4-2 respectively. Note that the heat numbers are the same for both tables, heat numbers are not shown in Table 4-2 in order to fit the table on the page.

Table 4-1 Reinforcement mechanical and physical properties of reinforcement (Mill Data)

Bar size	ASTM A706 grade ksi (MPa)	Heat #	Yield ksi (MPa)	Tensile ksi (MPa)	Elong. % 8 in. (0.2 m)	Nom. WT %
#3 (#10M)	Gr. 60 (420)	087313	69.0 (476)	99.0 (683)	18	100
#5 (#16M)	Gr. 60 (420)	095113	65.5 (452)	97.5 (672)	16	100
#6 (19M)	Gr. 60 (420)	302213	66.5 (459)	97.0 (669)	17	95
#3 (#10M)	Gr. 80 (550)	083513	96.5 (665)	124.0 (855)	23	96
#5	Gr. 80	327612	87.5	114.0	13	96

(#16M)	(550)		(603)	(786)		
#6 (19M)	Gr. 80 (550)	327612	88.0 (607)	115.0 (793)	14	96

Table 4-2 Chemical composition of reinforcement (Mill data)

Bar size	ASTM A706 grade, ksi (MPa)	C	Mn	P	S	Si	Cu	Ni	Cr	Mo	V	CE
#3 (#10M)	Gr. 60 (420)	0.280	1.280	0.007	0.024	0.190	0.180	0.070	0.060	0.020	0.020	0.500
#5 (#16M)	Gr. 60 (420)	0.290	1.250	0.009	0.022	0.170	0.220	0.080	0.080	0.021	-	0.510
#6 (19M)	Gr. 60 (420)	0.300	1.220	0.018	0.022	0.190	0.250	0.090	0.140	0.020	0.025	0.530
#3 (#10M)	Gr. 80 (550)	0.270	1.340	0.008	0.018	0.190	0.220	0.080	0.080	0.01	0.102	0.500
#5 (#16M)	Gr. 80 (550)	0.290	1.300	0.011	0.00	0.230	0.360	0.090	0.050	0.017	-	0.520
#6 (19M)	Gr. 80 (550)	0.290	1.300	0.011	0.005	0.230	0.360	0.090	0.050	0.017	-	0.520

Testing was performed using a MTS Universal Testing Machine (UTM) connected to a Data Acquisition system (DAQ). The testing program was operated using Daisy Lab. The UTM force and displacement were recorded. Tension testing was performed on each size and grade of reinforcement following *ASTM E8/E8M-13a Standard Test Methods for Tension Testing of Metallic Materials* and *ASTM A370-12a Standard Test Methods and Definitions for Mechanical Testing of Steel Products*. Three samples were tested for each size and grade. A two inch (0.05 m) gage length extensometer meeting *ASTM E83-10a Standard Practice for Verification and Classification of Extensometer Systems* was used to determine yield behavior. Figure 4.1 shows a photograph of the test setup used. The extensometer was removed from the bar sample at the onset of necking to prevent damaging the extensometer. When analyzing the Grade 60 reinforcement stress-strain data, the strain values up to 12% were obtained by the extensometer. For the Grade 80 reinforcement the extensometer was used for strain values up to 14%. This corresponds to the minimum elongation percent for an 8 inch (0.2 m) gage length defined by

ASTM A706 for Grade 60 and the Grade 80 reinforcement respectively. After the extensometer was removed the UTM displacement was used to compute the strain of the sample. Note that necking occurred prior to the 12% strain value for the #3 (#10M) Grade 80 bar so the extensometer was only used to strain values up to 8%. The yield stress and strain were determined using the 0.2% offset method (based off the nominal modulus elasticity of steel reinforcement of 29,000 ksi (200 GPa)). As required by ASTM A706, the stress corresponding to a strain value of 0.0035 in./in.is also reported. The stress and strain values at the onset of strain hardening is defined here in as the point where the stress-strain curve begins to have a positive slope after the initial yield point. The tensile strength and corresponding strain are values obtained at the maximum stress. The ultimate strain and corresponding stress are values obtained at the maximum strain and directly prior to the bar fracturing. These data were procured for all bar sizes and grades. Table 4-3 shows a summary of the tensile test results and

Table 4-4 shows a summary of the tensile testing strain hardening results. Note the values of Table 4-3 and

Table 4-4 are from the same tensile tests but were separated into two tables due to space constraints.

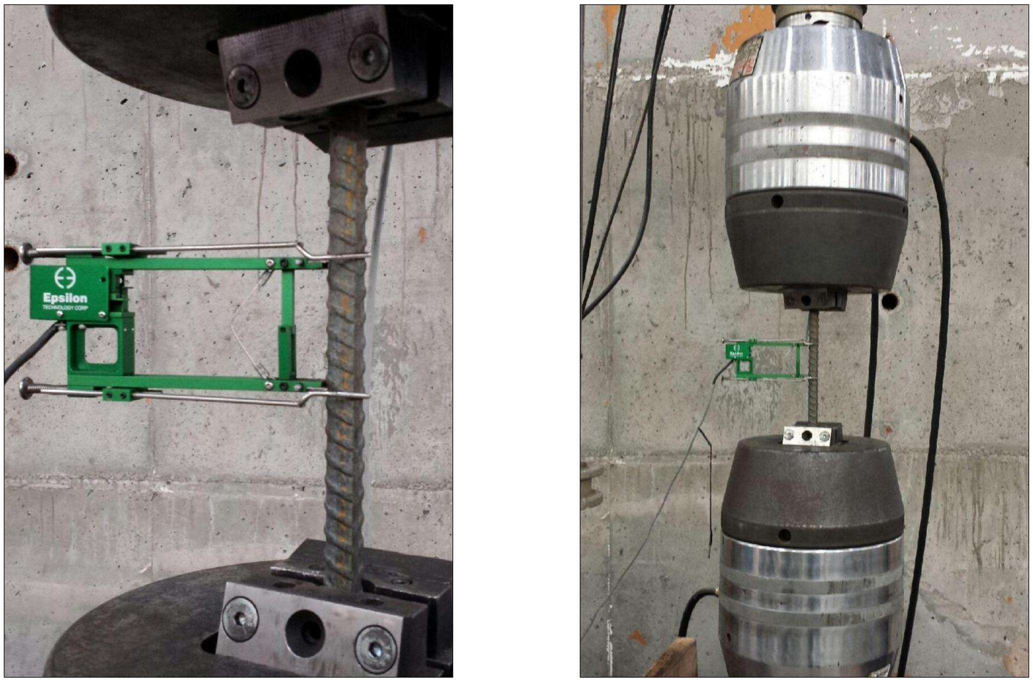

Figure 4.1 Photos of reinforcement tensile testing

Table 4-3 Summary of tensile testing results for reinforcing bar

Bar size	Grade, ksi (MPa)	Yield point (0.2% offset)		Yield point (0.0035 EUL*)		Tensile strength		Ultimate strain		Elong. % in 8 inch (0.2 m)
		Stress, ksi (MPa)	Strain, in./in. (m/m)	Stress, ksi (MPa)	Strain, in./in. (m/m)	Stress, ksi (MPa)	Strain, in./in. (m/m)	Stress, ksi (MPa)	Strain, in./in. (m/m)	
#3 (#10M)	Gr. 60 (420)	73.9 (510)	0.0045	71.9 (496)	0.0035	103.1 (711)	0.1104	73.2 (505)	0.1564	15
#5 (#16M)	Gr. 60 (420)	66.7 (460)	0.0043	66.7 (460)	0.0035	94.2 (649)	0.1274	71.6 (494)	0.1978	17
#6 (19M)	Gr. 60 (420)	67.2 (463)	0.0043	66.9 (461)	0.0035	100.4 (692)	0.1138	81.5 (562)	0.2153	16
#3 (#10M)	Gr. 80 (550)	83.4 (575)	0.0049	75.4** (520)	0.0035	121 (834)	0.0963	84.4 (582)	0.1410	13
#5 (#16M)	Gr. 80 (550)	86.2 (594)	0.0050	83.3 (575)	0.0035	114.8 (791)	0.1033	86.6 (597)	0.1555	14
#6 (19M)	Gr. 80 (550)	86.0 (593)	0.0050	83.9 (578)	0.0035	114.8 (792)	0.1172	93.9 (647)	0.1891	15

*EUL: Extension Under Load. ** did not meet specifications but other analysis methods indicate yield strength is greater than 80 ksi.

Table 4-4 Summary of tensile rebar testing strain hardening results

Bar size	Grade, ksi (MPa)	Strain hardening point	
		Stress, ksi (MPa)	Strain, in./in. (m/m)
#3 (#10M)	Gr. 60 (420)	N.A.	N.A.
#5 (#16M)	Gr. 60 (420)	65.6 (453)	0.0118
#6 (19M)	Gr. 60 (420)	67.1 (462)	0.0038
#3 (#10M)	Gr. 80 (550)	N.A.	N.A.
#5 (#16M)	Gr. 80 (550)	86.1 (594)	0.0085
#6 (19M)	Gr. 80 (550)	95.6 (590)	0.0090

N.A.: not available for the #3 reinforcing bar; this reinforcing bar exhibited a “round house” stress strain curve and did not exhibit yield plateau; as such, strain hardening data could not be determined.

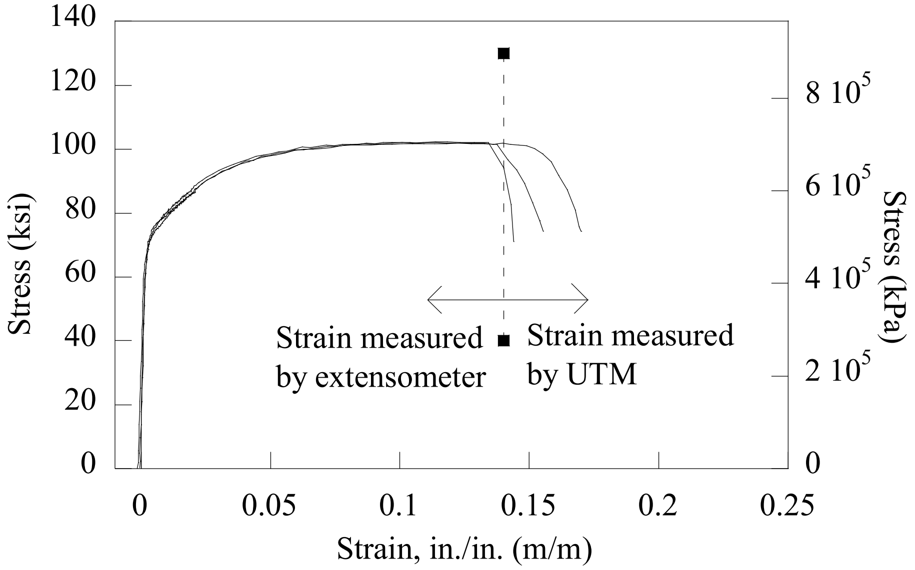

Figure 4.2 Stress-strain plot of Grade 60 #3 (#10M) reinforcing bars

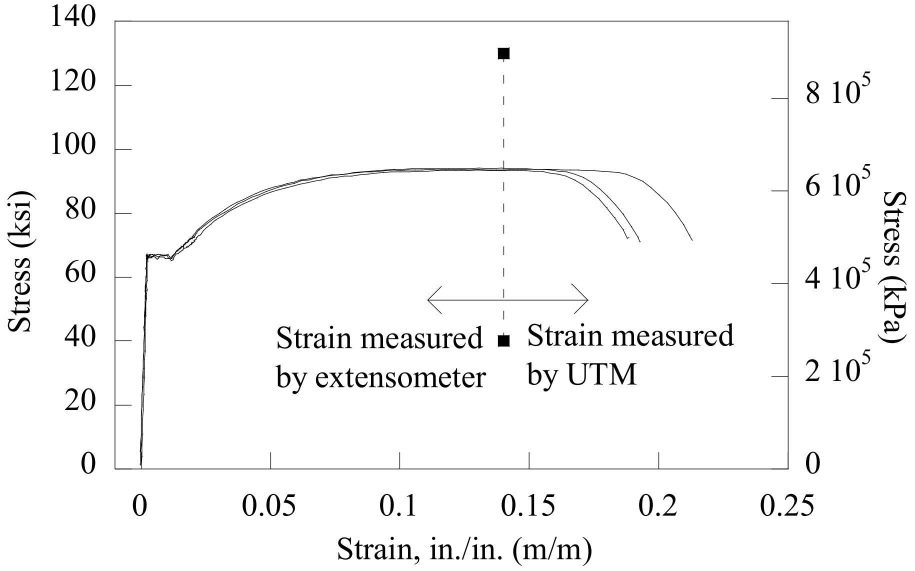

Figure 4.3 Stress-strain plot of Grade 60 #5 (#16M) reinforcing bars

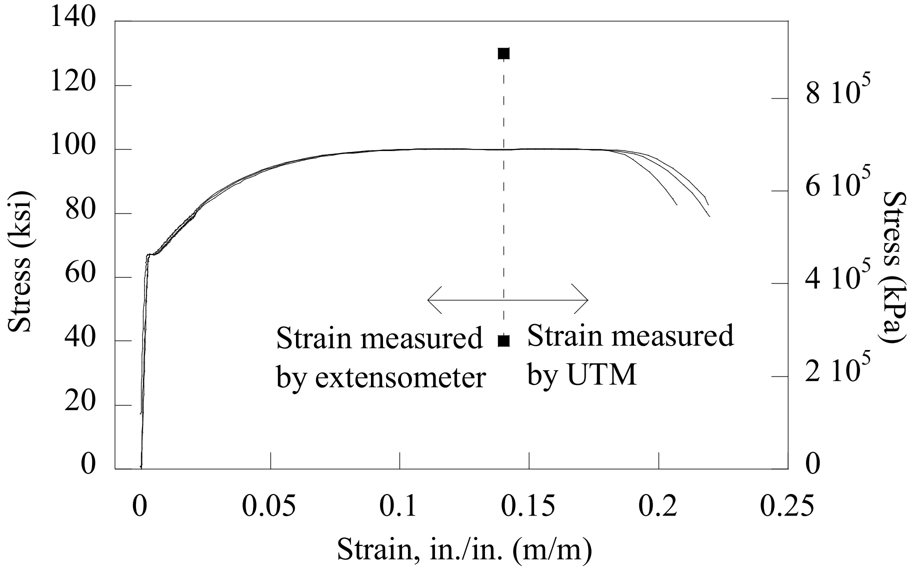

Figure 4.4 Stress-strain plot of Grade 60 #6 (#19M) reinforcing bars

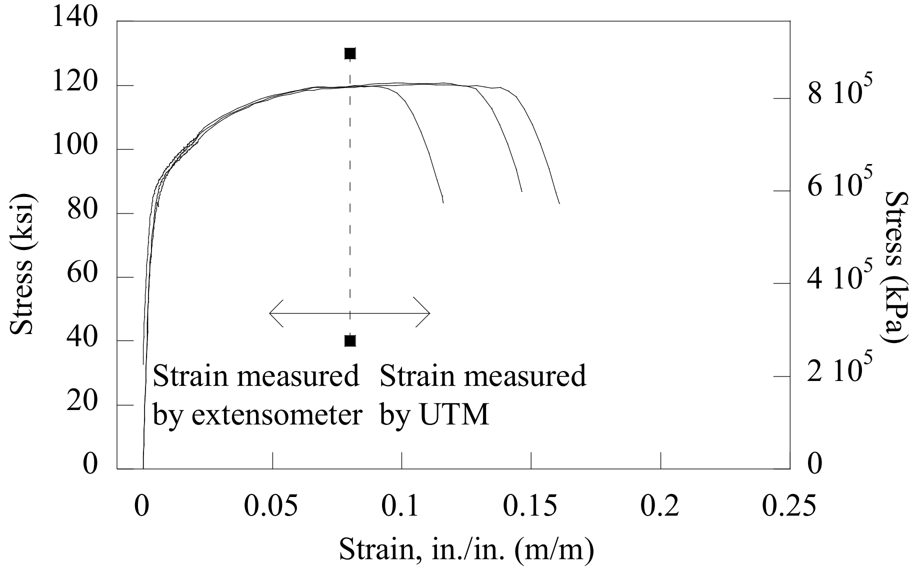

Figure 4.5 Stress-strain plot of Grade 80 #3 (#10M) reinforcing bars

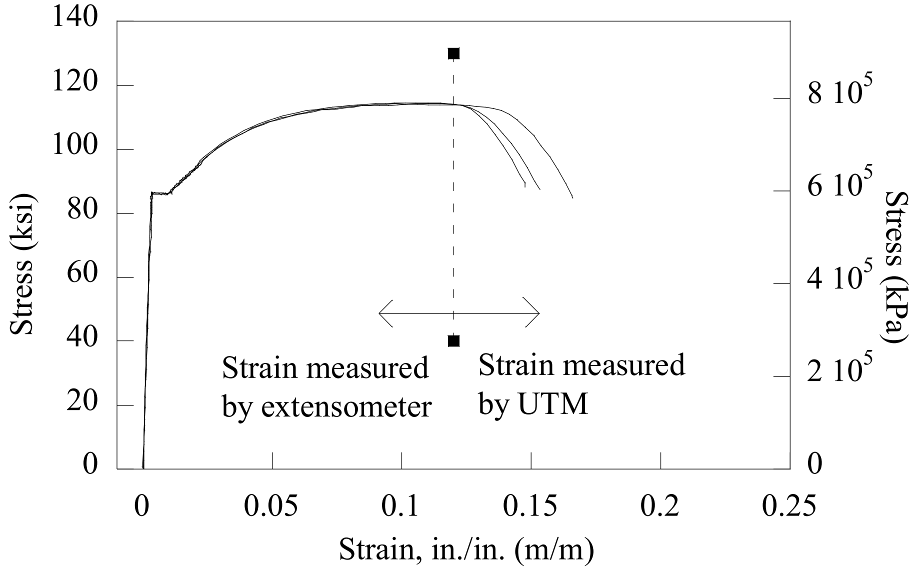

Figure 4.6 Stress-strain plot of Grade 80 #5 (#16M) reinforcing bars

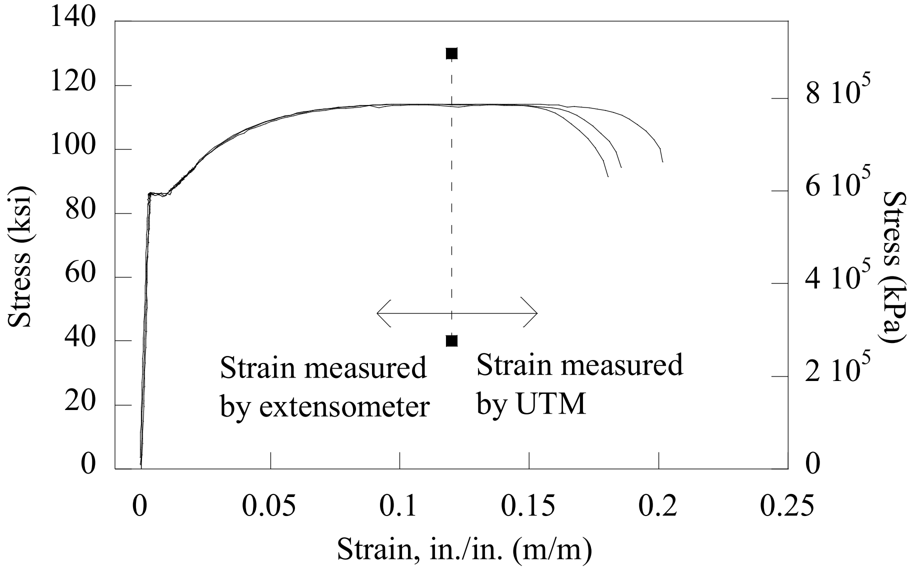

Figure 4.7 Stress-strain plot of Grade 80 #6 (#19M) reinforcing bars

4.2 Concrete

All concrete used in the construction of the test specimens was supplied by Knife River Corporation (Corvallis, OR). The concrete mixture contained a 3/8 inch (0.00953 m) maximum size aggregate (half scale of typical 3/4 inch (0.0191 m) and had a 28-day design compressive strength of 4 ksi (28 MPa). The mixture was also proportioned to be pumpable and had a minimum required slump of 5 inches (0.127 m). The same mixture proportions were used for all specimens. A matrix of the tests conducted to characterize the concrete is shown in

Table 4-5. The mixture proportions are shown in Table 4-6. A summary of the concrete properties are shown in Table 4-7. All concrete samples were made and cured following *ASTM C31/31M-12 Standard Practice for Making and curing Concrete Test Specimens in the Field* for making and curing specimens in the field. The standard cylinder size, 4-inch (0.102 m) diameter by 8 inches (0.203 m) tall, was used for compression strength testing according to *ASTM C39/39M-12a Standard Test Method for Compressive Strength of Cylindrical Concrete Specimens*, Modulus of elasticity (MOE) testing according to *ASTM C469/469M-10 Standard Test Method for Static Modulus of Elasticity and Poisson's Ratio of Concrete in Compression*, and splitting tensile testing according to *ASTM C496/496M-11 Standard Test Method for Splitting Tensile Strength of Cylindrical Concrete Specimens*. Six inch (0.152 m) by 6 inch (0.152 m) by 20 inch (0.508 m) standard beams were used for modulus of rupture (MOR) testing according to *ASTM C78/78M-10 Standard Test Method for Flexural Strength of Concrete (Using Simple Beam with Third-Point Loading).* All concrete samples were stored next to the test columns to match curing conditions of the columns. Cylinders were demolded at the same time as the formwork on the columns was removed. Both ends of all concrete test cylinders were mechanically ground prior to compression testing to prevent eccentric loading.

Table 4-5 Concrete testing matrix

Sample	Compressive Strength (ASTM C39)	Tensile Strength (ASTM C496)	Modulus of Elasticity (ASTM C469)	Modulus of Rupture (ASTM C78)
Column and Header	3-day, 7-day, 14-day, 28-day, days of testing	7-day, 28-day, days of testing	7-day, 28-day, days of testing	28-day, days of testing
Footing	7-day, 14-day, 28-day	Not tested	Not tested	Not tested

Note: The footing concrete samples were only tested to confirm the 28-day strength and to determine when the footing formwork could be safely removed.

Table 4-6 Concrete Mix Proportions per Cubic Yard (meter)

Mix	W/(C+P) Ratio	Coarse Agg. (3/8 in) lbs (kg)	Fine Agg. (sand) lbs (kg)	Fine Agg. (mansand) lbs (kg)	Cement lbs (kg)	Fly Ash lbs (kg)	Water gal (L)	Ad. Mix. (WRDA_64) oz (g)
Average of all pours	0.47	1193 (541)	1597 (724)	278 (126)	506 (230)	91 (41)	20 (74)	24 (680)

Table 4-7 Summary of concrete properties for columns C1 and C2

Sample	Compressive Strength (ASTM C39), ksi (MPa)	Tensile Strength (ASTM C496), ksi (MPa)	Avg. Modulus of Elasticity (ASTM C469), ksi (GPa)	Modulus of Rupture (ASTM C78), ksi (MPa)
Column C1/C2 Footing 28-Day	4.247 (29.28)	Not tested	Not tested	Not tested
Column C1/C2 day of C1 test (28-day)	4.770 (32.89)	0.682 (4.7)	3,011 (20.76)	0.507 (3.5)
Column C1/C2 day of C2 test (35-day)	4.837 (33.35)	0.677 (4.67)	2,585 (17.82)	0.539 (3.72)

Chapter 5

EXPERIMENTAL RESULTS FOR COLUMNS C1 AND C2

5.1 Introduction

This section provides test rest results from two column tests specimens; one column constructed with Grade 60 reinforcing bars (C1) and one column constructed with Grade 80 reinforcing bars (C2). The main objective of the testing is to assess the performance of the columns when subjected to cyclic loading when both columns are designed to have approximately the same lateral strength. Both columns were designed following the same standard.

The column testing procedure was described in Chapter 3. All results presented herein are divided into visual and measured observations. Visual observations refer to cracking, concrete spalling, bar buckling, and bar fracture. Measured observations include column lateral displacement, steel reinforcement strains, column curvature, column tilt, horizontal applied load, and footing displacement. All data are analyzed until first bar fracture.

5.2 Column C1 Experimental Results

5.2.1 Cracking

Crack mapping was performed after the final two peaks of each displacement cycle. Figure 5.1 shows two photos of the crack mapping near the end of the testing. It can be seen that cracking was primarily dominated by flexure and cracking extended to approximately half the column height.

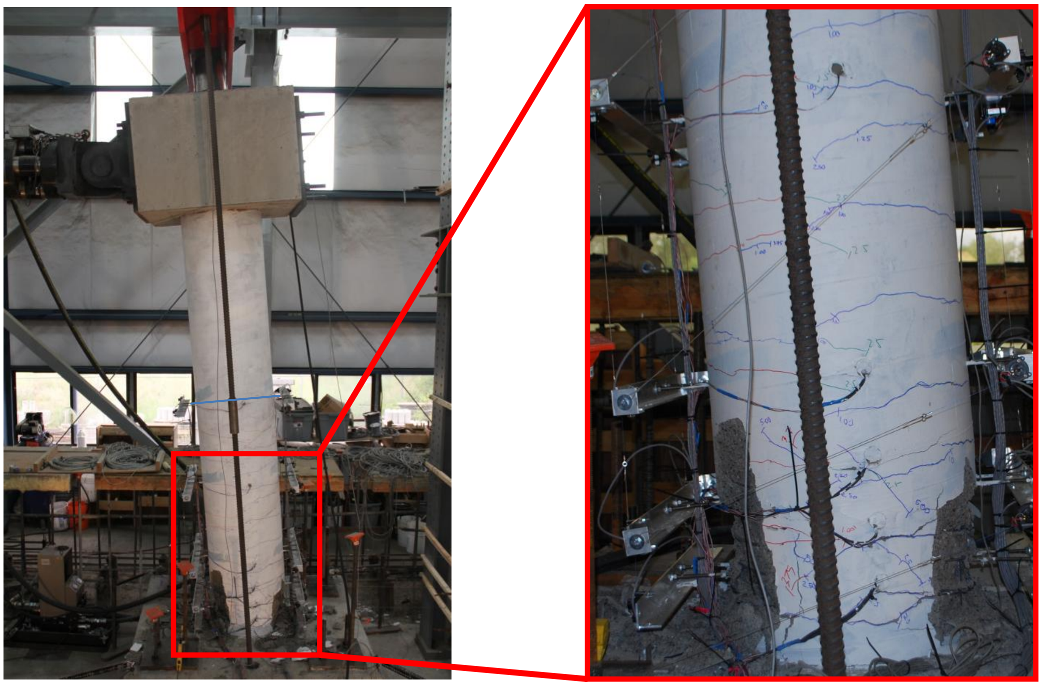

Figure 5.1 Column C1 crack mapping

5.2.2 Concrete Spalling

To assess time to spalling, the researches recorded the displacement cycle at the onset of concrete spalling, at concrete delamination, and at deep concrete spalling. Onset of concrete spalling is defined as the time (or in this case, cycle) when the concrete cover begins to exhibit cracking. Concrete delamination is defined here as the cycle when the concrete cover separates
Table 5-1 provides a summary of the concrete spalling and delamination values. All spalling and
from the column core—note that this occurs on the faces in line with the loading direction. Deep
delamination occurred after the longitudinal reinforcement yielded.
concrete spalling is defined as the cycle when the concrete core begins to crush.

Table 5-1 Summary of column C1 concrete spalling

	Onset of concrete spalling	Concrete delamination	Deep concrete spalling
Displacement cycle	2.50 (0.064)	3.75 (0.095)	6.25 (0.159)

in. (m)			

5.2.3 Bar Buckling

When the researchers were mapping the cracks, a visual assessment of the reinforcement was also performed to assess if the longitudinal bars exhibited buckling. The first longitudinal bar buckled on the second to last peak of the 7.5 inch (0.191 m) displacement cycle. Figure 5.2 shows a photo of the first bar that buckled. This bar was the longitudinal bar that was furthest south. The apex of the buckled bar was located approximately 6 inches (0.152 m) from the base of the column. Figure 5.2 shows the reinforcing bar buckled in very close proximity to the location of the strain gage. The silver tape in the photo is part of the protection for the strain gages and is believed to not have influenced the buckling of the reinforcing bar. However, the very slight reduction in area of the reinforcing bar cross-sectional area where the strain gage was installed may have influenced where the reinforcing bar buckled.

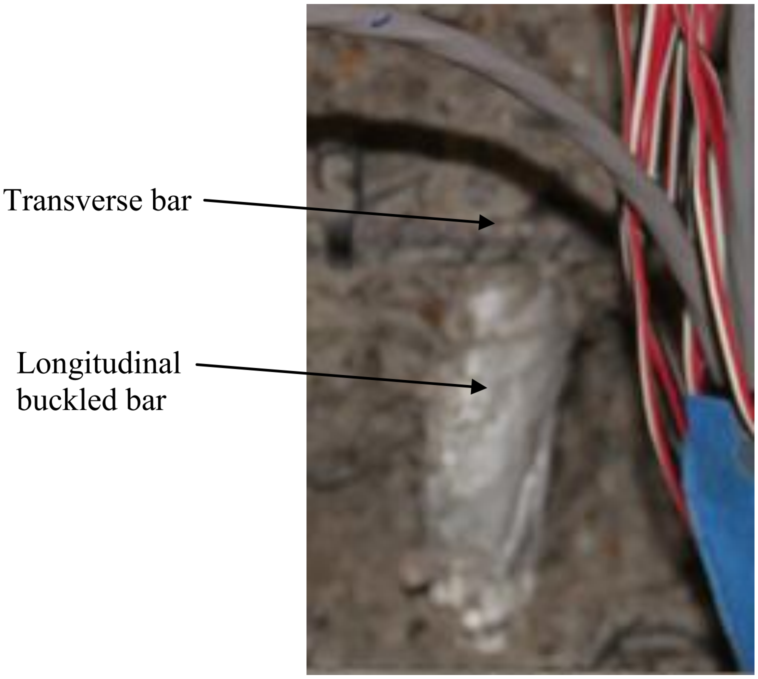

Figure 5.2 Photograph of column C1 bar buckling

5.2.4 Bar Fracture

The first longitudinal bar fractured at the final peak of the 7.5 inch (0.191 m) displacement cycle with an applied load of 27.22 kips (121.1 kN). The tip displacement was 7.51 inches (0.191 m)—the tip displacement is defined here as the displacement measured with the string potentiometer attached to the center of the north face of the header. Observations indicate that the bar fractured after a microcrack formed due to the bar buckling. The southernmost longitudinal bar fractured at an elevation approximately 6 inches (0.152 m) from the base of the column. Figure 5.3 shows the fractured reinforcing bar—note that it is in very close proximity to the location of the strain gage. The silver tape in the photo is part of protection for the strain gages and is believed to not have influenced the buckling or the fracture of the reinforcing bar.

However the slight reduction in the reinforcing bar cross-sectional area may have impacted the location where the reinforcing bar buckled and fractured.

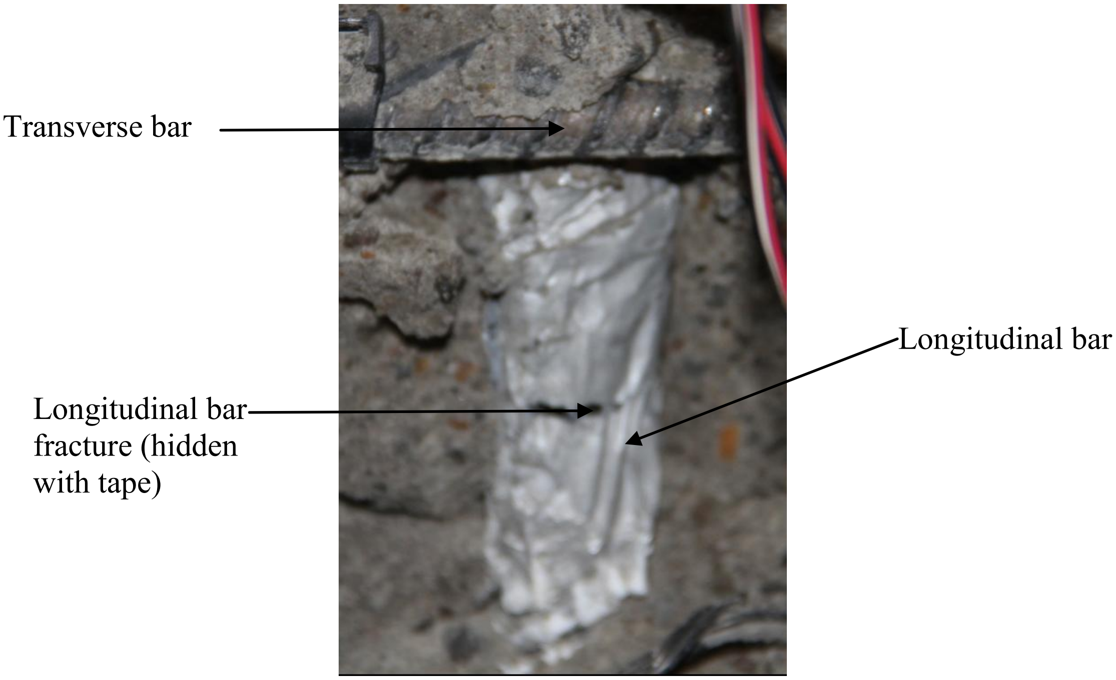

Figure 5.3 Photograph of column C1 first bar fracture

5.2.5 Column Lateral Displacement

The lateral displacement of the column was measured at six points along the height of the column. Locations of each point were provided in Chapter 3. Figure 5.4 shows the maximum and minimum lateral deflection at the 6 points for the 11 displacement cycles. The elevation is normalized with respect to the column diameter, D, and the lateral displacement, Δ, is normalized by the column test height, H.

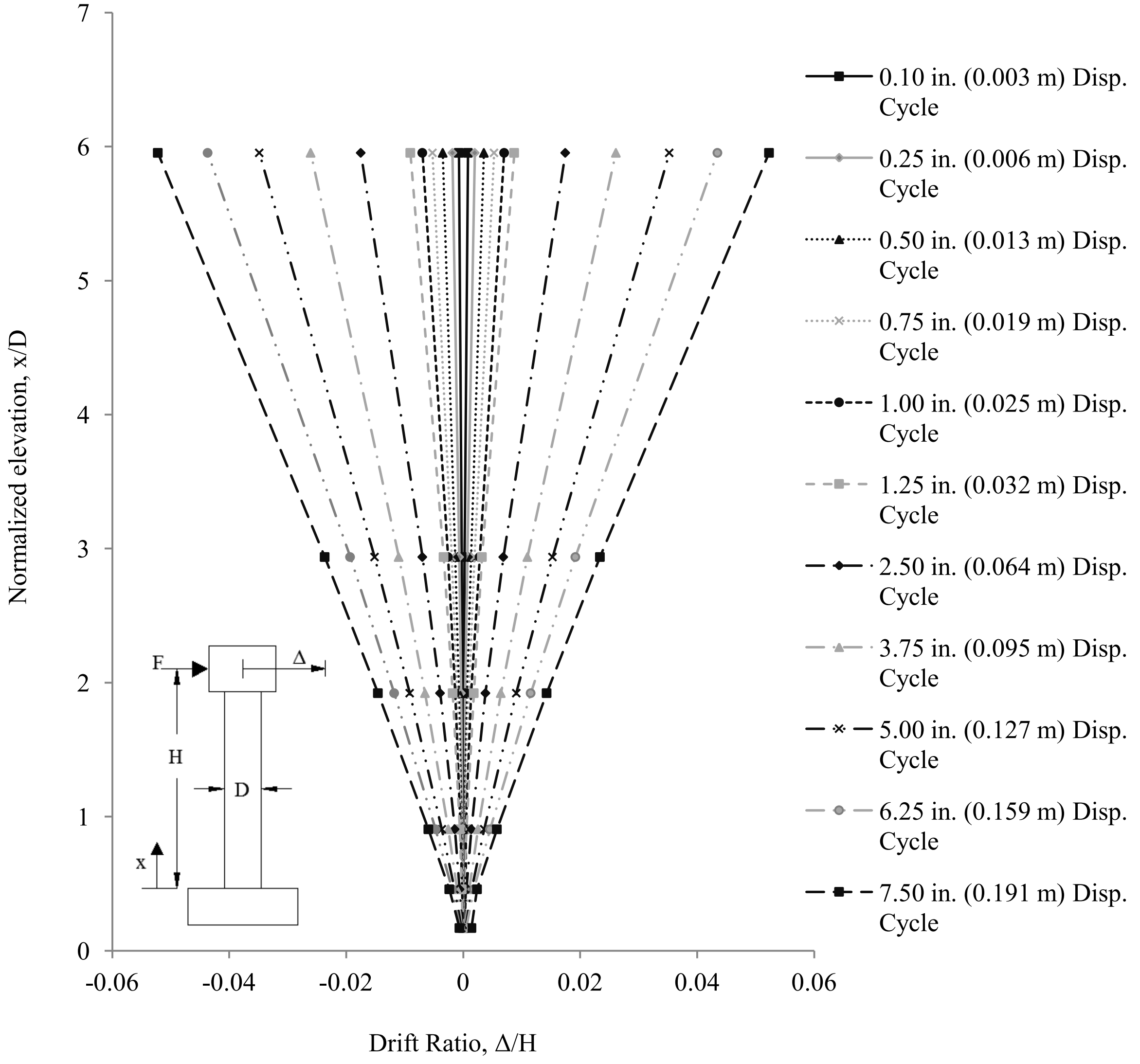

Figure 5.4 Column C1 drift ratio along the columns height

5.2.6 Reinforcing Bar Strains

Reinforcing bar strains were recorded on both the longitudinal and transverse reinforcement. Locations of strain gage are provided in Chapter 3. Figure 5.5 shows the maximum transverse reinforcement steel strains in column C1 for each displacement cycle along the height of the column. The elevation is normalized by the column diameter, D, and the steel strain is normalized by the yield strain of the transverse reinforcement. The yield strain is defined as yield stress determined using the 0.2% offset method divided by the nominal modulus of elasticity (MOE), 29,000 ksi (200 GPa). Note that only the maximum strains are shown because the transverse reinforcement never goes into compression during testing. Table 5-2 shows the yield strain values used to determine the normalized yield strain. Note that normalized strain values in Figure 5.5 and Figure 5.6 represent the 11 cycles with normalized strains for the smallest cycles on the bottom of the stacks, and the largest cycles on the top.

Figure 5.6 shows the maximum longitudinal reinforcement steel strains for column C1. Note that the longitudinal strains are both depending on the positive and negative displacement cycle. The maximum positive displacement cycle corresponds to the maximum tension strain. The maximum negative displacement cycle corresponds to the maximum compressive strain. The ordinate in the figure is normalized by the column diameter, D, and the steel strain is normalized by the yield strain of the longitudinal reinforcement. The yield strain was computed in the same manner as the transverse yield strain. The normalized strain values are stacked in the same order as the transverse reinforcement strain plot.

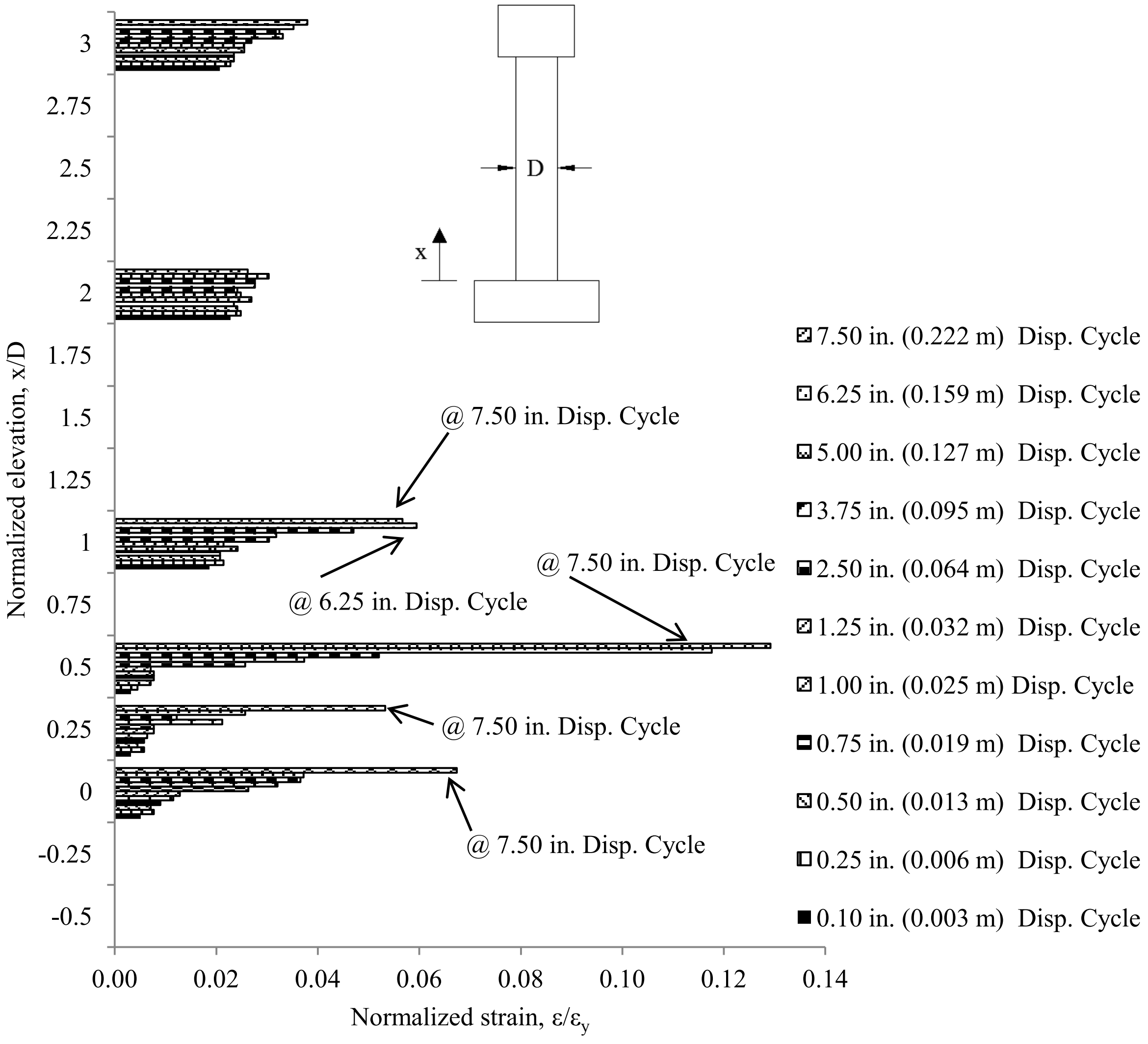

Figure 5.5 Column C1 transverse strains of transverse reinforcement

Table 5-2 Column C1 yield strains used in the strain analysis

Reinforcement	Yield strain	Yield stress ksi (MPa)	MOE ksi (GPa)
#3 (#10M) Grade 60 ksi (420 MPa)	0.00255	73.9 (510)	29,000 (200)
#5 (#16M) Grade 60 ksi (420 MPa)	0.00230	66.7 (460)	29,000 (200)

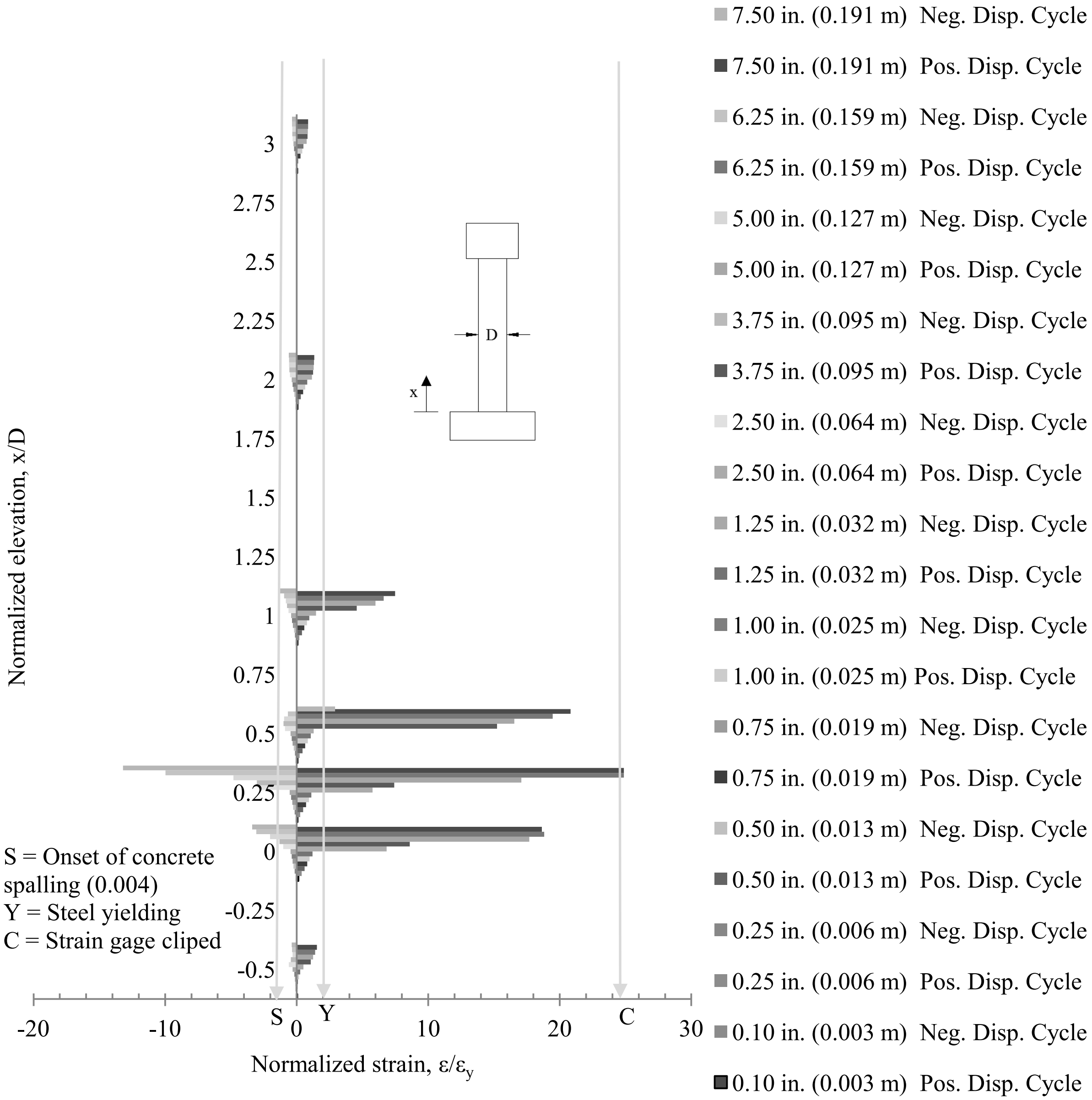

Figure 5.6 Column C1 longitudinal strains

5.2.7 Column Curvature

Flexural deformations of the columns can be determined using the rotation of columns segments, measured using a pair of left and right linear potentiometers located at the left and right chords. This assessment and analysis assumes that the Bernoulli hypothesis, that plane sections remain plane after deformation, is valid. Figure 5.7 shows the physical representation of the variables used in the curvature analysis. The change of slope between two sections (e.g., Sections a and b) is given by:

$$\theta ba=\frac{\Delta S2-\Delta N2}{hp} \qquad \text{(Eq. 5.1)}$$

where ΔS2 and ΔN2 are the extensions and shortening of the left (south) and right (north) column chords measured using a pair of string potentiometers at section b relative to section a and hp is the horizontal distance between the north and south string potentiometers (e.g., ΔS2 and ΔN2). Thus, the column end deflection obtained from the change of slope between a and b can be determined as follows:

$$b\Delta c,fl=\frac{\Delta S2-\Delta N2}{hp}\left(H-xb\right) \qquad \text{(Eq. 5.2)}$$

where H is the column test height and xb is the vertical distance to the centroid of section b measured from the top of the footing face. Using the same procedure the flexural deformation of another portion of the column can be determined using the change in slope between sections b and c as follows:

$$c\Delta c,fl=\frac{\Delta S3-\Delta N3}{hp}\left(H-xc\right) \qquad \text{(Eq. 5.3)}$$

where ΔS3 and ΔN3 are the extensions and shortening of the left (south) and right (north) column chords measured using a pair of string potentiometers at section c relative to section b.

This same procedure can be used to determine the slope between sections c and d and to determine the slope between sections d and e. The sum of the discrete column flexural deformation gives the total column flexural deformations, Δc,fl:

$$\Delta c,fl=b\Delta c,fl+c\Delta c,fl+d\Delta c,fl+e\Delta c,fl \tag{Eq. 5.4}$$

The fixed-end rotation of the column can be estimated using a pair of linear string potentiometers placed a short distance (6 inches (0.153 m)) from the top of the footing face. As shown in Figure 5.7, the column and lateral movement due to the fixed-end rotation can be estimated as:

$$\Delta c,fe=\theta fe(H\text{-}xa)=\frac{\Delta S1\text{-}\Delta N1}{hp}\left(H\text{-}xa\right) \tag{Eq. 5.5}$$

where hp is the distance between the pair of linear string potentiometers nearest to the top of the footing, ΔS1 and ΔN1 are the extensions and shortening measured from the string potentiometers to the south and north of the column.

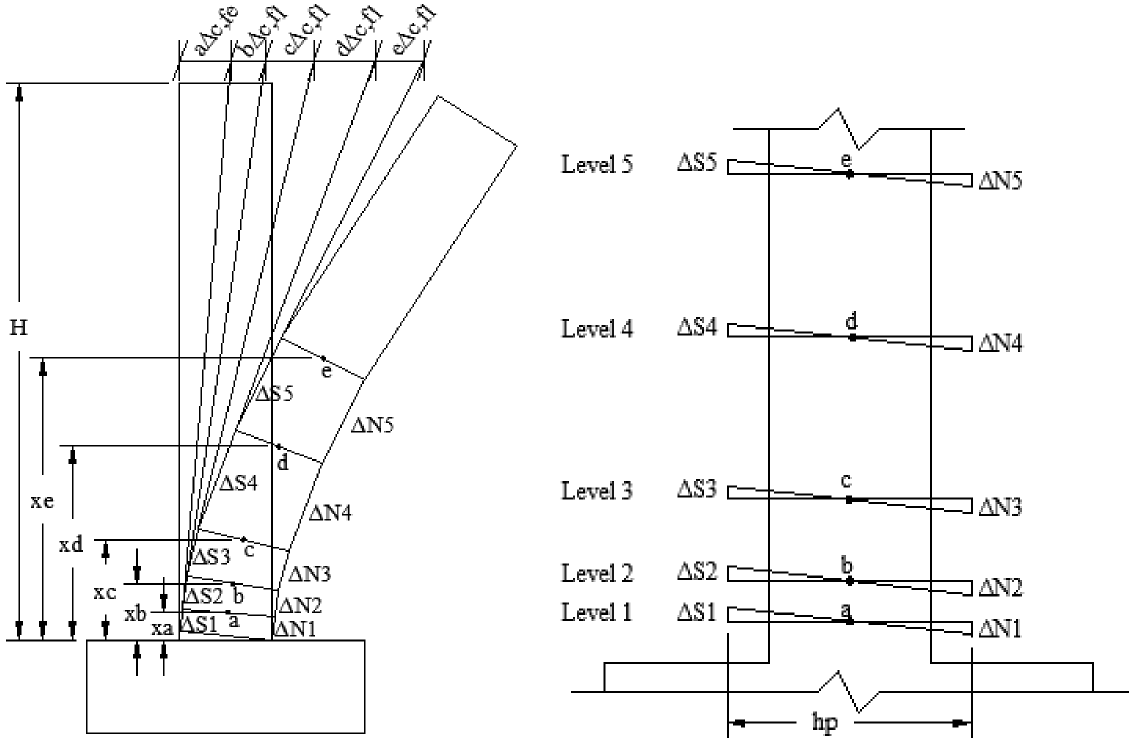

Figure 5.7 Physical representation of variables used in the curvature analysis

There are three main sources contributing to the fixed-end rotation. One contribution is from the deformations of the reinforcing bars passing through the joint core. Another contributing factor is from the global slippage of the reinforcing bars. The last source is the actual flexural deformation of the first 6 inches (0.153 m) of the column.

The method adopted here to compute the deformations is approximate because the contributions of reinforcing bar elongation (strain penetration) and bond slip cannot be separated with this experimental setup.

The relative curvature is computed at each of the five instrumentation levels described in Chapter 3 for each displacement level. The elevation and curvature are both normalized by the column diameter, D. The elevation is divided by the column diameter, D, and the curvature is multiplied by the column diameter, D. The calculation procedure used to determine the relative curvature at each level, I, is as follows:

(1) Compute ΔNi and ΔSi:

$$\Delta Ni=\frac{\Delta NEi+\Delta NWi}{2}$$

$$\Delta Si=\frac{\Delta SEi+\Delta SWi}{2}$$

where ΔNEi and ΔNWi are the measured changes in lengths of the curvature string potentiometers on the north side of the column at level, i, and ΔSEi and ΔSWi are the measured change in length of the curvature string pots on the south side of the column at level, i, respectively. The values of ΔNi and ΔSi are the average change in lengths of the curvature string potentiometers at each level, i, on the north and south sides respectively.

(2) Compute the maximum Δ at each level for each displacement cycle as follows:

$$\Delta i=\Delta Si-\Delta Ni$$

where Δi is the total change in length of the curvature string potentiometers at each level, i. This value is used as the vertical component of a right triangle to compute the relative rotation, θ, at each level, i.

(3) Compute the relative rotation, θ, at each level, i, as follows:

$$\Delta\theta i = \frac{\Delta i}{hp}$$

where Δθi is the relative rotation at each level, i.

(4) Compute the relative curvature, Ψ, at each level, i, as follows:

$$\Psi i = \frac{\Delta\theta i}{\Delta i}$$

where Ψi is the relative curvature at each level, i. Figure 5.8 shows the relative curvature for each displacement cycle along the height of the column.

5.2.8 Column Tilt

The column tilt is measured using a tilt sensor mounted at the center of east face of the header and using a string potentiometer attached to the center of the north face of the header. Figure 5.9 shows a plot of the measured tilt (from tilt sensor) and the calculated tilt (from the string potentiometer) versus the applied force. Note that the tilt sensor was used only to validate the string potentiometer measurements. The calculated tilt is the tip displacement divided by the column height converted into degrees. As shown in the plot there is an increasing difference between the measured tilt and the calculated tilt as the applied force reaches its maximum and minimum values. This is likely due to the positioning of the string pot that measures the tip displacement. As the column is being pushed horizontally the column also bends creating an additional vertical component measured by the string pot.

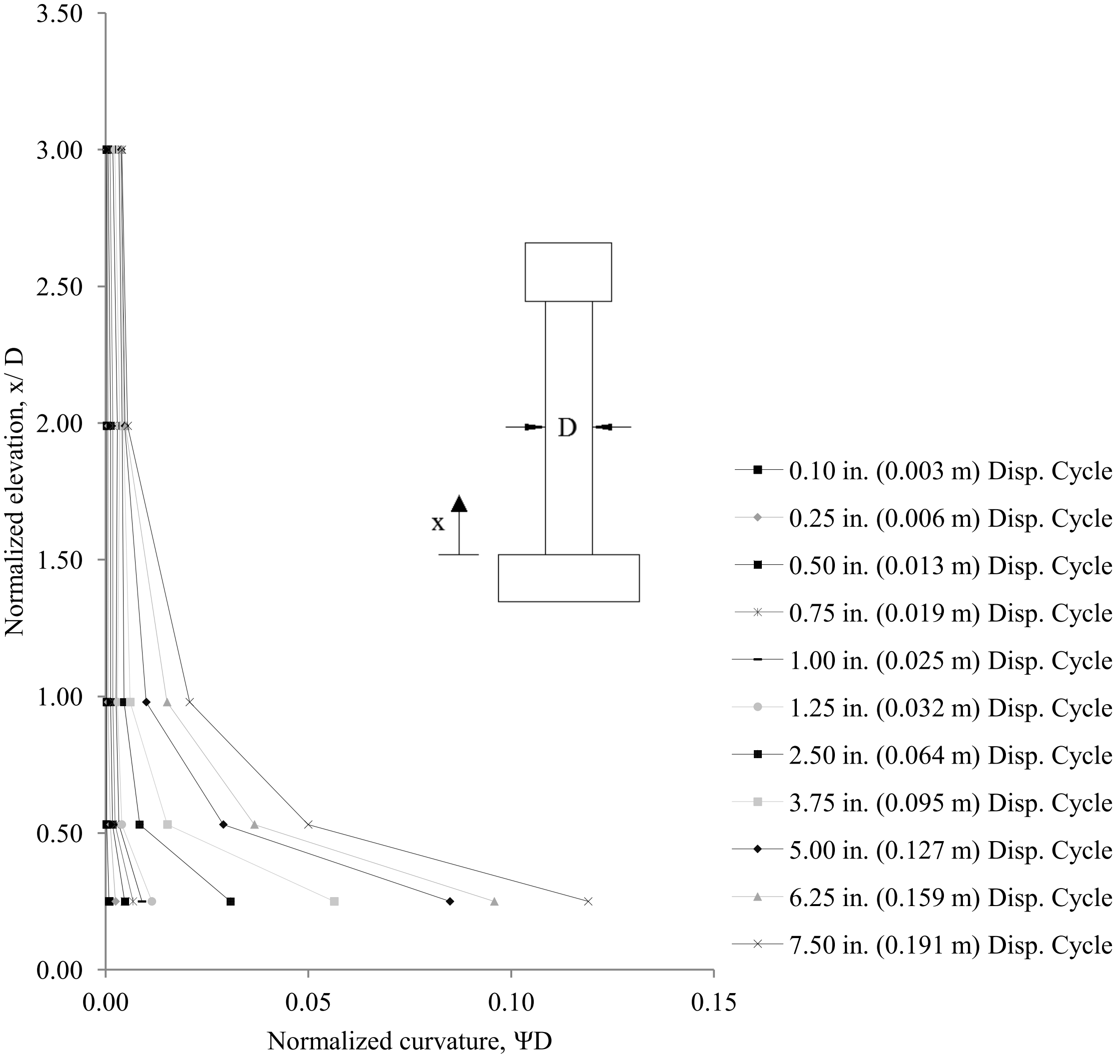

Figure 5.8 Column C1 normalized curvature with respect to the column diameter, D

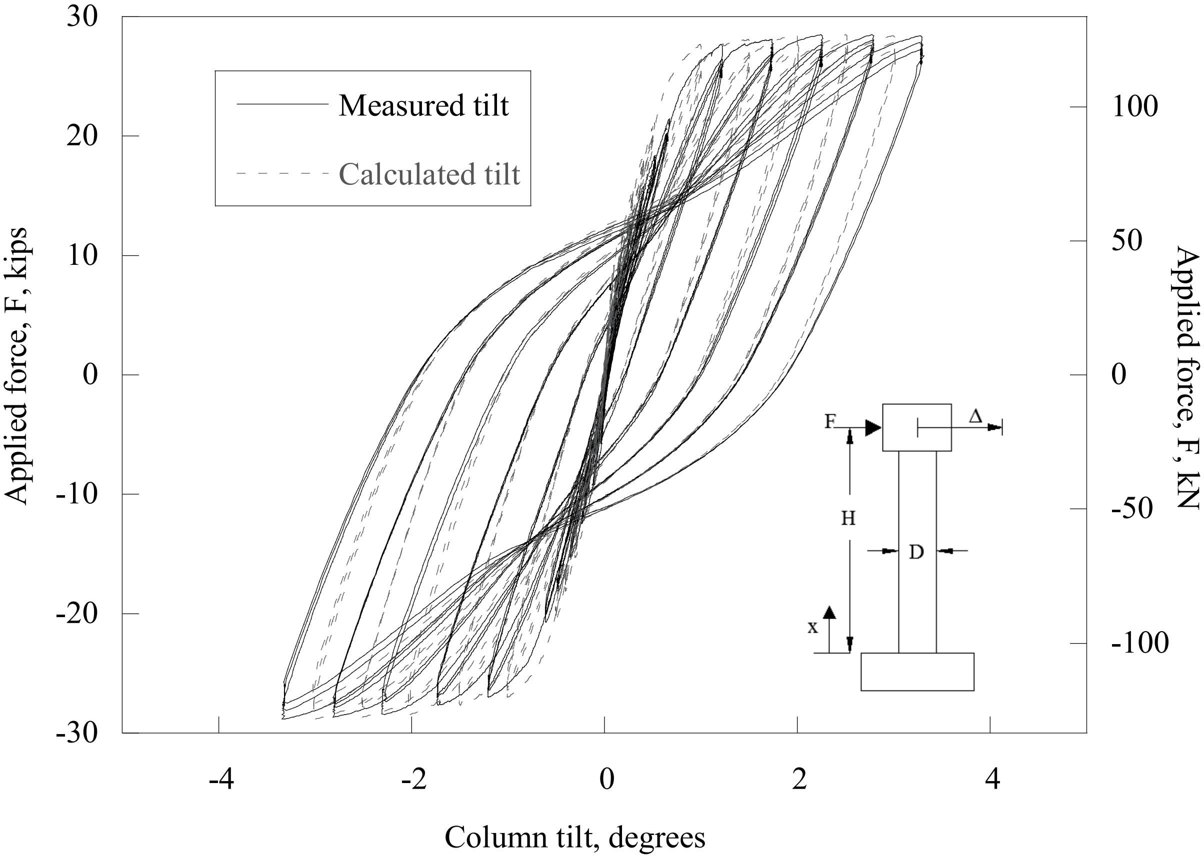

Figure 5.9 Column C1 tilt versus applied force

5.2.9 Horizontal Load

The applied horizontal load was measured using a group of parallel load cells within the actuator.

Figure 5.10 shows the applied load versus the drift ratio. The maximum applied force was 28.86 kips (128.4 kN) and the maximum drift ratio was 0.0527.

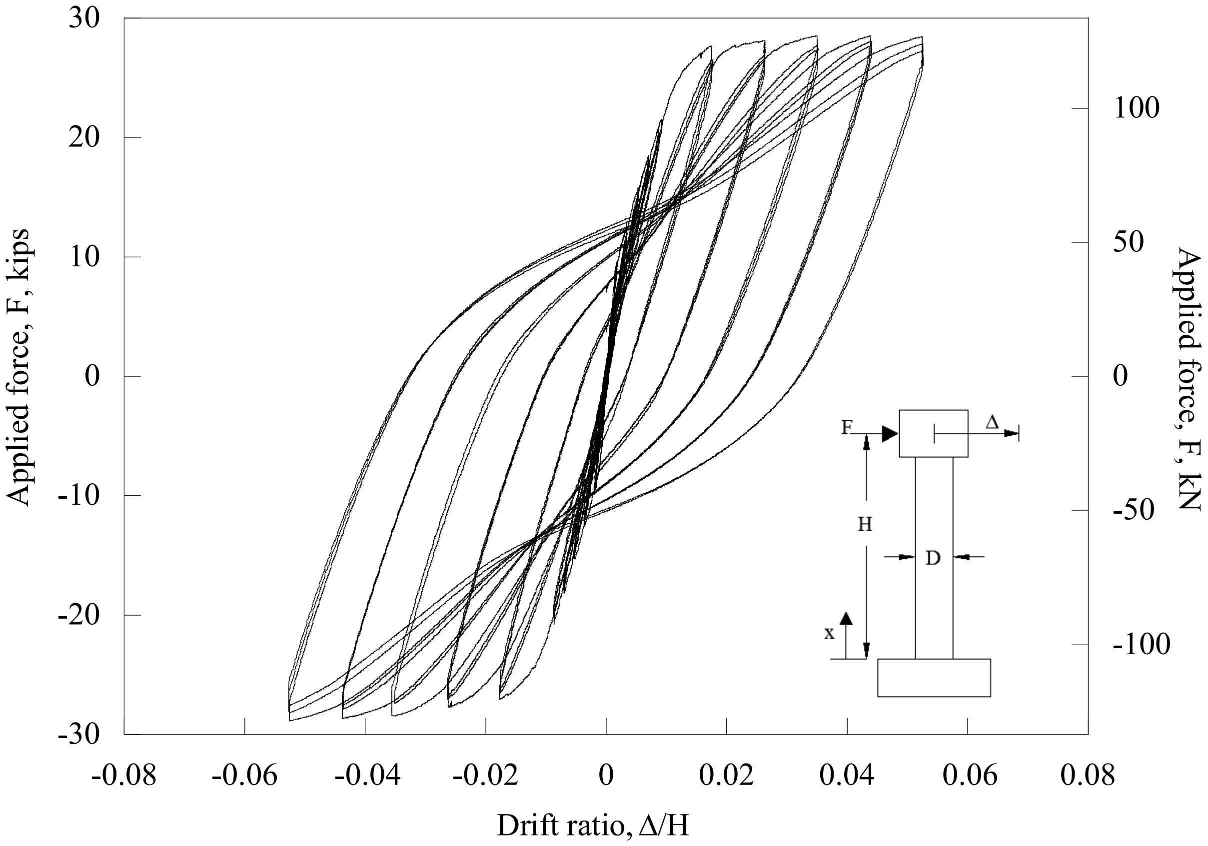

Figure 5.10 Column C1 applied force versus drift ratio

5.2.10 Vertical Load

The applied axial (vertical) load was measured using a load cell placed between the hydraulic jack and the column header. The initial axial load was set to 90 kips (400 kN). A pneumatic nitrogen charged accumulator was used to minimize changes in the axial load during testing. As shown in

Figure 5.11, the axial load increased as the applied horizontal load increased. This is due to the prestressing bars being stressed as a result of the lateral displacement of the column. The axial load also dropped below 90 kips (400 kN) during the larger displacement cycles. This is likely due to the reduction in axial stiffness of the column as a result of concrete cracking and spalling.

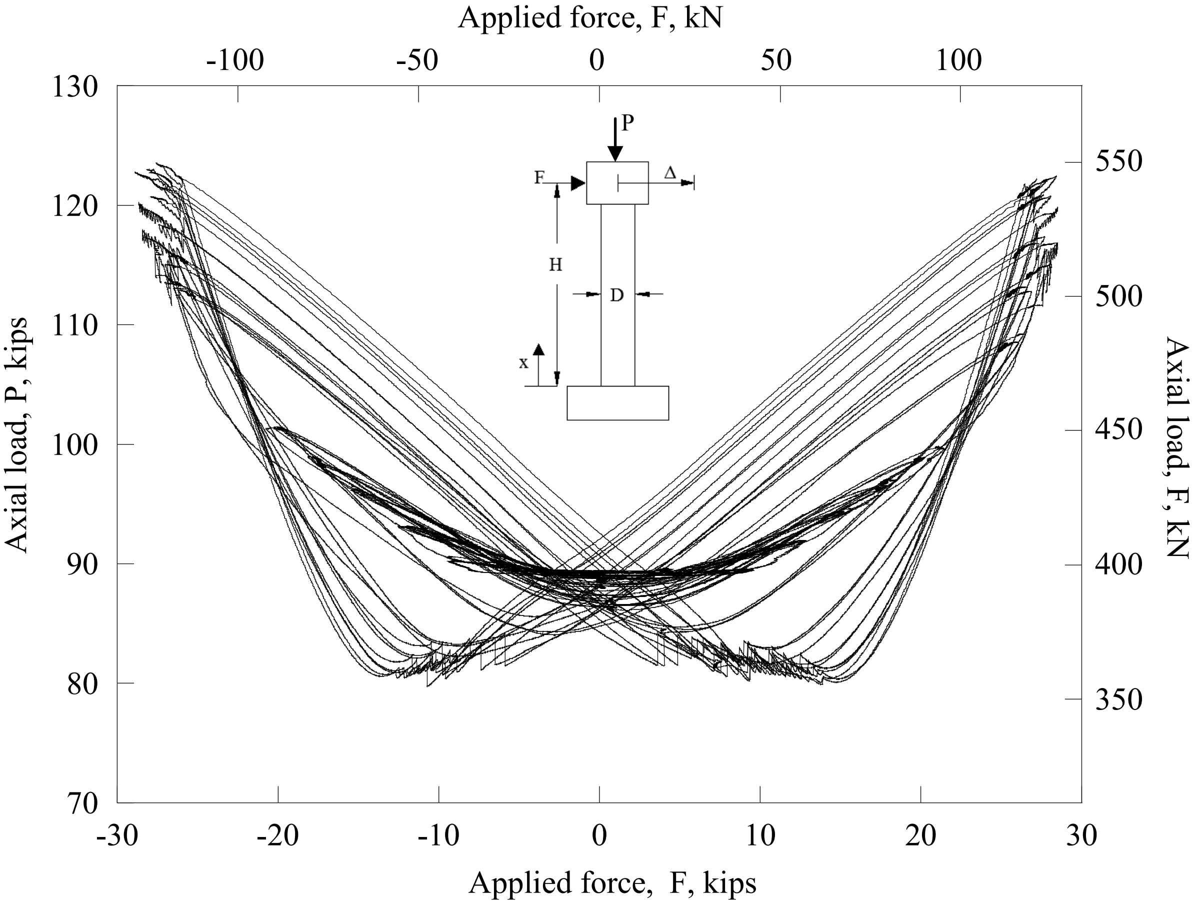

Figure 5.11 Column C1 axial load versus applied load

5.2.11 Footing Displacement

The footing was instrumented with four vertical LVDTs at each corner of the footing top face and two LVDTs on the north face of the footing. These LVDTs were used to determine if the footing rotated or was displaced laterally during the testing. The data from the six LVDTs showed that there was neither significant rotation nor horizontal displacement of the footing. LVDT recordings never exceeded 0.03 inches (0.0007 m).

5.3 Column C2 Experimental Results

5.3.1 Cracking

As with column C1, crack mapping was performed at the final two peaks of each displacement cycle. Figure 5.12 shows two photographs of the crack mapping near the end of the testing. The figure shows that cracking was primarily dominated by flexure and progressed to shear dominated cracks towards larger displacement cycles. Cracking extended to approximately two thirds the column height.

Figure 5.12 Column C2 crack mapping

5.3.2 Concrete Spalling

The displacement cycles at the onset of concrete spalling, concrete delamination, and deep concrete spalling were recorded. Table 5-3 provides a summary of the concrete spalling and delamination. As with column C1, all spalling and delamination occurred after the longitudinal reinforcement yielded.

Table 5-3 Summary of column C2 concrete spalling

	Onset of concrete spalling	Concrete delamination	Deep concrete spalling
Displacement cycle in. (m)	2.50 (0.064)	3.75 (0.095)	8.75 (0.222)

5.3.3 Bar Buckling

At the time of crack mapping the column was inspected to determine if any of the longitudinal bars had buckled. The first longitudinal bar buckled on the south side of the column during the 8.75 inch (0.222 m) displacement cycle. Figure 5.13 shows a photo of the first reinforcing bar that buckled. . The apex of the buckled reinforcing bar was located approximately 8.5 inches (0.216 m) from the base of the column.

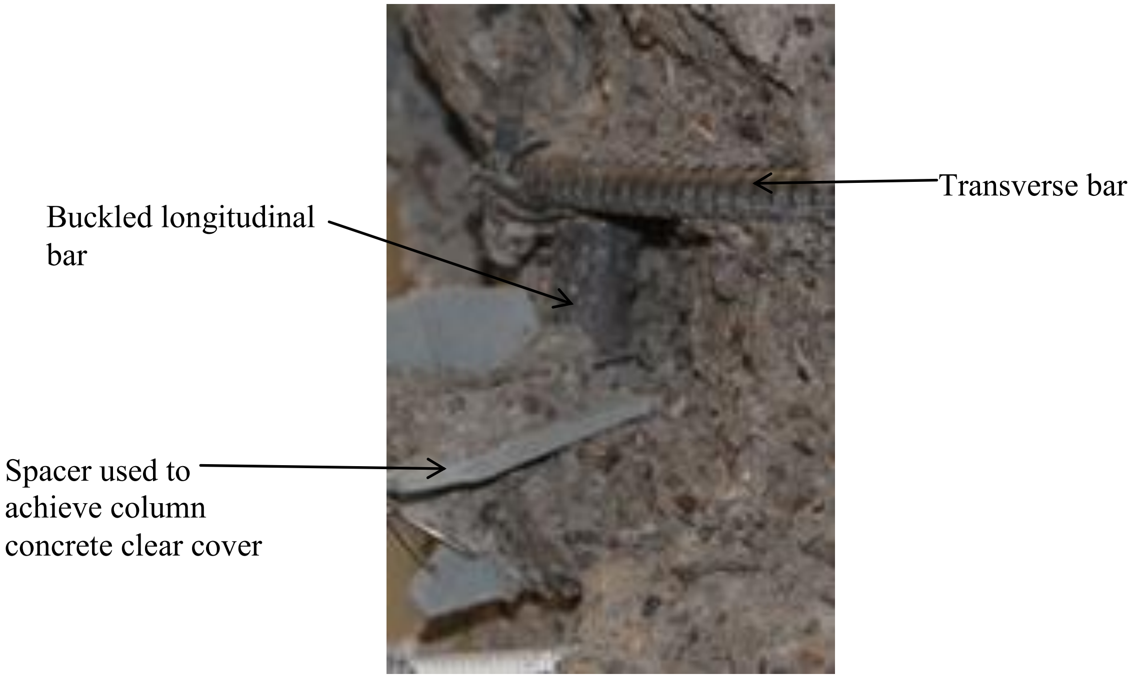

Figure 5.13 Photograph of column C2 first bar buckling

5.3.4 Bar Fracture

The first longitudinal reinforcing bar that fractured occurred on the return cycle after the first peak of the 8.75 inch (0.222 m) displacement cycle. The applied load was 10.94 kips (48.66 kN) and the tip displacement was 1.21 inches (0.0.31 m). The reinforcing bar fractured after it formed a microcrack as a result of bar buckling. The microcrack is believed to occur during compression and the failure is believed to have occurred on the following tension load. Figure 5.14 shows that the southernmost longitudinal reinforcing bar fractured at an elevation approximately 8.5 inches (0.216 m) above the base of the column.

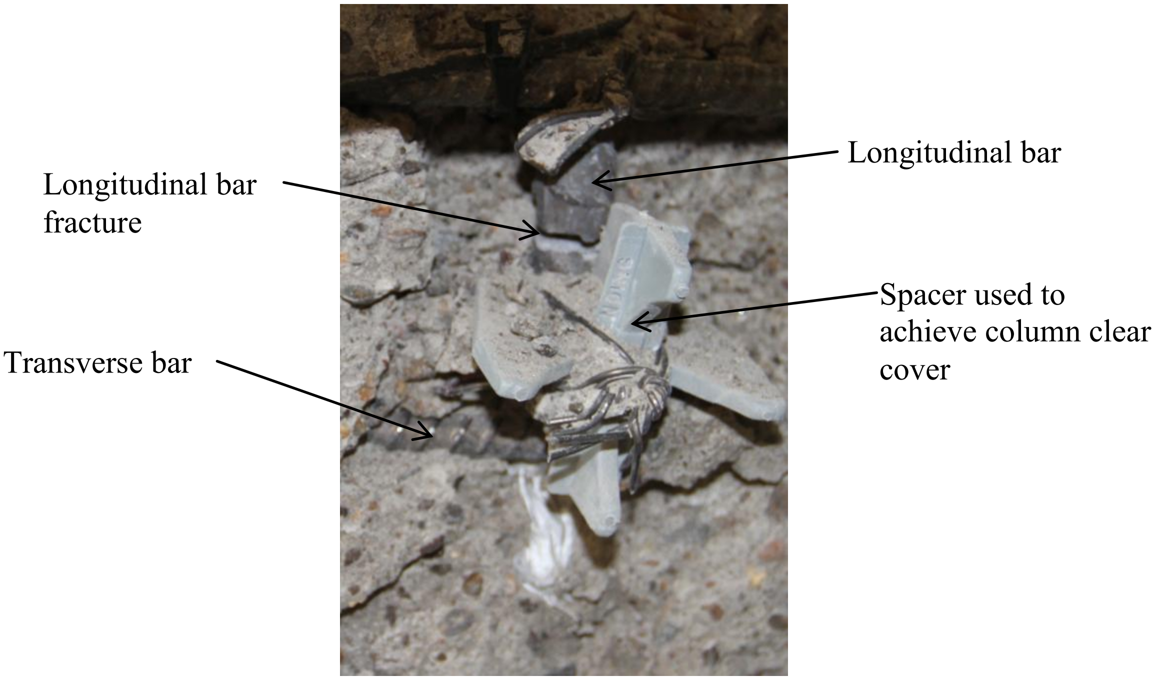

Figure 5.14 Photograph of column C2 first bar fracture

5.3.5 Column Lateral Displacement

The lateral displacement of the column was measured at six points along the height of the column. Details of the point locations were discussed earlier. Figure 5.15 shows the maximum and minimum lateral deflections at the 6 points for the 12 displacement cycles. As with the data from column C1, the elevation is normalized with respect to the column diameter, D, and the lateral displacement, Δ, is normalized by the column test height, H. Figure 5.7 shows the geometry and physical interpretation of the variables used in the column lateral displacement analysis, Δ, D, and H. Note that Δ, is taken at each of the 6 points along the height of the column.

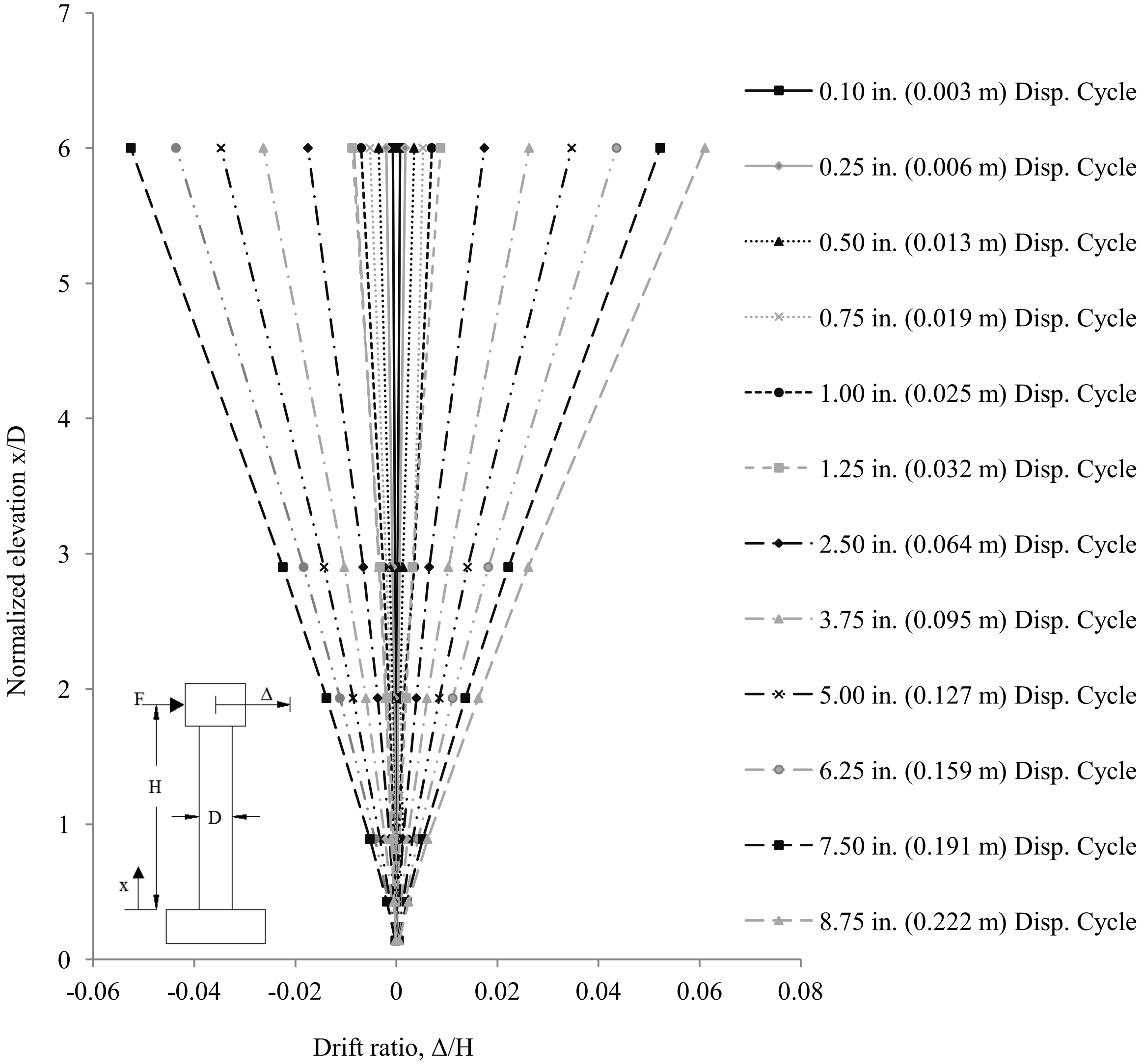

Figure 5.15 Lateral displacement of Column C2

5.3.6 Steel Reinforcing Strains

Steel reinforcing strains were recorded on both the longitudinal and transverse reinforcement. Locations of the strain gages for column C2 were provided in Chapter 3. Figure 5.16 shows the maximum transverse steel reinforcement strains for column C2 for each displacement cycle along the height of the column. The elevation is normalized by the column diameter, D, and the steel strain is normalized by the yield strain of the transverse reinforcement. The yield strain is defined as the yield stress determined using by the 0.2% offset method divided by the nominal modulus of elasticity, 29,000 ksi (200 GPa). Note that the spiral within the footing never went into tension during the final displacement cycle; the value shown in the figure is the minimum compression value.

Figure 5.17 shows the maximum longitudinal steel reinforcement strains of column C2 for each positive and negative displacement cycle along the height of the column. The maximum positive displacement cycle corresponds to the maximum tension strain. The maximum negative displacement cycle corresponds to the maximum compressive strain. The elevation is also normalized by the column diameter, D, and the steel strain is normalized by the yield strain of the longitudinal reinforcement. The yield strain was computed in the same manner as the transverse yield strain. Table 5-4 shows the yield strain values used to determine the yield strain values. Note that the transverse and longitudinal strains are stacked in terms of the displacement cycle, i.e., the lowest bar strains at each elevation represents 0.10 inch (0.003 m) displacement cycle and the highest bar represents the 8.75 inch (0.222 m).

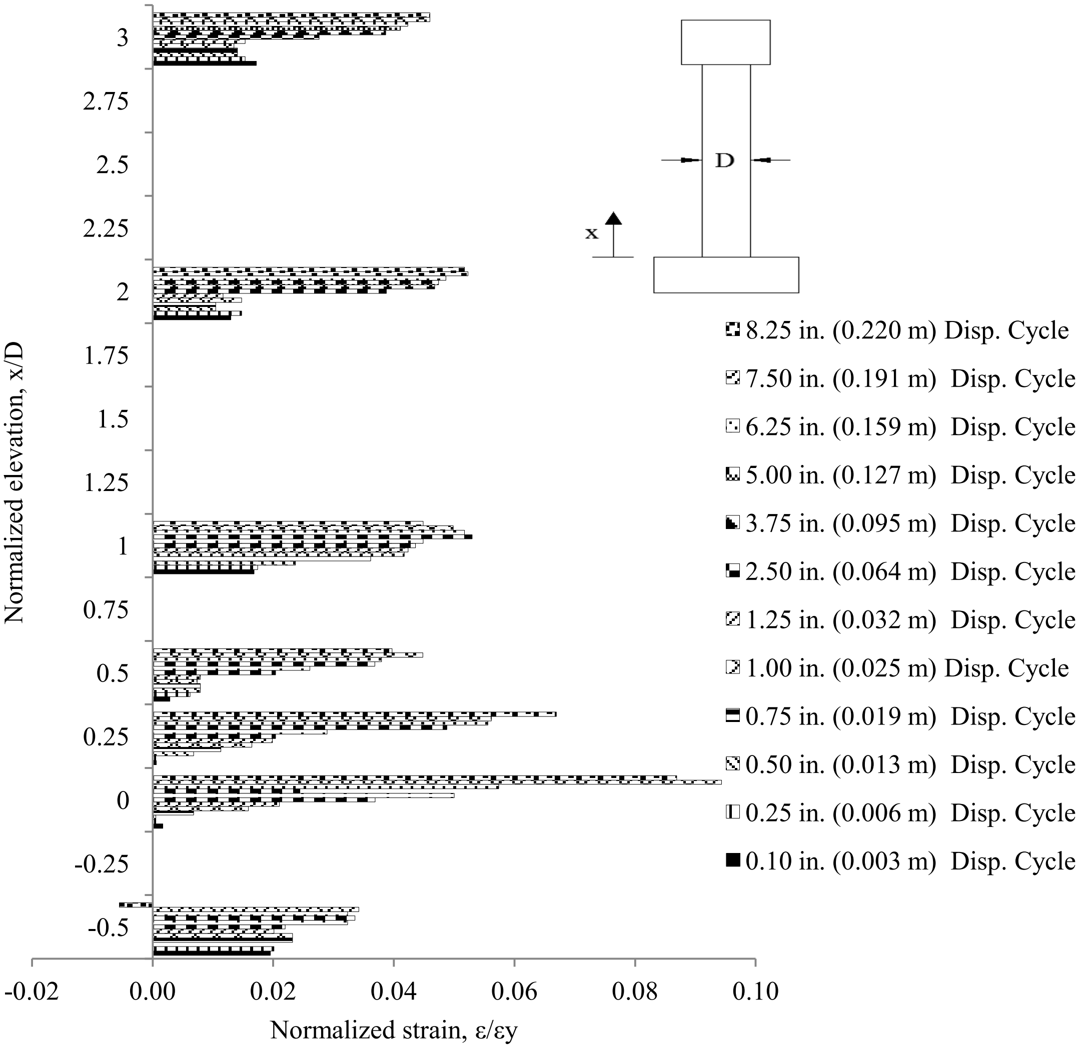

Figure 5.16 Transverse strains in Column C2

Table 5-4 Column C2 yield strains used in the strain analysis

Reinforcement	Yield strain	Yield stress ksi (MPa)	MOE ksi (GPa)
#3 (#10M) Grade 80 ksi (550 MPa)	0.00288	83.4 (575)	29,000 (200)
#5 (#16M) Grade 80 ksi (550 MPa)	0.00297	86.2 (594)	29,000 (200)

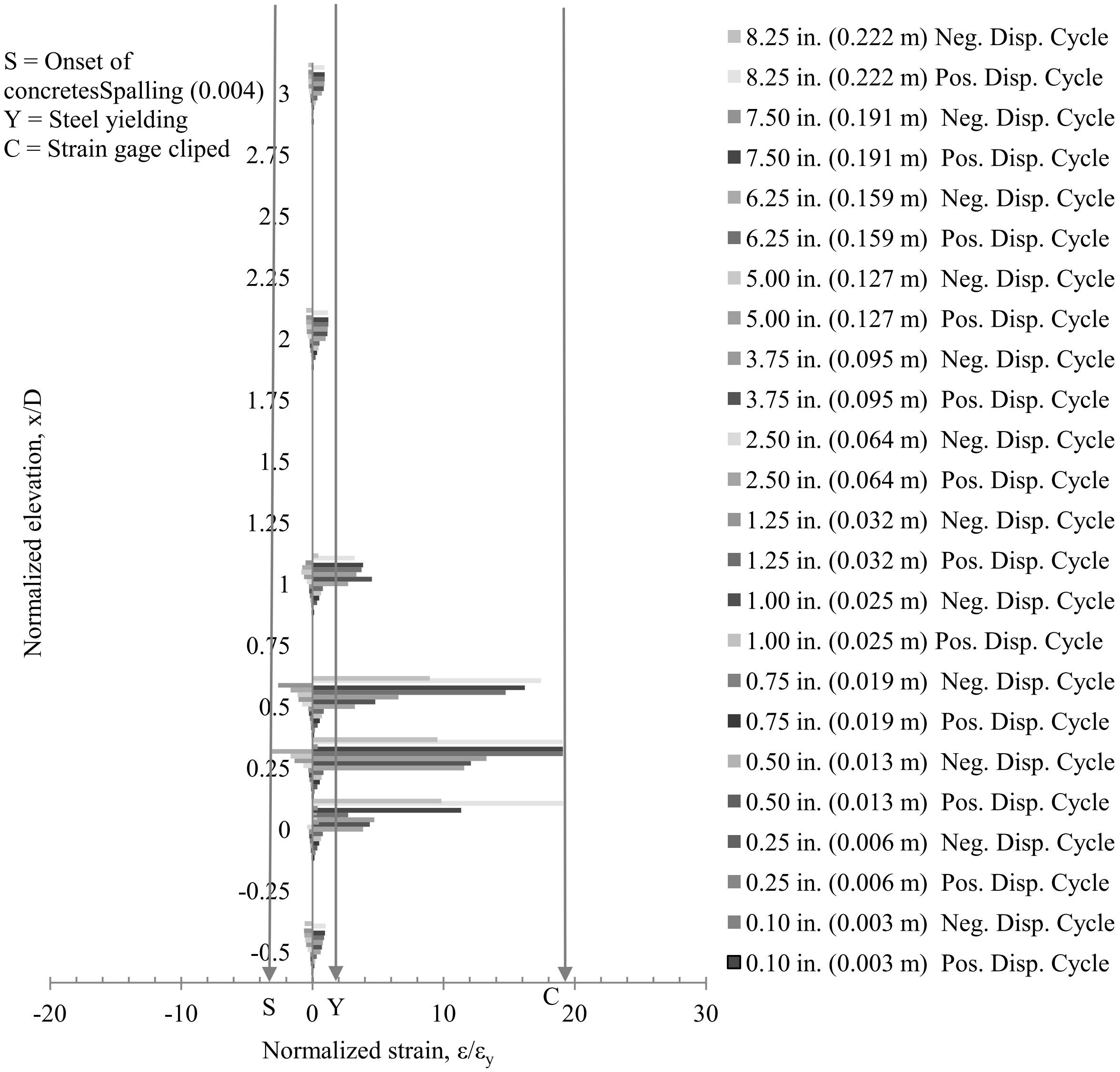

Figure 5.17 Longitudinal strains for Column C2

5.3.7 Column Curvature

The relative curvature was computed at each of the five instrumentation levels for each displacement level. Figure 5.18 shows the relative curvature for each displacement cycle along the height of the column. The elevation and curvature are both normalized by the column diameter, D. The elevation is divided by the column diameter, D, and the curvature is multiplied by the column diameter, D. Figure 5.7 shows the physical representation of the variables used in the curvature computations. Calculations used to determine the relative curvature at each level, i, are the same as for column C1 shown in section 5.2.7.

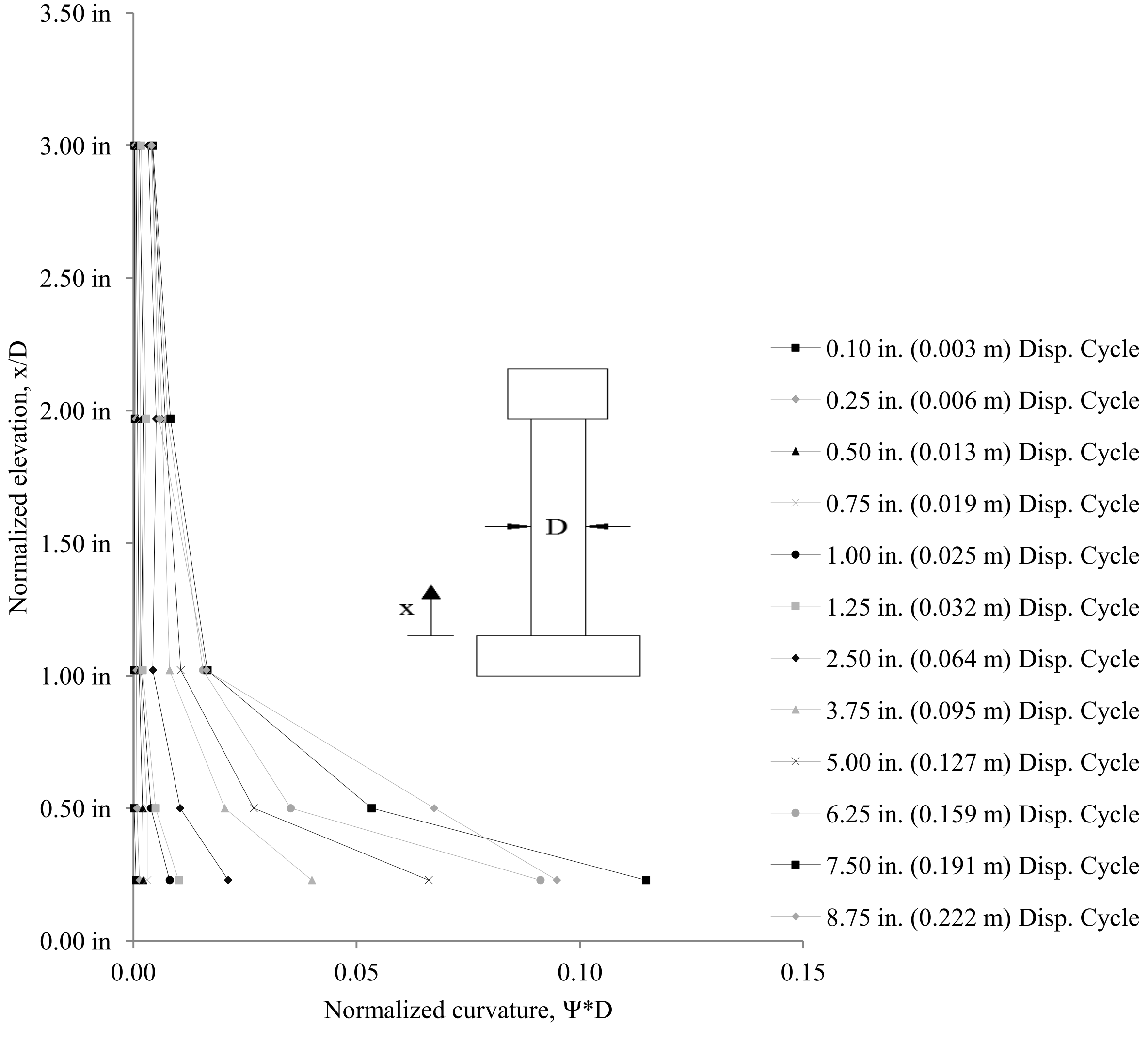

Figure 5.18 Column C2 normalized curvature with respect to the column diameter, D

5.3.8 Column Tilt

The column tilt was measured using a tilt sensor mounted at the center of east face of the header. Figure 5.19 shows a plot of the measured tilt and the calculated tilt versus the applied force. The calculated tilt was computed as the tip displacement divided by the column height converted into degrees. As seen in the plot there is an increasing difference between the measured tilt and the calculated tilt as the applied force reaches its maximum and minimum values. As with column C1, this is likely due to the positioning of the string pot that measures the tip displacement. As the column is being pushed horizontally the column also bends creating an additional vertical component measured by the string pot.

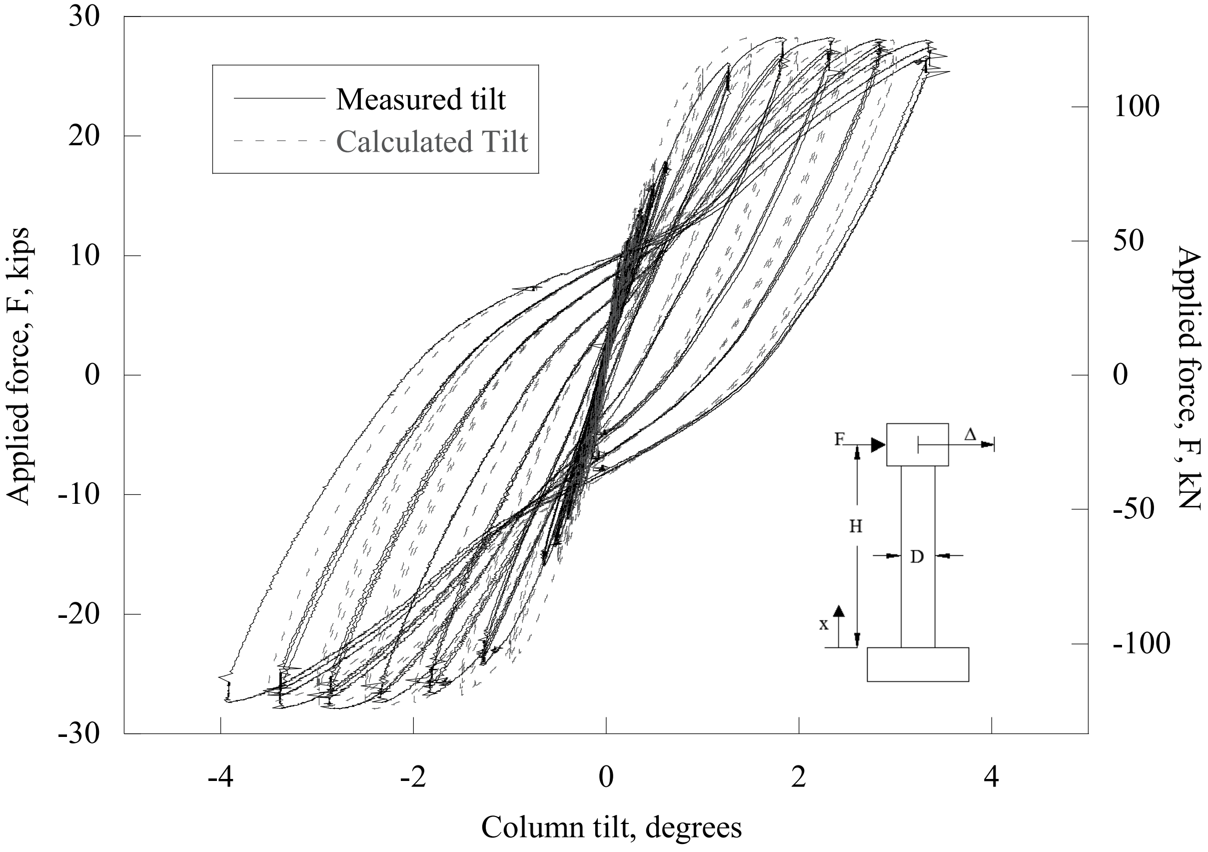

Figure 5.19 Column C2 tilt versus applied force

5.3.9 Horizontal Load

The applied horizontal load is measured by a group of parallel load cells within the actuator. The applied load was plotted against the drift ratio as shown in Figure 5.20. The maximum applied force was 28.24 kips (125.6 kN) and the maximum drift ratio was 0.061.

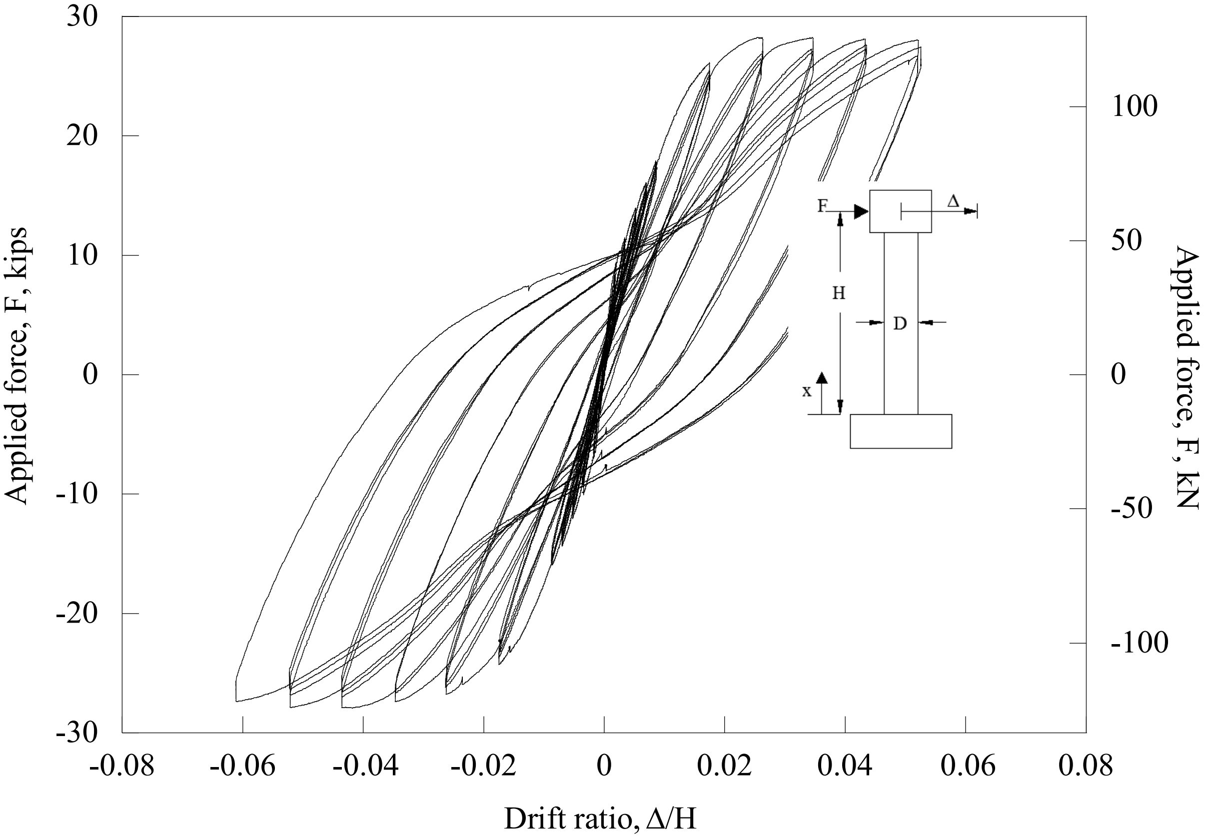

Figure 5.20 Column C2 applied force vs. drift ratio

5.3.10 Vertical Load

The applied axial (vertical) load was applied in the same manner as described for column C1. The initial axial load was set to 90 kips (400 kN). The same procedure described for column C1 was used for column C2 to attempt to minimize the change in axial load during testing. As shown in

Figure 5.21 the axial load increased as the applied horizontal load increased for column C2. The axial load for column C2 also dropped below the initial 90 kips (400 kN). The figure exhibits a similar shape as the figure for column C1, indicating that load histories were similar. The small differences in shape and the maximum axial load between columns C1 and C2 may be due to a slight difference in the pneumatic nitrogen accumulator pre charge.

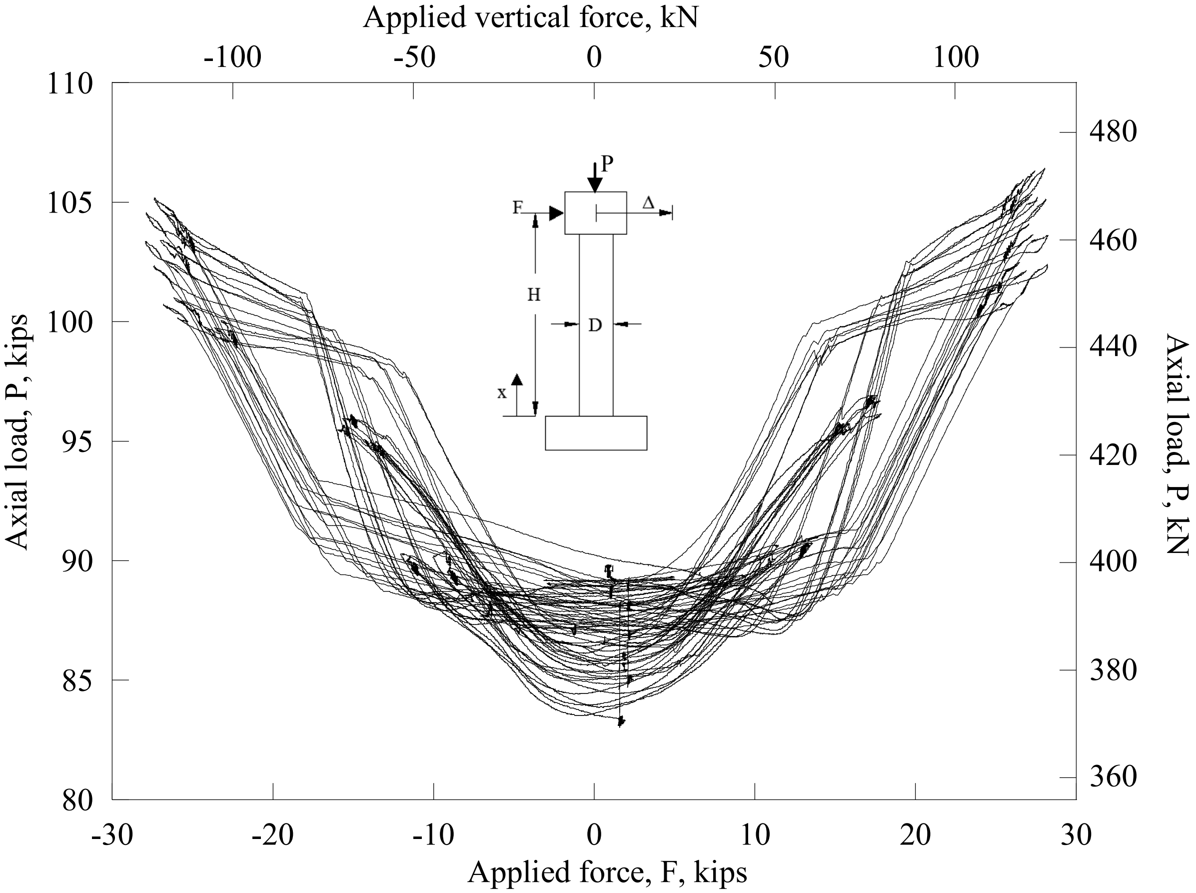

Figure 5.21 Column C2 axial load vs. applied force

5.3.11 Footing Displacement

The footing was instrumented with four vertical LVDTs at each corner of the top face of the footing and two LVDTs on the north face of the footing as discussed in Chapter 3 to determine if the footing rotated or displaced during the testing. The data from the six LVDTs showed that there was neither significant rotation nor horizontal displacement of the footing. No LVDT reading ever exceeded 0.05 inch (0.0013 m).

5.4 Summary

This chapter presented both visual and measured observations for two columns: column C1 and column C2. The visual observations included cracking, concrete spalling, bar buckling and bar fracture. The measured observations included column lateral displacement, steel reinforcement strains, column curvature, column tilt, horizontal applied load, vertical applied load and footing displacement. The goal of this section was to evaluate the performance of the two columns under cyclic lateral loading. The next chapter, Chapter 6, contains the analysis of the data presented in this chapter.

Chapter 6

ANALYSIS OF EXPERIMENTAL DATA

6.1 Introduction

Analyses were conducted using experimental data collected. For the analyses in this report, only data collected until the first bar fracture is included. The bar fracture is assumed to be the point of column failure. The effect of steel reinforcement grade was evaluated based on the visual observations, column lateral displacement, column steel strains, column curvature, horizontal applied load, energy dissipation, and column ductility.

6.2 Effect of Steel Reinforcement Grade

Columns C1 and C2 have the same exterior dimensions and similar moment capacities. Column C1 is reinforced with Grade 60 and column C2 is reinforced with Grade 80.

6.2.1 Visual Observations

Columns C1 and C2 exhibited similar crack distributions. However, the cracks in column C2 seem to appear over a larger height than column C1. This difference is approximately 2 feet (0.610 m). It is not clear whether this is a result of the reinforcement grade or a result of fewer longitudinal reinforcing bars. Columns C1 and C2 exhibited the onset of concrete spalling and concrete delamination during the same displacement cycles. Deep concrete spalling for column C2 occurred 2 displacement cycles later than column C1. Deep concrete spalling occurred for column C2 on the 8.75-inch (0.222 m) displacement cycle and at the 6.25-inch (0.159 m) displacement cycle for column C1. The location of the longitudinal reinforcing bar that buckled and ruptured was the same for both columns—this bar was the bar furthest to the south (closest to the strong wall). Thus, the mode of failure of the columns was flexural modes with bar buckling followed by tension fracture. The first longitudinal reinforcing bar to buckle and fracture in column C2 occurred at approximately 2.5 inches (0.064 m) further from the base of the column when compared with column C1. The bar fractured in column C1 was approximately 6 inches (0.152 m) from the base of the column at the final peak of the 7.50-inch (0.191 m) displacement cycle. The column C2 bar fractured approximately 8.5 inches away from the base of the column on the return from the first peak of the 8.75-inch (0.222 m) displacement cycle. The first longitudinal reinforcing bar in column C2 ruptured one displacement cycle later than column C1. Columns C1 and C2 both exhibited initial bar buckling in the direction of the applied load.

From the visual observations results of columns C1 and C2, column C2 seems to have improved performance. This is because the reinforcing bar fracture was observed at a larger displacement when compared to column C1. This indicates that Grade 80 reinforcement meeting ASTM A706 specifications may be an alternative reinforcement for Grade 60 reinforcing steel. It should be noted that because the bar fracture in column C2 occurred at a higher elevation than the bar fracture in column C1, the plastic hinge zone may need to be extended and/or additional development length provided. Further research is needed to assess this. However, longitudinal bar buckling and fracture higher in the column may be an advantage for post-earthquake inspections.

6.2.2 Maximum Lateral Displacement

Displacements at the level of the applied horizontal force were recorded for all tests. Column C2 exhibited larger displacements before the first bar fracture than column C1. Column C2 exhibited a maximum displacement of 8.79 in (0.223 m) and column C1exhibited a maximum displacement of 7.53 in (0.191 m). Figure 6.1 shows the drift ratio vs. elevation for the 7.5 inch (0.191 m) and 8.75 inch (0.222 m) displacement cycles for columns C1 and C2. The maximum drift ratio of column C1 was 5.23% and 6.11% for column C2.

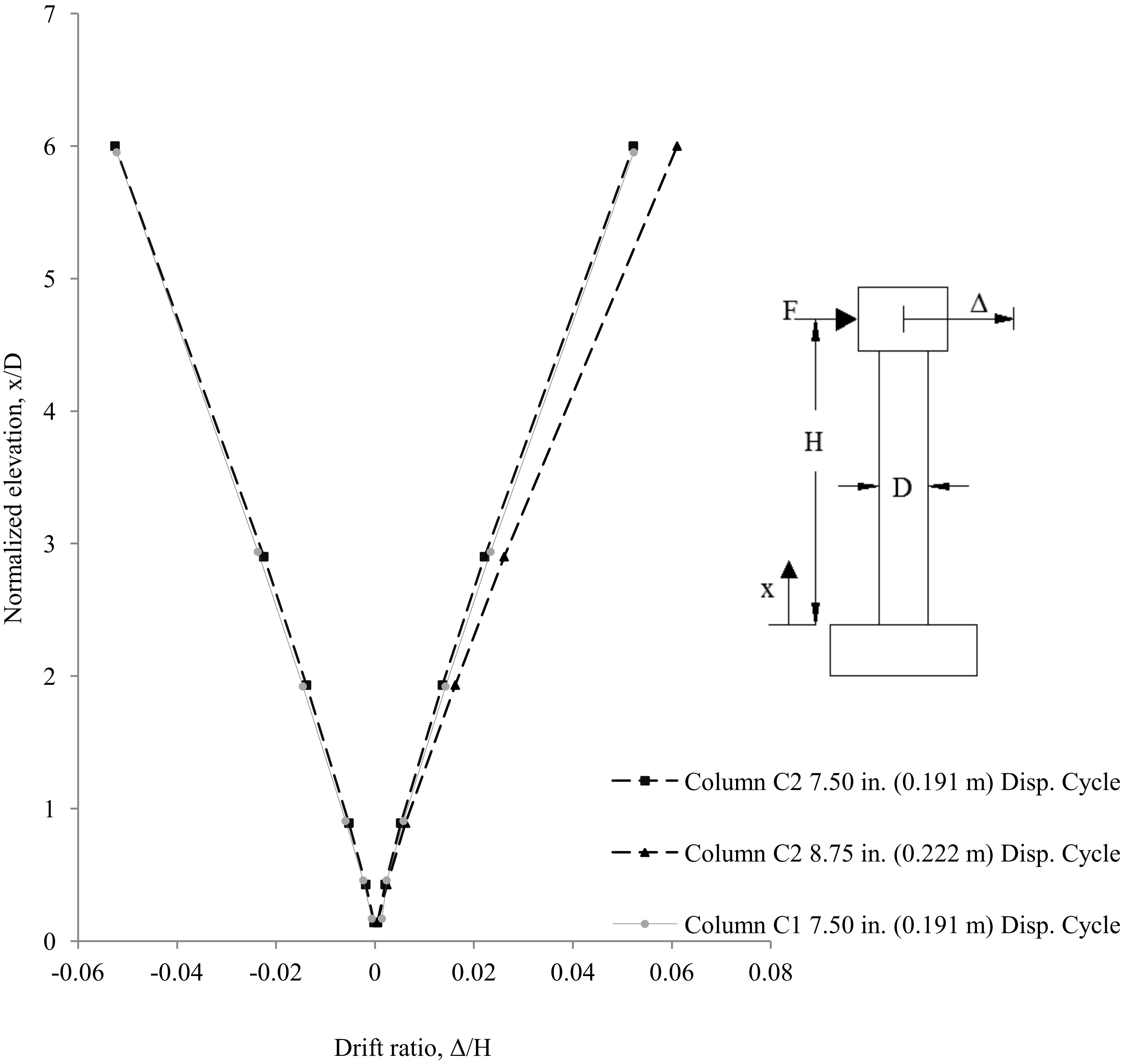

Figure 6.1 Columns C1 and C2 lateral displacements

As seen in Figure 6.1 the drift ratios along the normalized elevation of the column are very similar for the 7.50 inch (0.191 m) displacement cycle for columns C1 and C2. It is also seen that column C2 did not fail until the 8.75 inch (0.222 m) displacement cycle.

6.2.3 Steel Strains

Columns C1 and C2 had strain gages attached at similar locations to compare the strains in the steel reinforcement. Figure 3.10 shows the locations of the strain gages and the levels at which these were installed. The longitudinal reinforcing bars in column C1 yielded first at a tip displacement of 1.17 inches (0.030 m). This occurred during the approach to the first peak of the 1.25 inch (0.032 m) displacement cycle at the base of the column, level 2 where the strain is largest. The bar also yielded at levels 3 and 4 during this displacement cycle. The longitudinal bars in column C2 first yielded at a tip displacement of 1.52 inches (0.039 m). This occurred during the approach to the first peak of the 2.50 inch (0.064 m) displacement cycle at instrumentation level 3.The base of the column, level 2 through level 5 also yielded later in this same displacement cycle. Note that the longitudinal reinforcing bar in column C2 first yielded 6 inches (0.152 m) above the base of the column while the longitudinal reinforcing bar in column C1 first yielded at the base of the column. This may indicate that additional details are required to develop the Grade 80 reinforcing bars at the base of the column. Further research is needed. The longitudinal steel in column C1 yielded in the footing (level 1) on the 3.75 inch (0.095 m) displacement cycle and the longitudinal steel in column C2 did not yield in the footing (level 1) until the 8.75 inch (0.222 m) displacement cycle. This indicates that the contribution of strain penetration is not as important for column C2 as compared to column C1. Table 6-1 shows the transverse strains for columns C1 and C2 for 3 displacement cycles. All the transverse strains were very small in magnitude and never approached yielding; however it can be seen in Table 6-1 that the transverse strains in column C2 were typically larger than those of column C1. This may be due to the larger spacing between the longitudinal reinforcing bars embedded in column C2 compared to column C1. Note that column C1 does not have transverse strains for level 1 because the lead wires were damaged during fabrication of the footing.

Table 6-1 Summary of maximum transverse steel strains of columns C1 and C2

Level	Elevation in. (m)	2.50 in. (0.064 m) displacement cycle		5.00 in. (0.013 m) displacement cycle		7.50 in. (0.019 m) displacement cycle	
		C1 max % strain	C2 max % strain	C1 max % strain	C2 max % strain	C1 max % strain	C2 max % strain
1	-12.00 (-0.305)	N.A.*	0.0063	N.A.*	0.0097	N.A.*	0.0098
2	0.00 (0.000)	0.0067	0.0106	0.0093	0.0070	0.0172	0.0271
3	6.00 (0.152)	0.0020	0.0059	0.0031	0.0140	0.0136	0.0162
4	12.00 (0.3050	0.0066	0.0059	0.0133	0.0106	0.0329	0.0129
5	24.00 (0.610)	0.0078	0.0125	0.0120	0.0152	0.0145	0.0143
6	48.00 (1.219)	0.0062	0.0112	0.0070	0.0136	0.0067	0.0150
7	72.00 (1.829)	0.0069	0.0079	0.0083	0.0118	0.0097	0.0132

* N.A. Not available because lead wires were damaged during the footing concrete placement.

Table 6-2 shows the longitudinal strains for columns C1 and C2 for 3 displacement cycles. These data indicate that at the lower displacement cycles column C2 has larger longitudinal strains while at larger displacement cycles column C1 typically has larger longitudinal strains. For all displacement cycles, column C1 had larger longitudinal strains at the base of the column (level 2) when compared to column C2. This may suggest that column C2 reinforced (containing Grade 80 reinforcement) may require additional detailing to ensure the bar is fully developed at the base of the column, as already noted. Other than at the base of the footing (level 2) there does not seem to be any significant differences between the strains in the longitudinal reinforcing bars between column C1 reinforced with Grade 60 and column C2 reinforced with Grade 80. Column C1 had much larger compression strains in the longitudinal reinforcement when compared with column C2. The data indicates that the columns exhibited similar performance and reinforcement strains.

Table 6-2 Summary of maximum longitudinal steel strains of columns C1 and C2

Level	Elevation in. (m)	2.50 in. (0.064 m) displacement cycle		5.00 in. (0.013 m) displacement cycle		7.50 in. (0.019 m) displacement cycle	
		C1 max % strain	C2 max % strain	C1 max % strain	C2 max % strain	C1 max % strain	C2 max % strain
1	-12.00 (-0.305)	0.12	0.19	0.29	0.24	0.35	0.29
2	0.00 (0.000)	1.57	1.15	4.07	1.40	4.29	3.37
3	6.00 (0.152)	1.33	3.44	3.93	3.94	5.72*	5.67*
4	12.00 (0.3050	0.30	0.96	3.80	1.95	4.79	4.81
5	24.00 (0.610)	0.34	0.81	1.38	1.00	1.72	1.15
6	48.00 (1.219)	0.27	0.30	0.30	0.35	0.31	0.36
7	72.00 (1.829)	0.17	0.21	0.20	0.27	0.20	0.28

*Note that values over 5% strain are out of the dynamic range of the strain gages and may not be accurate.

6.2.4 Column Curvature

The normalized relative curvature data were shown in Chapter 5.The relative curvature was normalized by multiplying the value but the diameter, D, of the column. The largest relative curvatures occurred closest to the base of the column and reduced in magnitude along the height of the column. Note that column C2 was tested at the 8.75 inch (0.222m) displacement cycle but the relative curvature values at the 7.50 inch (0.019 m) displacement cycle were larger at all levels except for level 2 compared to the relative curvature values at the 8.75 inch (0.222) displacement cycle. Table 6-3 shows the relative curvature for 3 of the larger displacement cycles for columns C1 and C2. It can be seen that the relative curvatures at instrumentation levels other than level 1 are very similar between the two columns. However, at level 1, for all displacement cycles, column C1 exhibited larger values of relative curvature when compared to column C2. These results indicate that Grade 80 and Grade 60 reinforced columns have similar curvatures resulting from flexural deformations (i.e., from levels 2 through 5). The relative curvature at level 1 is composed of flexural deformations, deformations of the bars passing through the joint core, and global slippage of the bars. It is not possible to state exactly which of the three contributions is making the relative curvature values at the lower level for column C1 larger than those of column C2. It is believed that it is not largely depended on the flexural deformations as indicated with the longitudinal strain data. These results suggest that Grade 80 reinforcement can be used and can achieve similar performance as columns containing Grade 60 reinforcement.

Table 6-3 Summary of column C1 and C2 relative curvature

Level	Elevation* in. (m)	2.50 in. (0.064 m) displacement cycle		5.00 in. (0.013 m) displacement cycle		7.50 in. (0.019 m) displacement cycle	
		C1 max normalized curvature	C2 max normalized curvature	C1 max normalized curvature	C1 max normalized curvature	C1 max normalized curvature	C2 max normalized curvature
1	6.00 (0.152)	0.031	0.021	0.085	0.066	0.119	0.115
2	12.00 (0.3050	0.008	0.010	0.029	0.027	0.050	0.053
3	24.00 (0.610)	0.005	0.004	0.010	0.011	0.021	0.017
4	48.00 (1.219)	0.004	0.005	0.005	0.007	0.005	0.008
5	72.00 (1.829)	0.003	0.003	0.004	0.004	0.004	0.004

*Note these elevations are not exact; the exact elevations are slightly different for the two columns and are accounted for in the analysis.

6.2.5 Applied Horizontal Load

The applied horizontal load was measured using a load cell in the actuator and the tip displacement was measured using a string pot. The moment capacity was computed as follows:

(1) Compute the drift angle, θ;

$$\theta=\frac{\Delta}{H}$$

(2) Compute the horizontal component of the axial load, P_H;

$$P_H=P\sin(\theta)$$

(3) Compute the moment capacity of the column, M;

$$M=(F-P_H)L$$

These calculations remove the horizontal component of the applied axial load that is acting against the applied horizontal load. The percent difference between the actual moment capacities of columns C1 and C2 is 10.30%. The expected moment capacities were computed using Response 2000® and assuming elastic perfectly-plastic steel stress strain models. Although the prediction was relatively good, other considerations may be needed to predict the moment capacity of a concrete column reinforced with Grade 80.

Table 6-4 shows the maximum applied force and moment capacity for both columns. As shown in the table, the maximum applied forces of the two columns are very similar. However the moment capacity of column C2 is 11% larger than the moment capacity of column C1. Column C1 had a larger horizontal displacement and axial load at the maximum horizontal applied force. Results also indicated that the expected moment capacity is larger than the actual moment capacity. The over strength factor of 1.4 used to predict columns C1 and C2 moment capacity appears to be high. It should be noted that the moment capacity of column C1 is only 93% of its calculated nominal moment capacity and the moment capacity of column C2 is 3% larger than its calculated nominal moment capacity. The percent difference between the expected moment capacities of columns C1 and C2 is 1%. The percent difference between the actual moment capacities of columns C1 and C2 is 10.30%. The expected moment capacities were computed using Response 2000® and assuming elastic perfectly-plastic steel stress strain models. Although the prediction was relatively good, other considerations may be needed to predict the moment capacity of a concrete column reinforced with Grade 80.

Table 6-4 Column C1 & C2 moment capacity

Column	Maximum applied force kip (kN)	Expected shear capacity kip (kN)	Moment capacity kip-ft (kN-m)	Expected moment capacity kip-ft (kN-m)
C1	28.86 (128.4)	33.58 (149.4)	267 (362)	403 (546)
C2	28.24 (125.6)	33.22 (147.8)	296 (401)	399 (541)

Figure 6.2 shows the applied horizontal force versus the drift ratio for columns C1 and C2 up to the first longitudinal bar fracture. It can be seen that the overall shape of the hysteretic loops are similar. Note that column C1 has more area between the loading and unloading curves, which indicates greater energy dissipation. This is discussed in more detail in section 6.2.7.

6.2.6 Energy Dissipation

The energy dissipated per cycle was determined for each column. The value was determined by taking the area within the applied force vs. displacement hysteretic loops for each displacement cycle. This value was then divided by the number of cycles per displacement cycles. It is worth noting that for each displacement cycle there was 3 cycles each having a north and south displacement peak equal to the value of the given displacement cycle. Also, note that for the final displacement cycle, less than 3 complete cycles occurred before failure.

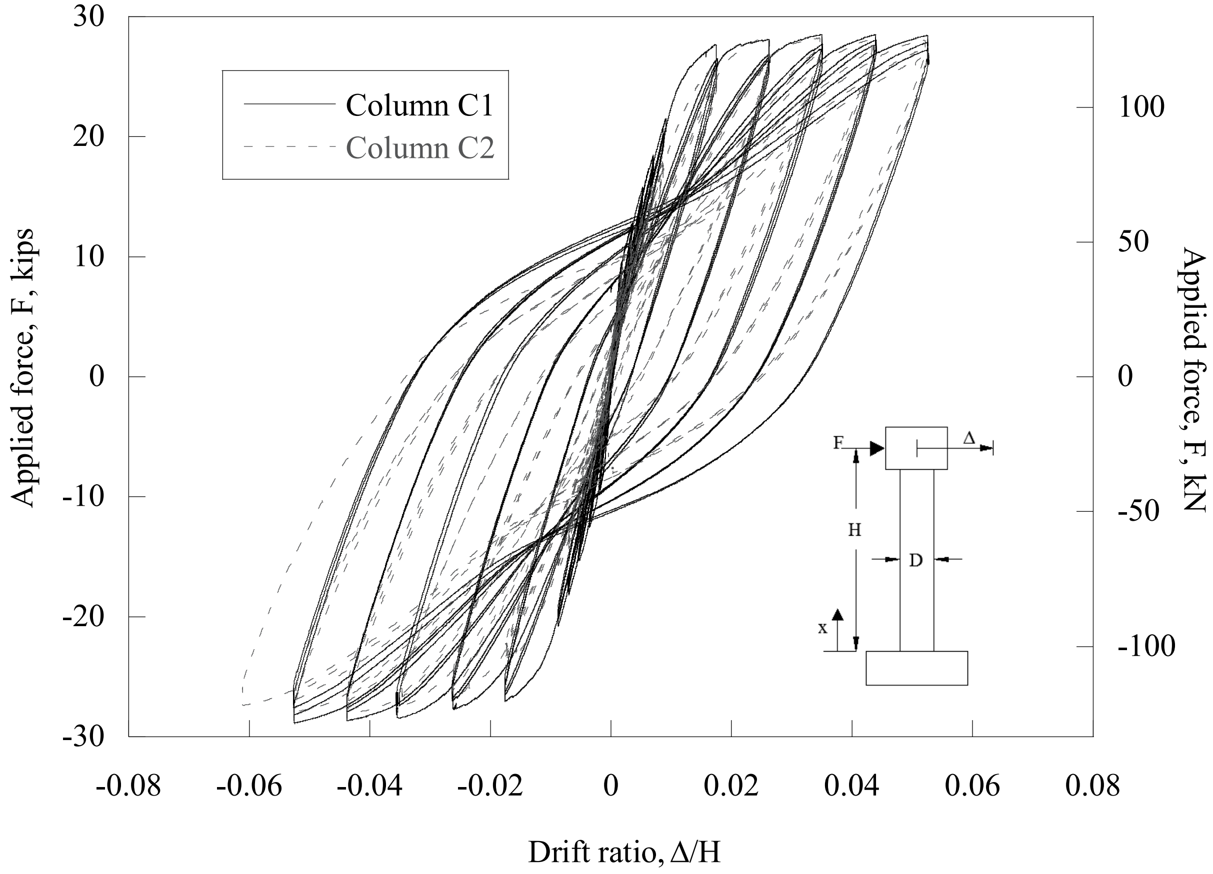

Figure 6.2 Columns C1 and C2 applied force versus drift ratio

As shown in Figure 6.3, column C1 exhibited greater energy dissipation per cycle until the failure cycle when compared to column C2. This was expected because column C1 had more reinforcing bars to absorb the energy and the reinforcing bars yielded at a lower stress when compared with the Grade 80 reinforcing bars in column C2. Table 6-5 shows the total energy dissipated up to the first reinforcing bar fracture. It can be seen in this table that column C1 dissipated more energy when compared to column C2. This is most likely due to the reduction in the area of steel in column C2, which results in lower column stiffness, which in turn lowers its energy dissipation capacity.

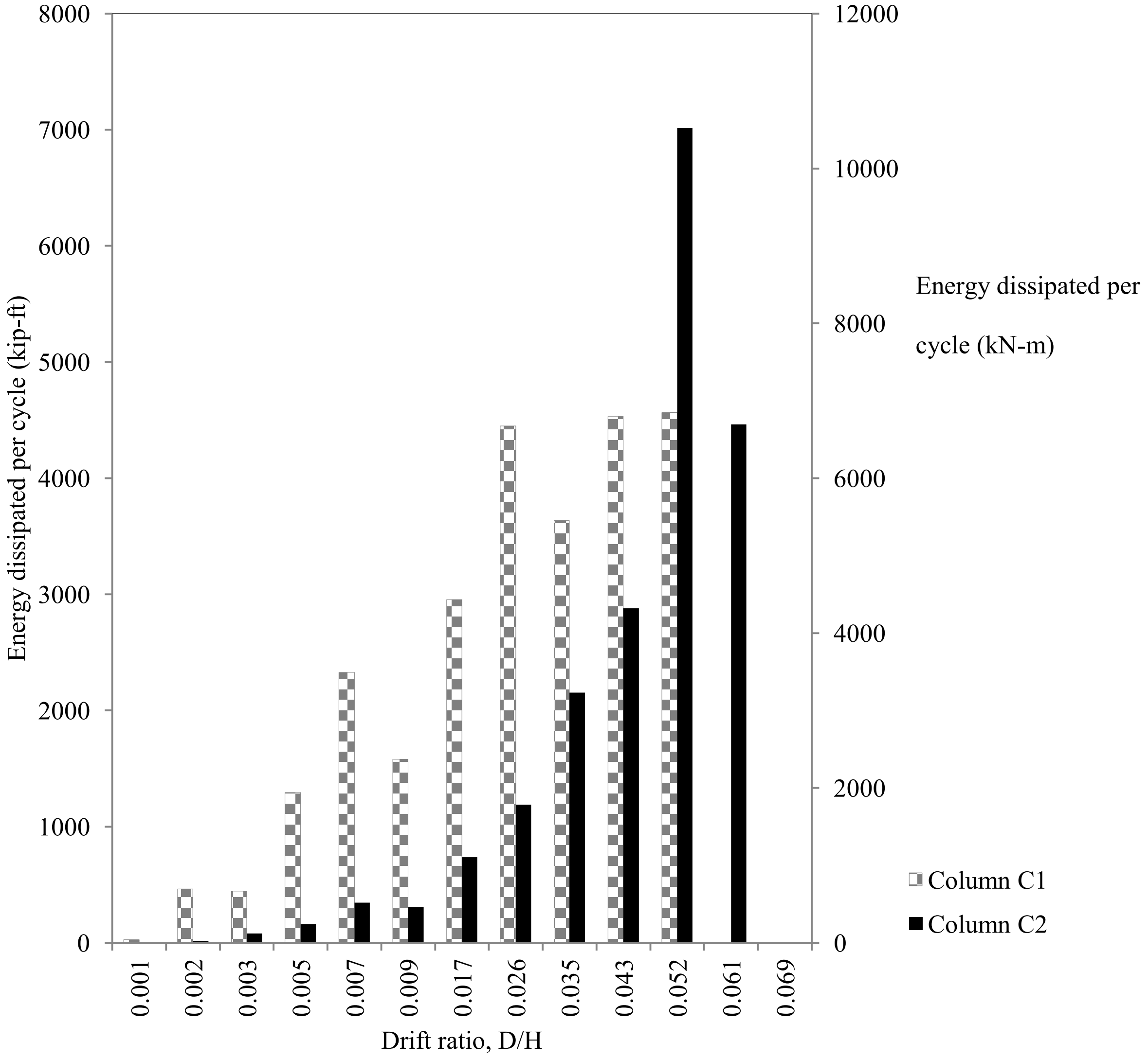

Figure 6.3 Energy dissipated per cycle for columns C1 and C2

Table 6-5 Total energy dissipated for columns C1 and C2

Column	Total energy dissipated kip-ft (kN-m)
C1	76,994 (104,390)
C2	48,040 (65,133)

Further research is needed to assess the effects of lower overall energy dissipation. It should be noted that most codes do not require a minimum energy dissipation value.

6.2.7 Column Ductility

The column ductility is defined in both displacement ductility and curvature ductility. The displacement ductility is computed as the ratio of the maximum tip displacement to the tip displacement at a reference yield of the column. Note that the reference yield of the column is defined as point when the longitudinal reinforcement bars reach a strain of 1%. It should also be noted that the displacement ductility was also computed using the first yield displacement of the column. The first yield is defined as the point when the longitudinal reinforcement first yields. The curvature ductility is computed as the ratio of the maximum relative curvature at the lowest instrumentation level (level 1) to the relative curvature at the same instrumentation level at the reference yield of the column. The curvature ductility is also computed at the other levels. The reference yield for the curvature ductility is defined in the same manner as for the displacement ductility.

Table 6-6 summarizes the displacement and curvature ductility of columns C1 and C2. The results indicate that when using the reference yield, the displacement ductility is larger for column C2 when compared to column C1. However, it should be noted that C1 has a larger displacement ductility when using the first yield displacement. This could be a result of the greater yield strength of the Grade 80 reinforcement, although stresses would be expected to be greater. Further assessment is needed. The curvature ductility of column C2 at instrumentation levels 1 and 5 are larger than those of column C1. At instrumentation level 2, both columns had similar (<5% difference) curvature ductility values. For both columns the curvature ductility was largest at this level 2.

Table 6-6 Summary of column C1 and C2 ductility

	Displacement ductility, μ_Δ		Curvature ductility, μ_ψ				
	Reference yield	First yield	Level 1	Level 2	Level 3	Level 4	Level 5
Column C1	3.94	6.44	6.32	8.87	5.75	1.60	1.42
Column C2	4.13	5.78	7.35	8.54	4.95	1.29	1.45
% Difference	4.71	10.8	15.07	3.79	14.95	21.45	2.09

The curvature ductility is typically the most important towards the base of the column where the majority of the curvature occurs. In this case the data indicates that a column reinforced with Grade 80 reinforcement performs similar to a column reinforced with Grade 60 reinforcement.

6.3 SUMMARY

Column C2 (containing Grade 80 reinforcement) performed similar to column C1 (reinforced with Grade 60 reinforcement) when comparing maximum drift ratio, relative curvature, displacement ductility, and curvature ductility. Column C2 exhibited lower energy dissipation when compared with column C1. The strain data indicates that additional anchorage/detailing may be needed to fully develop the Grade 80 reinforcement at the base of the column, although further testing is required to confirm this.

Chapter 7

SUMMARY AND CONCLUSIONS

7.1 SUMMARY

Grade 80 reinforcing bars could reduce reinforcing steel quantities, may reduce reinforcing bar congestion, and could improve the constructability and economy of RC structures. However, limited research has been performed to validate the use of Grade 8- reinforcement. Results from a limited number of research projects indicate that Grade 80 reinforcement should be considered for use in all member types. This research assessed the performance of two columns: one reinforced with Grade 60 reinforcement and the other reinforced with Grade 80 reinforcement. Although further testing will be done, this contract included testing of two columns. Four additional columns will be assessed.

Preliminary results indicate that the column constructed with Grade 80 reinforcing steel achieved similar resistance and displacement ductilities when compared with the reference column constructed with Grade 60 reinforcement. The column made with Grade 60 reinforcement showed larger hysteretic energy dissipation than the column made with Grade 80 reinforcement. Furthermore, the observed modes of failure for columns made with Grade 60 and Grade 80 reinforcement were similar. The main mode of failure was bar fracture due to longitudinal bar buckling after spalling of concrete cover in the plastic hinge region.

7.2 Future Testing

The results in this study present a promising step towards implementation of Grade 80 reinforcement in the design and construction of reinforced concrete columns, within the bounds of the variables used in the testing program. Four additional columns are to be tested and results from these tests will be reported in a report to ODOT. All results will be assessed and recommendation on the use of HSS (Grade 80) reinforcement will be provided after this testing is completed. It should be noted that the design procedure for the use of Grade 80 reinforcement in other areas of a bridge are not clear and additional research is needed. A PacTrans 2 research project has been funded to investigate the mechanical properties of Grade 80 reinforcement and to assess the shear capacity of members made with Grade 80 reinforcement. These results should provide additional information such that the codes can specifically address the use of Grade 80 reinforcement in RC members in seismic regions.

Chapter 8 **REFERENCES**

AASHTO. 2012. *AASHTO LRFD BRIDGE DESIGN SPECIFICATIONS, Customary U.S. Units, 2012*. American Association of State Highway and Transportation Officials.

American Society for Testing and Materials. 2012. "ASTM A706". American Society for Testing and Materials.

Bauschinger, J. 1887. "Variations in the Elastic Limit of Iron and Steel." *The Journal of the Iron and Steel Institute* 12 (1): 442–444.

Bentz, E.C. 2000. "Sectional Analysis of Reinforced Concrete". Ph.D. Thesis, Department of Civil Engineering, University of Toronto.

CALTRANS. 2012. *CALTRANS SEISMIC DESIGN CRITERIA*. Version 1.6. CALTRANS.

Collins, M.P., and D Mitchell. 1991. *Prestressed Concrete Structures*. Prentice-Hall.

Dodd, L., and J. Restrepo-Posada. 1995. "Model for Predicting Cyclic Behavior of Reinforcing Steel." *Journal of Structural Engineering* 121 (3): 433–445. doi:10.1061/(ASCE)0733-9445(1995)121:3(433).

Gustafson, David P. 2010. "Raising the Grade." *Concrete International* 32 (04) (April 1): 59–62.

Mander, J., F. Panthaki, and A. Kasalanati. 1994. "Low-Cycle Fatigue Behavior of Reinforcing Steel." *Journal of Materials in Civil Engineering* 6 (4): 453–468. doi:10.1061/(ASCE)0899-1561(1994)6:4(453).

Nissen, Erik. 2013. "Mill Issues Related to Making High-Strength Reinforcement". Power Point presented at the ACI Hot Topic Session: High-Strength Reinforcing Bars - Balancing Design Requirements with Achievable Material Properties, October 20, Phoenix, Arizona. http://hub.concrete.org/Convention/Fall-Convention/PresentationDetail.asp?EventId=ZHOT.

ODOT. 2012. *ODOT Bridge Design and Drafting Manual*. 2004, rev. August 2012. Oregon Department of Transportation.

Paulson, Conrad. 2013. "Brief Historical Overview of Yield Strength in ACI 318". Power Point presented at the ACI Hot Topic Session: High-Strength Reinforcing Bars - Balancing Design Requirements with Achievable Material Properties, October 20, Pheonix, Arizona. http://hub.concrete.org/Convention/Fall-Convention/PresentationDetail.asp?EventId=ZHOT.

Priestley, M. J. N., and G. Benzoni. 1996. "Seismic Performance of Circular Columns with Low Longitudinal Reinforcement Ratios." *Aci Structural Journal* 93 (4) (August): 474–485.

Rautenberg, J.M., S. Pujol, and A. Lepage. 2010. "Cyclic Response of Concrete Columns Reinforced with High-Strength Steel." *9th US National and 10th Canadian Conference on Earthquake Engineering 2010, Including Papers from the 4th International Tsunami Symposium* 3 (July 25). http://nees.org/resources/679/download/2010EQConf-000996.PDF.

Rice, Pual, and David Gustafson. 1976. "Grade 80 Reinforcing Bars and ACI 318-71." *Journal Proceedings* 73 (4) (April 1): 199–206.

Rodriguez, M., J. Botero, and J. Villa. 1999. “Cyclic Stress-Strain Behavior of Reinforcing Steel Including Effect of Buckling.” *Journal of Structural Engineering* 125 (6): 605–612. doi:10.1061/(ASCE)0733-9445(1999)125:6(605).

Selzer, Jacob. 2013. “Reinforcing Bar Metallurgy - 101”. Power Point presented at the ACI Hot Topic Session: High-Strength Reinforcing Bars - Balancing Design Requirements with Achievable Material Properties, October 20, Phoenix, Arizona. http://hub.concrete.org/Convention/Fall-Convention/PresentationDetail.asp?EventId=ZHOT.

Texler, Daniel. 2001. *DT Column* (version 2.1). dtware. http://www.dtware.com.

Trejo, D., Barbosa, A. R., and Link, T. 2014. "Seismic Performance of Circular Reinforced Concrete Bridge Columns Constructed with Grade 80 Reinforcement," Final Report, SRS 500-610, Oregon Department of Transportation.

The Regents of the University of California. 1999. *OpenSees*. University of California.

Vecchio, F.J., and M.P. Collins. 1986. “The Modified Compression Field Theory for Reinforced Concrete Elements Subjected to Shear.” *ACI Journal* 83 (2) (April): 219–231.

WSDOT. 2012. *WSDOT Bridge Design Manual (LRFD)*. M 23-50.12. Washinton State Department of Transportation.

PART 2:

CONNECTION BETWEEN PRECAST CONCRETE COLUMNS AND DRILLED SHAFTS IN SEISMIC REGIONS FOR ACCELERATED BRIDGE CONSTRUCTION

Table of Contents

List of Figures

List of Tables

Acknowledgments

The work described here was funded by Pacific Northwest Transportation Consortium (PACTRANS), TransNow, the Vietnam Education Foundation (VEF), and by the Federal Highway Administration through the Highways for Life Program (Viet Tran et al., 2013). The Pactrans funding supported the testing of the third specimen (DS-3) and the subsequent analyses of thes data from all three specimens. That funding of all of these agencies is gratefully acknowledged.

In addition, the advice and assistance provided by Bijan Khalighi of WSDOT and Lee Marsh of the BergerABAM, Inc. Assistance with the laboratory experiments was provided by fellow graduate students Todd Janes, Olafur Haraldsson, Bo-Shiuan Wang, Po-Chien Hsio, Patricia Clayton, Hang Nguyen, Travis Thonstad, Max Stephens, Spencer Livermore and by Laboratory Manager Vince Chaijaroen. Their help and encouragement is much appreciated.

Chapter 1

INTRODUCTION

The use of cast-in-place columns in bridge construction requires long on-site construction times and large labor requirements in the field. Cast-in-place construction is particularly disruptive in situations in which the construction process exacerbates traffic congestion.

Precasting bridge elements is one solution for reducing on-site construction time, field labor requirements, and traffic delays. Although full bridges can be constructed off site and transported to the bridge site, this strategy is only viable in a few situations. In practice, precasting is usually limited to smaller elements to make fabrication and transportation easier. For about 50 years, this strategy has been widely applied to bridge girders. Extending this strategy to bridge columns can be challenging in seismically hazardous areas, because it is difficult to achieve a good connection at the base of the column.

This research develops a new type of connection between a precast concrete column and the supporting cast-in-place drilled shaft. The concept, illustrated in Fig. 1-1, has been adapted from the “wet” socket connection concept that was developed by Haraldsson et al. (2011, 2013). In this connection, the precast column is intentionally roughened where it is embedded in the cast-in-placed enlarged drilled shaft. The transition region needs to be strong enough to develop the flexural strength of column. To make the transition region as short as possible, mechanical anchors are used for column bars to reduce the development length of the longitudinal reinforcement in the transition region.

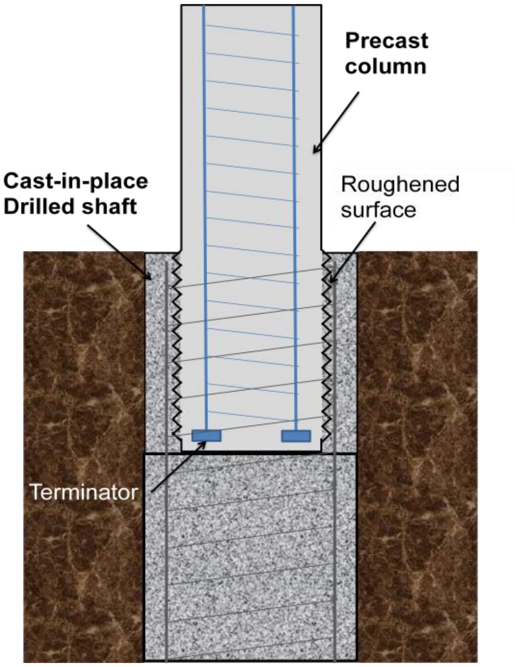

Figure 1-1. Column-to-Shaft Connection Concept

The construction sequence is shown schematically in Fig. 1-2. Once the shaft has been excavated, the shaft reinforcing cage is placed, and concrete is cast until reach the bottom level of the transition (Step 1). The precast column is then positioned and braced (Step 2), and the transition is cast (Step 3). Finally, the cap beam is constructed to connect with the columns (Step 4).

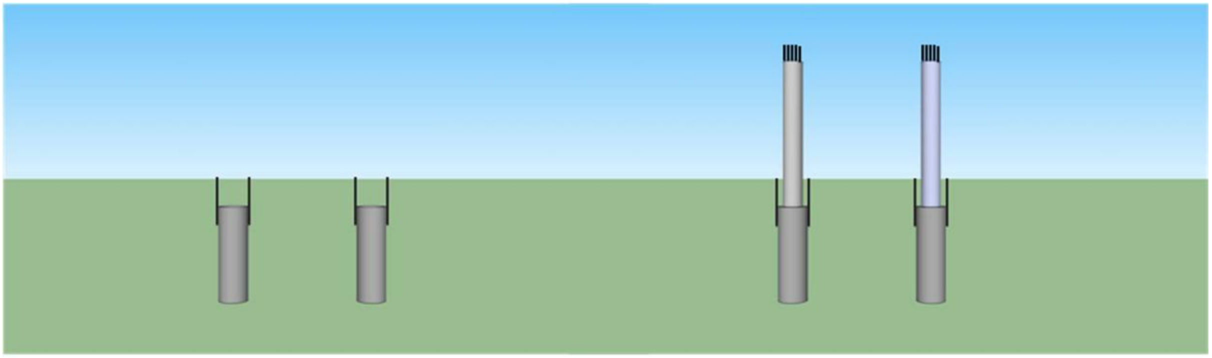

1. Dig and cast drilled shaft

2. Position and brace precast column

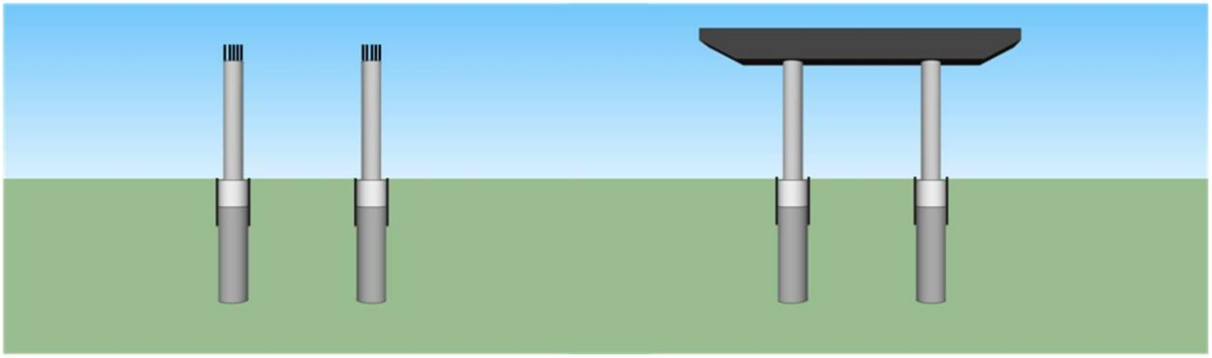

3. Cast transition

4. Position precast cross beam with ducts and grout to protruding column bars

Figure 1-2. Construction Sequence

The objective of this research was to evaluate the behavior of precast column-to-drilled shaft connections. Particular emphasis was placed on inelastic behavior under cyclic excitations which might occur during a severe earthquake, and on the proportioning of the transverse reinforcement within the transition region between the column and shaft..

Chapter 2 describes the development and design of the test specimens. Chapter 3 describes the experimental program. The system responses are reported in Chapter 4, and Chapter 5 provides a summary, conclusions, and recommendation for future research.

Chapter 2

DESIGN OF TEST SPECIMENS

Three column-drilled shaft connection specimens (DS-1, DS-2, and DS-3) were tested at the University of Washington to evaluate the seismic performance of the connection. With the exception of the spirals in the transition region, the specimens were designed to conform to the AASHTO Load Resistant Factor Design 2009, the AASHTO Guide Specifications for LRFD Seismic Design 2009, and the WSDOT Bridge Design Manual (2012).

The specimens' key properties are reported in Table 2-1. The dimensions and reinforcement in Specimen DS-1 and DS-2 were scaled (1/3.6) from a prototype. The only difference between these two specimens was the amount of spiral in the column-to-shaft transition region, which was reduced by half in DS-2. Specimen DS-3 had 60% more column reinforcement, and 45% more shaft reinforcement, but had a smaller shaft diameter.

For all specimens, the embedded length of the column in the drilled shaft (28 in.) was based on the scaled-down non-contact lap splice length of the shaft prototype according to WSDOT BDM (proposed by McLean et al. (1997)), given as:

$$l_{ns} = l_s + e$$

where:

l_{ns} = length of noncontact lap splice.

l_s = lap splice length required by AASHTO LRFD 5.11.5.3 or

$l_s = 1.7 l_d$ (for a Class C lap splice) where l_d is the longer development length of either column or shaft bars. In our case, mechanical anchors were used only for column bars, so the development length is controlled by shaft bars.

$e =$ distance between the shaft and column longitudinal reinforcement.

Table 2-1. Specimens Configuration

	DS-1	DS-2	DS-3
Column Diameter	20 in.	20 in.	20 in.
Clear Column Height	60 in.	60 in.	60 in.
Column Longitudinal Reinforcement Ratio	1.0 % (10#5)	1.0 % (10#5)	1.6 % (16#5)
Column Transverse Reinforcement	0.8 % (gage-3 @ 1.25 in. pitch)	0.8 % (gage-3 @ 1.25 in. pitch)	0.8 % (gage-3 @ 1.25 in. pitch)
Shaft Diameter	30 in.	30 in.	26 in.
Shaft Height	30 in.	30 in.	30 in.
Transition Length	28 in.	28 in.	28 in.
Shaft Longitudinal Reinforcement Ratio	0.9 % (30 bundles of 2#3)	0.9 % (30 bundles of 2#3)	2.7 % (24 bundles of 3#4)
Shaft Transverse Reinforcement	0.14 % (bundle of 2 gage-9 @ 3.0 in. pitch)	0.07 % (1 gage-9 @ 3.0 in. pitch)	0.40 % (bundle of 3 gage-9 @ 1.5 in. pitch)
Lateral Reinforcement Efficiency Factor [k]	0.50	0.25	1.00

The shaft longitudinal reinforcement was designed to form a plastic hinge in the column. Therefore, the yield moment of the shaft had to be larger than the moment at the base of the shaft due to the over-strength moment and shear from the column above.

The shaft spirals were designed based on the non-contact lap splices behavior, but using different value of efficiency factor. McLean et al. (1997) proposed a formula to determine spiral spacing as:

$$s_{tr} = \frac{2\pi A_{sp} f_{ytr} l_s}{A_l f_{ul}}$$

where,

A_{tr} = area of shaft transverse reinforcement or spiral (in.^{2})

A_l = total area of longitudinal column reinforcement (in.^{2})

f_{yt} = specified minimum yield strength of shaft transverse reinforcement (ksi)

f_{ul} = specified minimum tensile strength of column longitudinal reinforcement (ksi), 90 ksi for A615 and 80 ksi for A706

l_s = Class C tension lap splice length of the column longitudinal reinforcement (in.)

s_{tr} = spacing of shaft transverse reinforcement (in.)

TheWSDOT BDM adjusts this formula by adding to the divisor a factor, k, representing the ratio of column tensile reinforcement to total column reinforcement at the nominal resistance. This factor can be determined from column moment-curvature analysis or, as a default, taken as k = 0.5. For this research, the shaft spirals were designed with three different values of k, equal to 0.5, 0.25, and 1.0, corresponding to specimens DS-1, DS-2, and DS-3 respectively.In addition, the WSDOT BDM requires three turns of wire at the end to terminate the spiral. Thus, 6, 3, and 9 turns of spiral were placed at the top of the transition in Specimen DS-1, DS-2, and DS-3 respectively.

A typical specimen is shown in Fig. 2-1.

a). Precast Column b). Column-Shaft connection

Figure 2-1. Specimen

Chapter 3

QUASI-STATIC TESTS

The specimens were placed in a self-reacting rig, as shown in Fig. 3-1. A constant axial load of 159k was applied to the top of the column to represent the un-factored dead load. The specimen was then subjected to cyclic, horizontal displacements. The displacement history was the same as applied in previous tests by Pang et al. (2008), Haraldsson et al. (2011), and Janes et al. (2011). This displacement history was a modification of a loading history for recommended in NEHRP (Building Seismic Safety Council). The testing stopped when nearly all of the column bars or shaft spirals had fractured.

The axial load applied at the top of column was monitored by load cells in the Baldwin Testing Machine. The lateral load was monitored by load cells in the MTS actuator. The response of the specimen was monitored by potentiometers, linear variable differential transformers (LVDTs), a motion-capture system (Optotrak Certus brand), and strain gauges.

The displacement history included multiple sets of 4 cycles each. Within each set, the peak amplitudes of each cycle was 1.2A, 1.4A, 1.4A, and 0.33A respectively, where A is the maximum peak amplitude from the previous cycle set. The small amplitude cycle was intended to evaluate the residual small-displacement stiffness in the specimen after the maximum peak amplitude cycle of each set. In all cycles, the actuator moved from zero displacement to the peak cycle displacement in approximately 20 seconds. The maximum positive and negative displacements in each cycle were denoted as “peaks” and “valleys”. The displacement history is plotted in Figure 3-2.

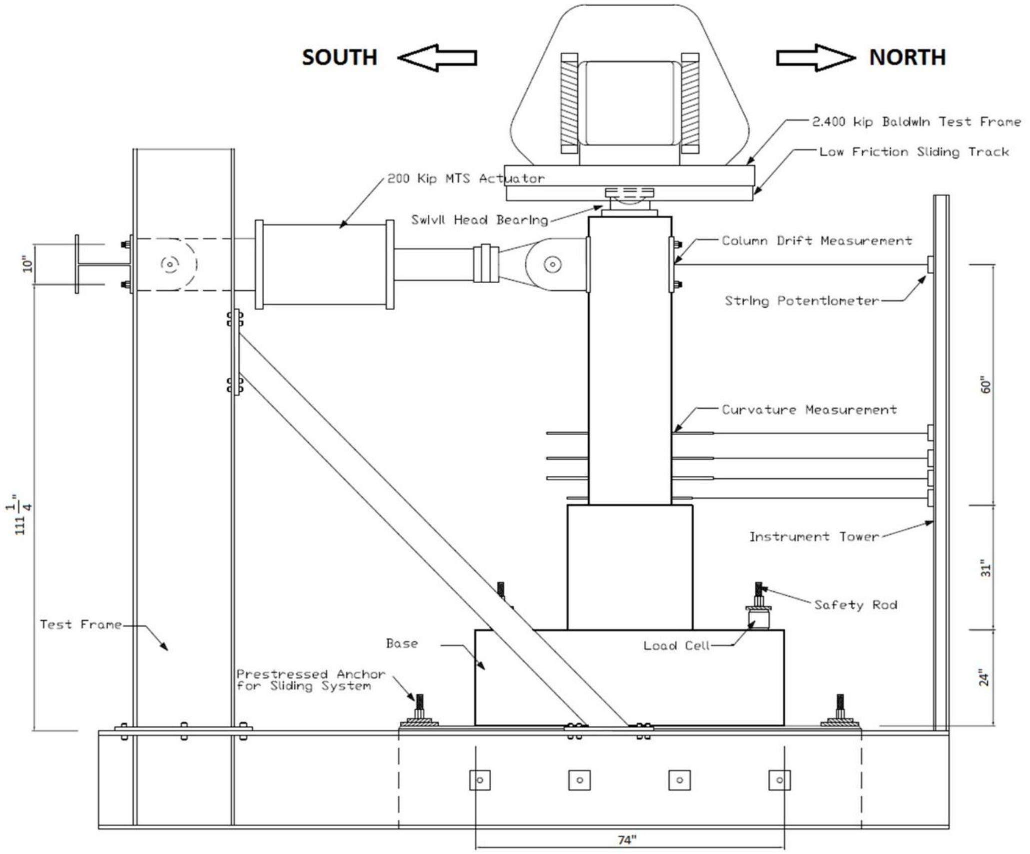

Figure 3-1. Test Setup

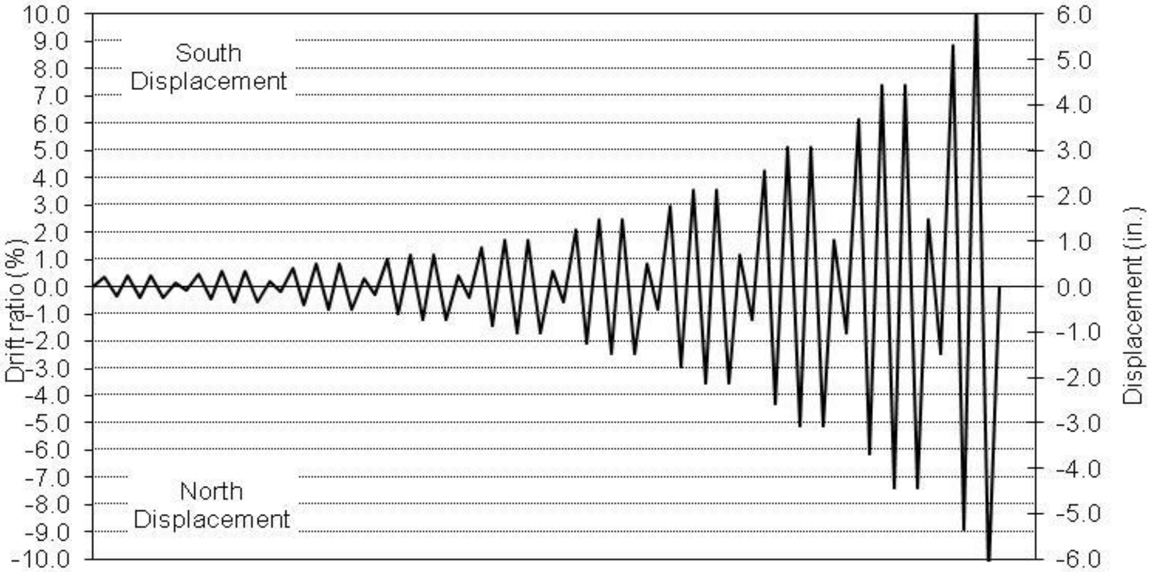

Figure 3-2. Displacement History

Chapter 4

SYSTEM RESPONSE

The moment vs. drift ratio response of specimens DS-1, DS-2, and DS-3 are shown in Fig. 4-1a. In all cases, the yield moment was reached at about 1.5%-2.0% drift ratio. The moment capacity dropped below 80% of the peak value at 7%-8% drift ratio. The responses of specimens DS-1 and DS-3 were very ductile. The peak strengths in Specimen DS-1 was expected because the column were nominally identical previous column-to-spread footing tests (Haraldsson et al. (2011)) and the specimen strength was controlled by the column response.

The damage of connection after testing are shown in Fig. 4-1b. In Specimens DS-1 and DS-3, plastic hinges formed in the column and the mode of failure was column failure as desired. The shaft just had some cracking and damage of the concrete cover at the top of the shaft, but almost strains measured in longitudinal and transverse reinforcement were smaller than the yield strain. In contrast, the plastic hinge did not form in the column in Specimen DS-2.Little spalling occurred in this column during the cyclic test. Instead, the system was damaged by prying failure within the column-shaft connection. The strains measured in the longitudinal reinforcement indicated that there was no bonding failure during testing, as expected.

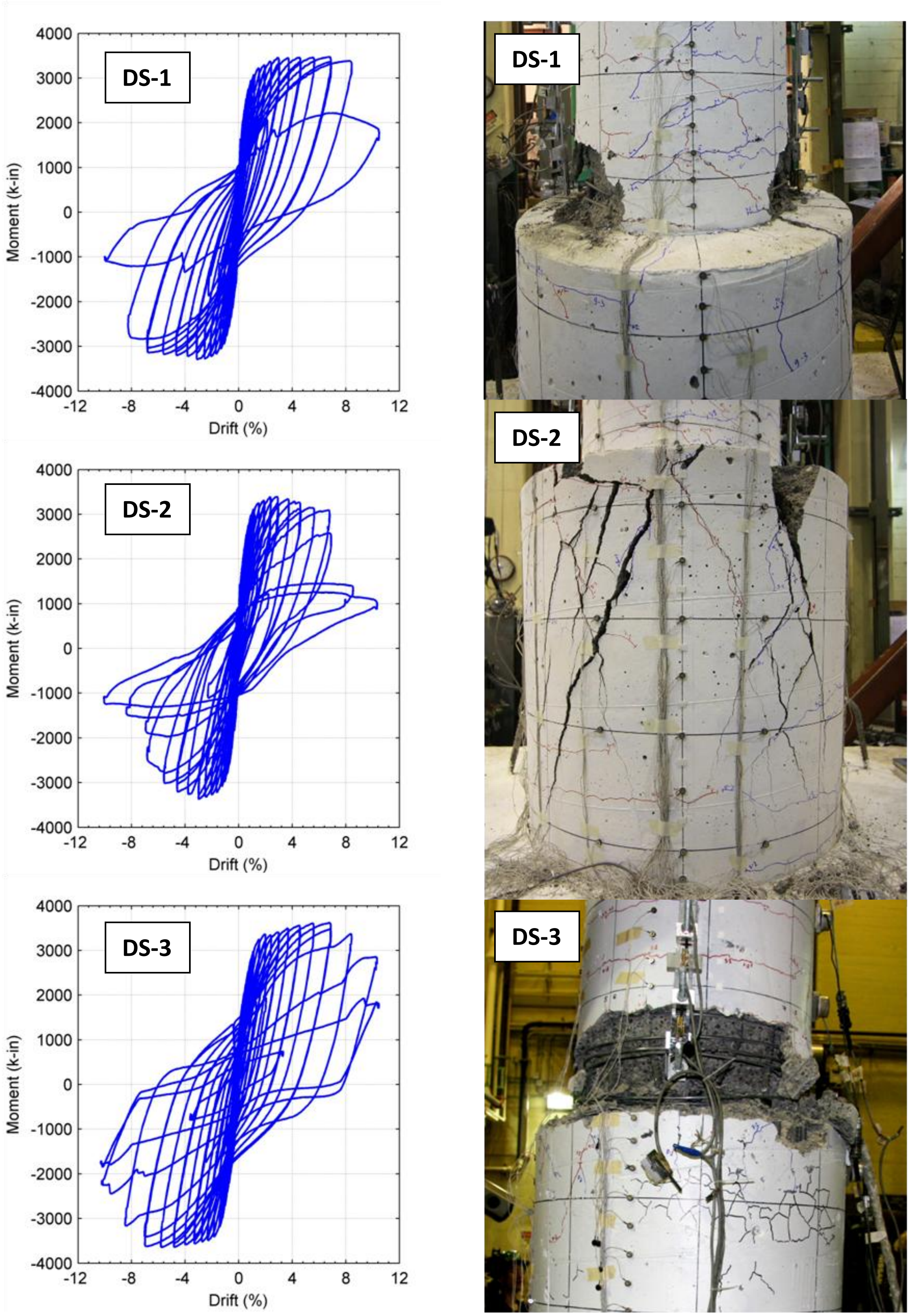

Figure 4-1. a) Moment-Drift Ratio Response b) Damage after testing

Under cyclic loading, the strain gauges attached to the shaft spirals in all three specimens showed that the horizontal strain distributions in the transition spirals were not uniform over the height of the connection. The horizontal strains were largest in the upper part of the transition (Fig. 4-2), they were moderate in the middle of the transition region (Fig. 4-3), and they were almost zero at the bottom of the transition region (Fig. 4-4). In all three specimens, the horizontal strains at the top of the transition exceeded the yield strain of approximately 0.002. In the case of the DS-1 and DS-3, which were designed for k=0.5 and k=0.25, the maximum strains were approximately 50% larger than the yield strains. In contrast, the strain in DS-2 (k=0.25) were much larger, and the shaft spirals eventually fractured, not only at the top, but throughout the length of the transition region.

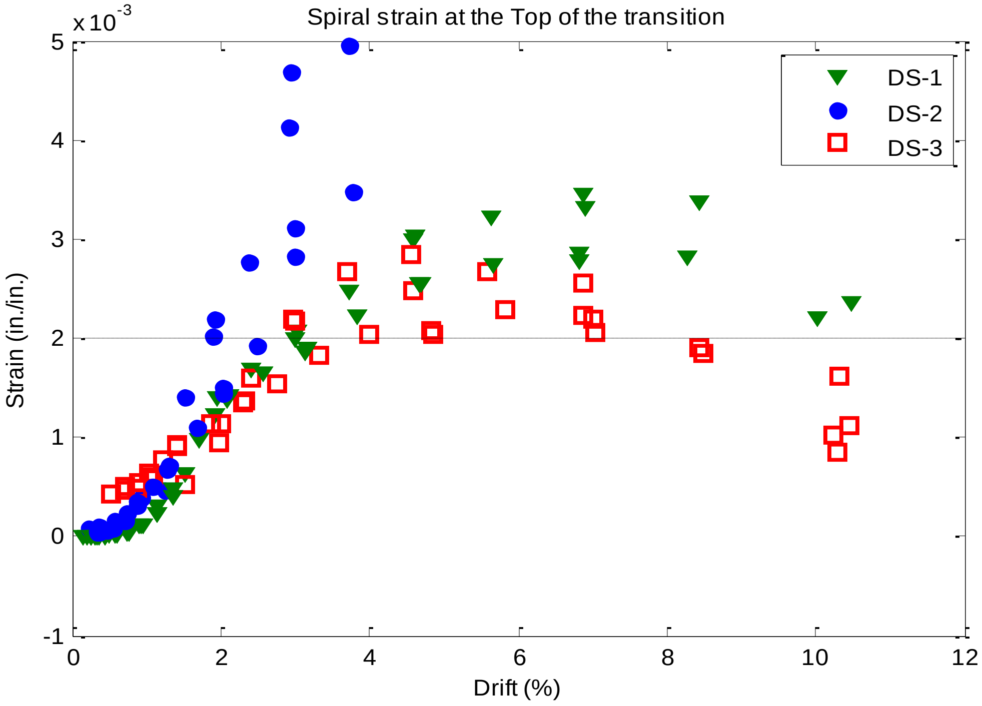

Figure 4-2. Spiral Strain at the Top of the Transition

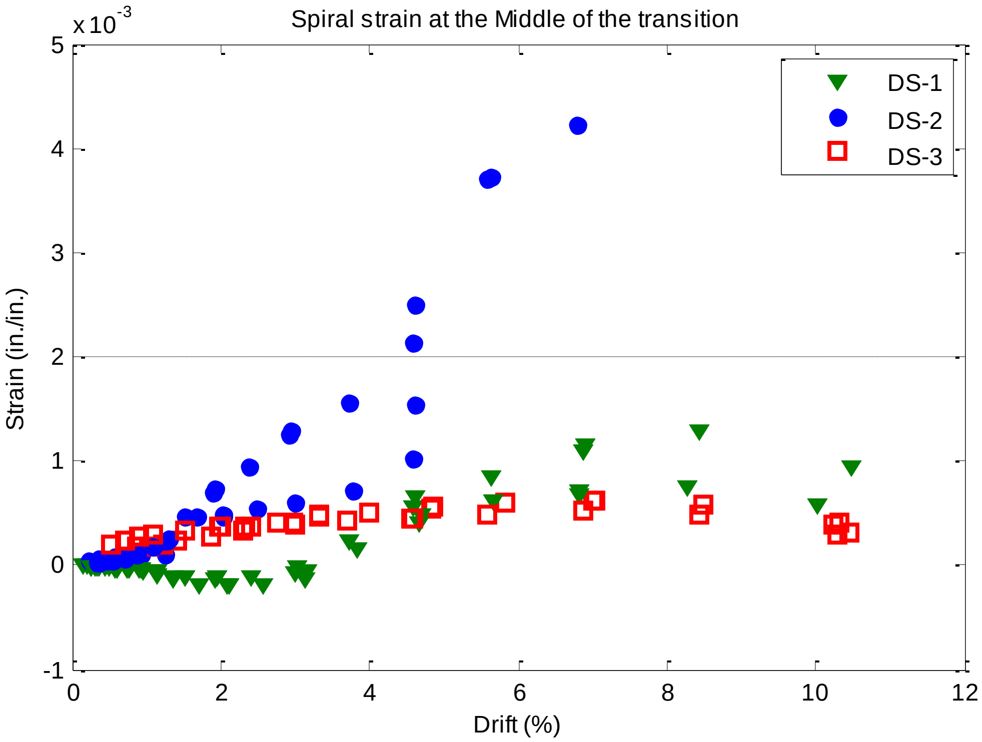

Figure 4-3. Spiral Strain at the Middle of the Transition

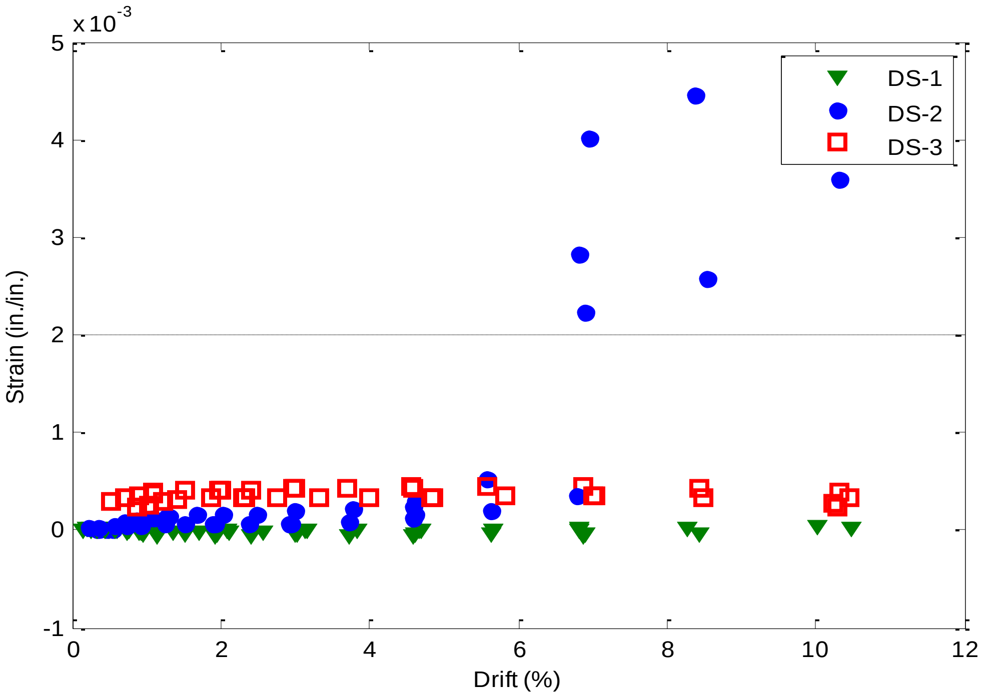

Figure 4-4. Spiral Strain at the Bottom of the Transition

Chapter 5

CONCLUSIONS AND RECOMMENDATIONS

A new type of connection between a precast concrete column and an oversized drilled shaft using “wet” socket connection has been developed. This connection system can accelerate construction and perform well in high seismic regions.

From the results obtained in three tests performed in the University of Washington, the following conclusions can be drawn:

- It is possible to proportion the transverse reinforcement in the transition region to protect the connection and cause failure to occur by plastic hinging of the precast column, as desired. The test specimens had the smallest possible shaft/column diameter ratio, and the shortest possible embedment length, so this conclusion should hold for all permissible shaft and column combinations.
- The spiral strains in the transition region are largest at the top and almost zero at the bottom of the transition. Therefore, it would be more efficient if more spirals are placed in the upper part and fewer spirals are placed in the lower part of the transition region. The spiral strain at the middle of the transition length was nearly yielding in Specimen DS-1 (designed with $k = 0.5$), but was equal as about 50% of yielding strain in Specimen DS-3 (designed with $k = 1.0$). Thus, it suggests that the spirals should be designed with a efficiency factor $k = 1.0$ for the upper part, and $k = 0.5$ for the lower part of the transition to ensure that all spiral will be in elastic region.
- Prying failure of the concrete shell surrounding the precast column will occur if inadequate confinement reinforcement is provided.

REFERENCES

1. “*AASHTO Guide Specifications for LRFD Seismic Design”* (2009). AASHTO, Washington DC.
2. AASHTO (2009). “*LRFD Bridge Design Specifications*” 4th ed., American Association of State Highway and Transportation Officials, Washington, DC.
3. Building Seismic Safety Council for the FEMA. (2004) “*NEHRP Recommended Provisions for Seismic Regulations and for New Buildings and Other Structures (FEMA 450) 2003 Ed.*,” Washington D.C.
4. Haraldsson, O.S., Janes, T.M., Eberhard, M.O., and Stanton, J.F. (2013). “*Seismic Resistance of Socket Connection between Footing and Precast Column.*” Journal of Bridge Engineering, ASCE, Sept-Oct, pp. 910-919.
5. Haraldsson, O. (2011). “*Spread Footing Socket Connections for Precast Columns.*” Master’s Thesis, University of Washington, Seattle, WA.
6. Janes, T. (2011). “*Precast Column Socket Connections for Thin Spread Footings.*” Master’s Thesis, University of Washington, Seattle, WA.
7. McLean, D.I. and Smith C.L. (1997), “*Noncontact Lab Splices in Bridge Column-Shaft Connections,*” Washington State Department of Transportation Report WA-RD 417.1, Olympia, Washington, July.
8. Pang, J.B.K., Steuck, K.P., Cohagen, L.S., Eberhard, M.O. and Stanton, J.F. (2008), “*Rapidly Constructible Large-Bar Precast Bridge-Bent Connection,*” Washington State Department of Transportation Draft Report, WA-RD 684.2, Olympia, Washington, October, 184 pp.
9. Viet Tran, Hung, Stanton, John F., Eberhard, Marc O. (2013), “Precast Bent System for High Seismic Regions: Laboratory Tests of Column-to-Drilled Shaft Socket Connections,” Federal Highway Administration, Publication No. FHWA-HIF-13-038, June.
10. WSDOT BDM (2012). “*Bridge Design Manual (LRFD)*”, Washington State Department of Transportation, Olympia, Washington, August.

PART 3:

CONCRETE FILLED STEEL TUBES FOR ACCELERATED BRIDGE CONSTRUCTION WITH FOCUS ON CONNECTIONS TO PRECAST CONCRETE PIER AND PILE CAPS

Table of Contents

List of Figures

List of Tables

Acknowledgments

The basic funding for the research completed in the past year on imcorporating prior recommendations on CFST design into the AASHTO LRFD bridge design specifications and for developing practical and economical precast concrete connections is provided by PacTrans High Performance Bridge Systems Grant. Additional support for the research described here was provided by the Army Research Laboratory under Cooperative Agreement Number DAAD19-03-2-0036, the California Department of Transportation (CALTRANS) and the Washington State Department of Transportation (WSDOT). The views and conclusions contained in this document are those of the authors and should not be interpreted as representing the official policies, either expressed or implied, of the Army Research Laboratory, the U.S. Government, CALTRANS or WSDOT. The U.S. Government is authorized to reproduce and distribute reprints for Government purposes notwithstanding any copyright notation heron. The authors gratefully acknowledge the financial support of these organizations. In addition, the advice and assistance provided by Ron Bromenschenkel, Michael Cullen, and Peter Lee of the CALTRANS, Bijan Khalighi of WSDOT and Jon Tirpak of the Advanced Technology Institute and the Vanadium Technology Partnership..

Chapter 1

INTRODUCTION

Circular concrete filled steel tubes (CFST) are practical structural elements that have had wide use in Asia but limited use in US bridge construction. CFSTs are economical, have superior engineering properties, and permit rapid construction. The steel tube serves as formwork and reinforcement to the concrete fill, negating the need for placing flexible reinforcing cages, shoring and disposable formwork. The placement of the concrete fill may be further enhanced using self-consolidating concrete (SCC) so that vibration is not required; without interior reinforcement concrete placement is further facilitated. The deformation capacity of the CFST member is increased by the composite action of the concrete fill with the thin, ductile steel tube, and greater stiffness for a given member diameter and material. The fill also increases local and global buckling resistance by stiffening the walls of the tube and decreasing the member slenderness.

CFST are composite members and shear stress transfer must occur between the steel and concrete to ensure full composite action (1, 2). In addition to its inherent flexural and axial strengths, the steel tube provides optimal confinement and greater shear strength than spiral reinforcing, typically used for circular reinforced concrete columns. CFST is clearly most efficient under combined loading (axial plus flexure). Because CFST provides high axial load carrying capacity, they are suitable for bridge piers, piles and drilled shaft foundations.

The current American Association of State Highway and Transportation Officials (AASHTO) LRFD (3) specifications permit the use of CFST construction, but the current provisions have been essentially unchanged for 25 years and do not reflect the extensive research and development that have occurred in the intervening period. This report will briefly review those existing provisions; summarize the vast amount of research completed on CFST; and present proposals for economical and efficient design of CFST members for rapid and economical construction of bridges.

This research is focused on developing design provisions for the use of CFST bridge piers and drilled shafts with focus on connections between the CFST members and pier and pile caps and the work progressing in the past year. This research has been completed with funding from multiple courses, and the report provides an overview of research provided to date with a focus on the work completed during the past year.

Chapter 2

CFST DESIGN PROVISIONS

While CFST is used infrequently in bridge design, a range of specifications are available for the use of the composite design.

2.1 Current AASHTO LRFD Design Provisions

The AASHTO LRFD Specifications (3) provide design rules for CFST construction. These AASHTO provisions are primarily in Articles 6.9.5 and 6.12.2.

The local stability of the steel tube is provided using a limit of the diameter to thickness (*D/t*) ratio. The limiting value is defined in AASHTO Eq. 6.12.2.3.2-1 as:

$$\frac{D}{t} \leq 2\sqrt{\frac{E}{F_y}} \qquad (2.1)$$

where E and F_y are the elastic modulus and nominal yield stress of steel respectively.

The effective flexural stiffness of a CFST member, EI_{eff}, is defined in AASHTO Eq. 6.9.5.1-5 as:

$$EI_{eff} = E_s I_s + 0.4\left(\frac{A_c}{nA_s}\right) I_s \qquad (2.2)$$

where the subscripts c and s refer to properties of the steel and concrete sections, respectively, n is a tabulated value which approximates the ratio of the modulus of elasticity for the steel and concrete, and I and A are the moment of inertia and area of the respective material sections.

The maximum compressive resistance, P_o, of a CFST member is the summation of the yield capacity of the steel tube and the compressive capacity of the concrete fill as defined in AASHTO Eq. 6.9.5.1-4 as:

$$P_o = 0.85f'_c A_c + F_y A_s \tag{2.3}$$

where f'_c is the compressive strength of concrete and other variables have been defined previously. The member buckling capacity, P_{cr}, is based on conventional steel buckling equations as given in AASHTO Eqs. 6.9.5.1-1 and 6.9.5.1-2 and Eq. 4.

$$P_{cr} = 0.658^{\frac{P_o}{P_e}} P_o \quad for\ stocky\ columns \tag{2.4a}$$

$$P_{cr} = 0.877 P_e \qquad for\ slender\ columns \tag{2.4b}$$

(Note that the above equations look a bit different than the equations appearing in the LRFD Specification, because internal reinforcement is not included and some terms have been combined for comparison in later discussion).

The flexural resistance of a CFST member is based on the *D/t* ratio of the section as well as the material properties of the steel tube and is defined in AASHTO Eqs. 6.12.2.3.2-1 and 6.12.2.3.2-2 as:

$$M_n = M_{ps}\ for\ \frac{D}{t} \leq 2\sqrt{\frac{E}{F_y}} \tag{2.5a}$$

$$M_n = M_{yc}\ for\ \frac{D}{t} > 2\sqrt{\frac{E}{F_y}} \tag{2.5b}$$

where M_n is the nominal moment capacity of the CFST, and M_{ps} and M_{yc} are the plastic and yield moment capacity of the steel tube respectively.

Combined loading is an important design consideration because CFST are commonly used under combined compression and bending. The current AASHTO LRFD provisions employ a bilinear axial load-bending moment interaction (P-M interaction) curve used for steel members. This relationship is defined in AASHTO Eqs. 6.9.2.2-1 and 6.9.2.2-2 as:

$$\frac{P_u}{2.0P_r} + \left(\frac{M_{ux}}{M_{rx}} + \frac{M_{uy}}{M_{ry}}\right) \leq 1.0\ for\ \frac{P_u}{P_r} < 0.2 \tag{2.6a}$$

$$\frac{P_u}{P_r} + \frac{8.0}{9.0}\left(\frac{M_{ux}}{M_{rx}} + \frac{M_{uy}}{M_{ry}}\right) \leq 1.0\ for\ \frac{P_u}{P_r} \geq 0.2 \tag{2.6b}$$

where the subscripts x and y correspond to the direction of loading, M_u and M_r are the flexural moment demand and resistance respectively, and P_u and P_r are the axial load demand and resistance.

2.2 Current AISC CFST Design Provisions

The American Institute of Steel Construction (4) also provides design guidelines for CFST construction in Chapter I of the 2010 Steel Construction Manual. The local stability of the steel tube is provided using a *D/t* ratio limit provided in AISC Table I1.1A. This limit is defined as:

$$\frac{D}{t} \leq 0.15\frac{E}{F_y} \tag{2.7}$$

The effective flexural stiffness of CFST is defined in AISC Eq. I2-12 as:

$$EI_{eff} = E_s I_s + C_3 E_c I_c \tag{2.8a}$$

$$C_3 = 0.6 + 2\left[\frac{A_s}{A_c + A_s}\right] \leq 0.9 \tag{2.8b}$$

The maximum compressive capacity of a CFST member is defined in AISC Eq. I2-9b as:

$$P_o = C_s f'_c A_c + F_y A_s \tag{2.9}$$

where the coefficient C_3 is taken as 0.95 for circular CFST in recognition of the confinement provided by the steel tube. The member buckling capacity is calculated using the steel buckling equations defined in Eq. 4.

The flexural resistance of a CFST member is based on the *D/t* ratio of the section as well as the material properties of the steel tube and is defined in AISC Eqs. I3-3a and I3-3b as:

$$M_n = M_p \; for \; \frac{D}{t} \leq 0.15 \frac{E}{F_y} \qquad (2.10a)$$

$$M_n = M_p - \left(M_p - M_y\right)\left(\frac{\lambda - \lambda_p}{\lambda_r - \lambda_p}\right) for \; \frac{D}{t} > 0.15 \frac{E}{F_y} \qquad (2.10b)$$

where M_p is the plastic moment capacity of the composite section, M_y is the yield moment of the steel tube, and λ, λ_p, and λ_r are slenderness ratios determined from AISC Table I1.1b.

AISC permits the use of plastic stress distribution or strain-compatibility methods described in Section I1.2 to calculate combined axial-flexural resistance of CFST. The plastic stress distribution method (PSDM) assumes that the section develops the full yield stress of the steel in tension and compression and a uniform compressive stress of $0.95f'_C$ for concrete over the full compression region, as illustrated in Fig. 1a. The 0.95 coefficient on f'_C is larger than the 0.85 typically used for a Whitney stress block calculation in recognition of the concrete confinement provided by a circular CFT. For each neutral axis depth, pairs of axial and bending resistances are determined by satisfying equilibrium over the cross section for the given stress distribution as illustrated in Fig. 1a. This calculation results in a material-based axial load-bending moment (P-M) interaction curve.

Sectional analysis or strain-compatibility methods are typically used to compute the resistance of reinforced concrete members. For reinforced concrete components, a maximum concrete compression strain of 0.003 is assumed. The strain profile is constructed for each neutral axis depth, and pairs of axial and bending resistances are determined by satisfying equilibrium, as is illustrated in Fig. 2.1b.

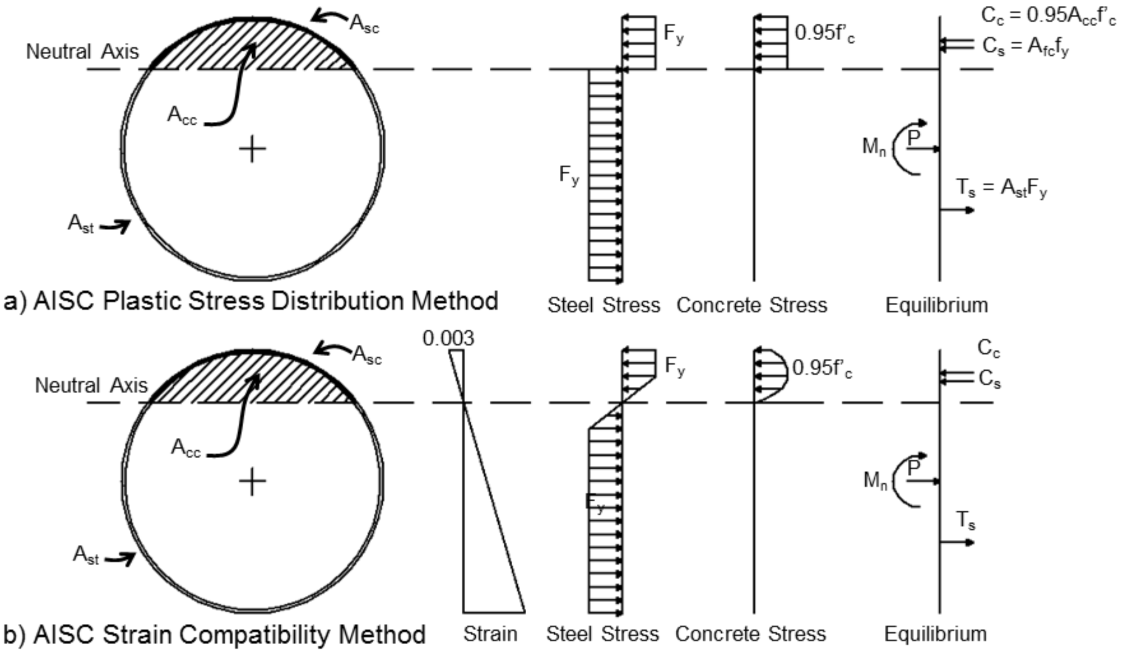

Figure 2.1. AISC model for prediction of CFT resistance**.**

Chapter 3

EVALUATION OF CURRENT PROVISIONS AND PROPOSED REVISIONS

3.1 Evaluation of Current Provisions

A detailed database was compiled for comparison and evaluation of CFST design procedures from 14 test programs and 22 publications, as summarized in Table 1. A wide range of tube diameters D, global slenderness values Kl/r, local slenderness values D/t, and axial load ratios P/P_o were included in this data, as shown in the table. The measured engineering values of interest for these tests are the bending moment and axial load as well as the stiffness. More comprehensive information on each test including the test setup, material properties, and specimen behavior are available elsewhere (5, 6).

Table 3.1 Circular CFT Test Data

Reference	Diameter (in.)	D/t	P/P_0	KL/r	Number of Specimens	Test Information
Boyd, Cofer & McLean (7)	8	73-107	10-14%	32-33	5	Foundation connection
Elchalakani et al. (8)	4 - 4.5	40 - 110	0	-	4	Flexural
Elremaily and Azizinamini (9)	13	34 - 56	20-42%	17-18	6	Beam column
Fujimoto, et al. (10)	6 - 12	34-101	15-80%	9-19	11	Eccentrically loaded column
Furlong (11)	4.5 - 6	36-98	23-63%	21-23	10	Eccentrically loaded column
Han et al. (12)	4 - 8	47-105	0	-	18	Flexural
Lehman and Roeder (13), Kingsley (14), Chronister (15), Williams (16), and Lee (17)	20 - 30	80 - 120	9 - 21%	23-24	19	Foundation connection
Marson and Bruneau (18)	12.5-20	43-74	19-33%	33-44	4	Foundation connection
Morino et al. (19)	9.5	27-53	40-70%	16-25	12	Beam column
O'Shea and Bridge (20)	6.5-7.5	59-226	78-86%	23-26	6	Flexural
Prion and Boehme (21)	6	89	15-82%	21-39	16	Beam column
Thody (22)	20	80	0	-	6	Flexural

Wheeler and Bridge (23)	16-18	63-72	0	-	6	Flexural
Zhang et al. (24)	13.5	57-110	29-59%	28-30	12	Foundation connection

3.1.1 Diameter to Thickness Ratio (D/t)

The experimental database was used to evaluate the influence of the AISC D/t limit on the flexural resistance of CFST. Fig. 3.1 shows the ratio of the measured to the computed flexural resistance of a CFST member as a function of the ratio of the local slenderness of the tube normalized by the AISC slenderness limit. It can be seen that CFST specimens which meet the AISC slenderness limit achieve and exceed the computed resistance.

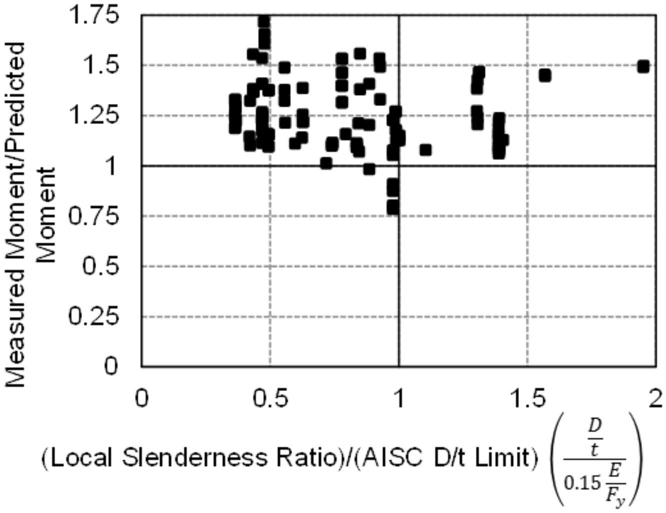

Figure 3.1 Effect of the D/t slenderness limit on moment resistance of CFST.

3.1.2 Effective Stiffness

The expression for EI_{eff} provided in the AISC provisions (Eq. 7 above) were compared with the measured data. The average ratio of the measured -to -predicted flexural stiffness ratio was 0.57 for specimens with no axial load and 0.87 for specimens with axial load. This trend is logical because experimental data shows that the flexural stiffness increased with increased compressive load, because a larger portion of the concrete contributed to the stiffness with increased compression (6). To simulate this effect, a modified stiffness equation was proposed:

$$\mathrm{EI_{eff}} = \mathrm{E_s I_s} + \mathrm{C' E_c I_c} \tag{2.1a}$$

$$\mathrm{C'} = 0.15 + \frac{\mathrm{P}}{\mathrm{P_o}} + 2\frac{\mathrm{A_s}}{\mathrm{A_s}+\mathrm{A_c}} < 0.9 \tag{2.1b}$$

where C' defines the contribution of the gross stiffness, I_c, of the concrete. This approach results in an accurate prediction of the flexural stiffness, with a mean of the measured to predicted stiffness of 1.0.

Axial Load

Comparison to the experimental database showed that the buckling expressions defined in AISC and AASHTO accurately and reliably predict axial capacity of CFST members (25). Both the AISC and AASHTO equations (Eq. 2.9) require EI_{eff}. Use of the proposed flexural stiffness defined in Eq. 2.11 was found to result in accurate axial load capacities.

3.1.3 Combined Loading

The AASHTO provisions neglect the strength of concrete and therefore provide an extremely conservative estimate as to the combined P-M resistance of CFST members. This study evaluated the two AISC procedures for predicting the combined loading resistance of CFST. Both resulted in conservative estimates of resistance. In general, the plastic stress distribution method was easier to use and had a mean value closer to 1 and a lower coefficient of variation than the strain compatibility method (e.g., 6, 18). To illustrate and amplify this conclusion, Fig. 3.2 provides comparisons between the measured moment resistance and the computed moment resistance with the plastic stress distribution method (Fig. 3.2a) and the strain compatibility method (Fig. 3.2b). Fig. 3.2 shows that PSDM is more reliable and somewhat conservative. The strain compatibility method had a much larger average and standard deviation values indicating less reliability and greater conservatism in the method.

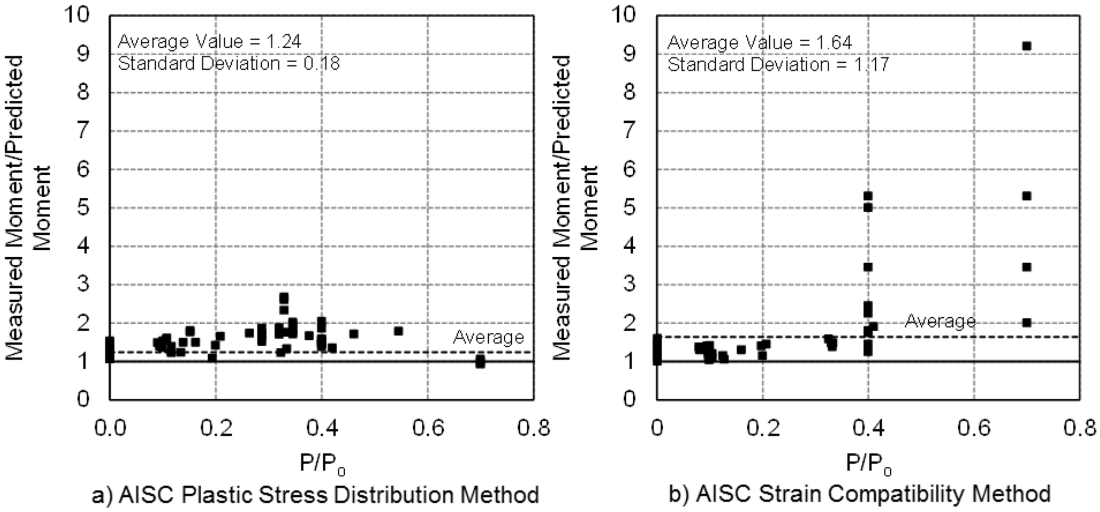

a) AISC Plastic Stress Distribution Method

b) AISC Strain Compatibility Method

Figure 3.2 Comparison of plastic stress distribution and AISC strain compatibility method to experimental results.

The AASHTO resistance prediction is more conservative than both the AISC plastic stress distribution and strain compatibility methods. This conservatism is illustrated in Fig. 3.3, which plots the P-M interaction diagram specified in the current AASHTO provisions as well as the P-M interaction diagram developed using the AISC PSDM for a CFST with D = 60-in. and t = 0.25-in. In example, consider a case in which an axial load of 2500-kips is applied to the given CFST member (plotted using the grey dashed line in Fig. 4). The current AASHTO interaction diagram limits the flexural capacity of the member to 87000kip-in., while the AISC PSDM predicts a flexural capacity of 185000kip-in. As is illustrated by this example, the AASHTO interaction diagram provides a severely conservative estimate of the capacity of this CFST member in comparison to that predicted by the AISC method which was shown to be conservative as well (Fig. 3.2a).

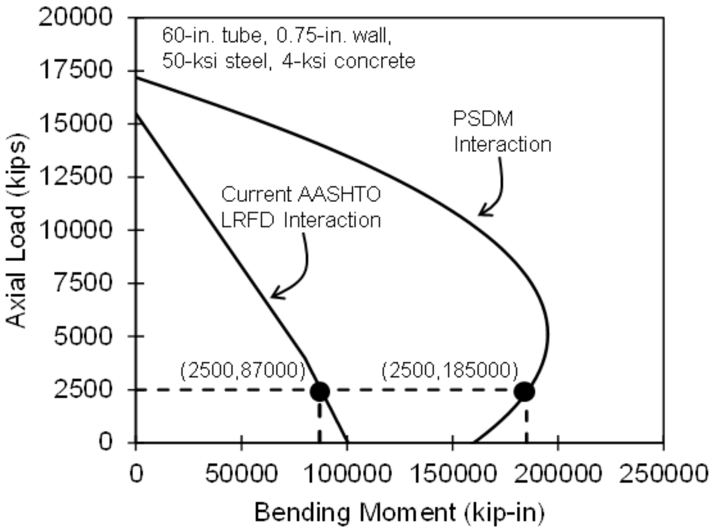

Figure 3.3 Comparison of current AASHTO interaction curve to plastic stress distribution method.

3.2 Proposed Revisions

Proposed draft provisions have been developed for consideration for adoption into the AASHTO LRFD Specification. The draft provisions are proposed as a revision to Article 6.9.5.

The major aspects of the design of CFST as proposed for the provisions are:

1. Slenderness Limitations. The proposed D/t limit is the same as the current AISC (Eq. 6).
2. Effective Flexural Stiffness. EI_{eff} is important in defining buckling and stability effects as well as estimating deflections and deformations. The method used in Eq. 11 is proposed because it is reliable.
3. Buckling and Stability. The buckling and stability limits follow the current AASHTO LRFD provisions expressed in a format consistent with the AISC provisions (Eq. 9).

4. Combined Loading. The PSDM and strain compatibility methods are permitted to compute resistance under combined loading. The PSDM provides greater accuracy and reliability. Closed form equations for this method are included in the proposed revisions.

Chapter 4

CONNECTIONS TO CFST BRIDGE PIERS

4.1 Foundation Connections for CFST

CFST offers many advantages in rapid construction and improved structural performance, but connections between CFST and other structural components are often different and more complex than those used in steel or reinforced concrete construction because of the composite nature of CFST. A foundation connection which develops the full plastic moment capacity of the CFST has been developed as is shown conceptually in Fig. 4.1. When properly designed, this connection provides large inelastic deformation capacity during seismic loading as illustrated by the hysteresis in Fig. 4.2b (13). The connection employs a flange or annular ring that is welded to the base of the steel tube with a complete joint penetration (CJP) or fillet welds that develop the tensile strength of the tube. The ring permits continuity of the concrete fill of the CFST pier with the foundation, and assures attachment and support for the tube and concrete fill during placement and construction. The flange projects out from and penetrates into the tube to interlock the CFST column with the foundation or cap and to provide blocking and binding with the fill and foundation. Internal shear connectors, dowels, or reinforcement are not required. The embedded tube and annular ring provide the force and moment transfer as is illustrated by the compression struts in Fig. 4.1a. The foundation or pile-cap is designed to normal depth, design loads, and shear and flexural reinforcement.

Two variations of the embedded connection have been proposed, as shown in Fig. 4.1. A monolithic version of the connection directly embeds the annular ring and tube into the foundation, permitting simultaneous casting of the CFST and footing, as shown in Fig. 4.1b. For the second variation, the footing is cast with a recess formed by light gauge corrugated metal pipe (with inside diameter that is slightly larger than the outside diameter of the annular ring) for later placement of the tube and annular ring as illustrated in Fig. 4.1c. The tube is placed into the recess after the foundation is cast, and the recess is filled with readily available high strength low shrinkage plastic fiber reinforced grout. Detailed information regarding the grout and fiber properties as well as mixing procedures are provided in reference material (14, 16, 17). For both options, the steel tube is filled with low shrinkage self-consolidating concrete to complete the CFST member and connection, and no vibration of the concrete is required (13).

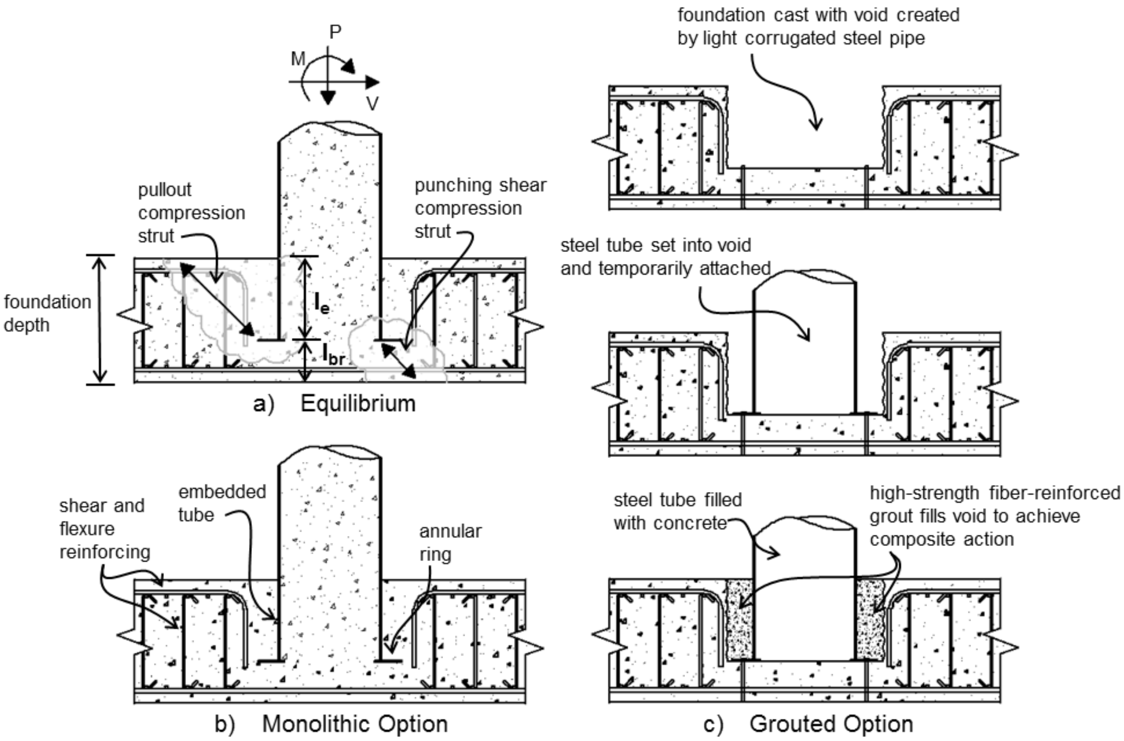

Figure 4.1 Proposed foundation connection.

Nineteen large scale CFST piers with the embedded foundation connection were tested at the University of Washington. (13). As the testing program was so large, only the hysteretic performances of selected specimens are discussed here to demonstrate the influence of tube embedment depth on connection behavior. The moment drift behaviors of an inadequately and adequately embedded specimen are shown in Fig. 4.2, while typical behaviors and failure modes are shown in Fig. 4.3. In summary, the ductility of inadequately embedded connections was ultimately limited by foundation damage due to a conical pullout of the CFST from the foundation, as shown in Fig. 4.3a. In general, the failure mode of adequately embedded connections was characterized by ductile tearing of the steel tube which initiated as a result of local tube buckling as is illustrated in Fig. 4.3d. Furthermore, adequately embedded specimens exhibited a minimal decrease in resistance as a result of severe local buckling which generally initiated at around 4% drift, and had virtually no foundation damage at the end of testing as is shown in Fig. 4.3b. The drift levels achieved by the adequately embedded specimens at failure are significantly larger than those observed from similar size reinforced concrete pier and column base connections.

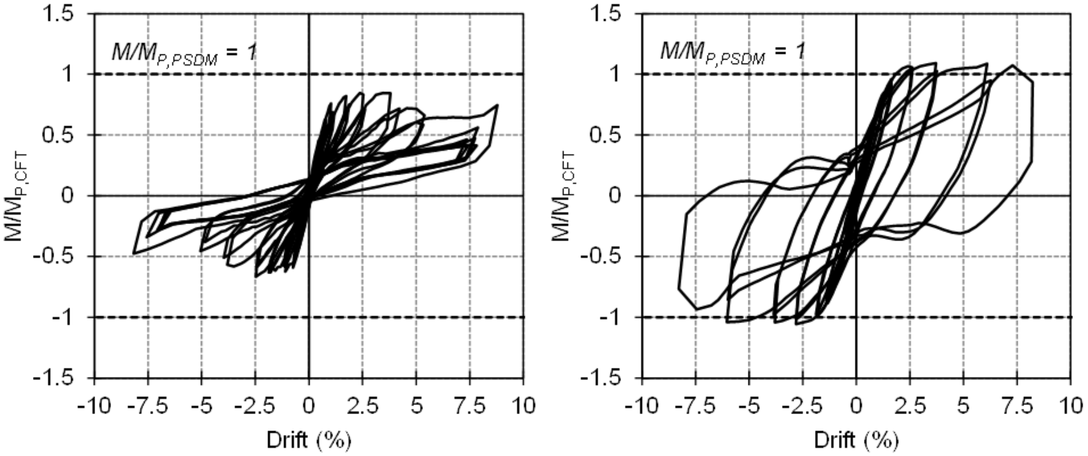

a) Specimen with Inadequate Embedment

b) Specimen with Adequate Embedment

Figure 4.2 Moment rotation plots**.**

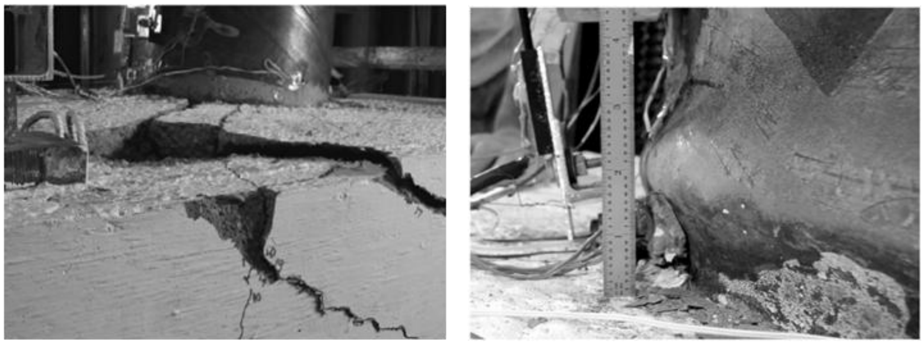

a) Footing Damage Due to Shallow Embedment

b) Footing at End of a Test with Adequate Embedment

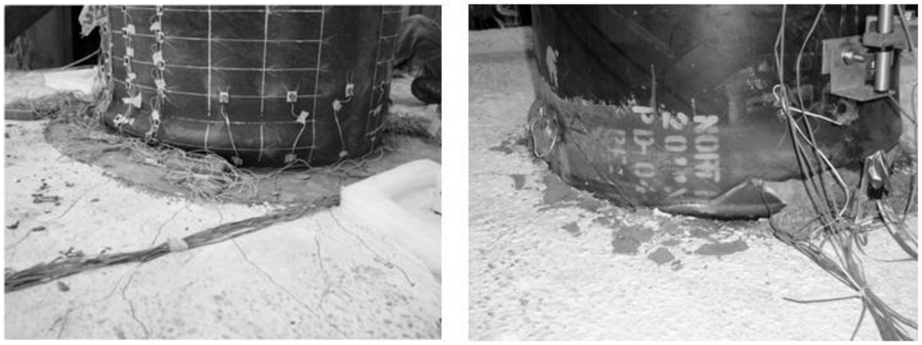

c) Local Buckling at Large Inelastic Deformation

d) Ductile Tearing of Tube in Local Buckling Region

Figure 4.3 Photos of CFST pier connection behavior.

The experimental results were used to develop design expressions for a CFST column-to-foundation connection capable of transferring the full moment capacity of the CFST. Specifically, expressions were developed to dimension and detail the annular ring, determine the required embedment depth, l_e, of the tube to eliminate the conical pullout failure mode, and to determine the required depth of concrete below to the tube, l_{br}, to prevent concrete punching failure (see Fig. 6a). These expressions are not discussed here for brevity; however detailed explanations are available in (13).

4.2 CFST to Pier Cap Connection

The experimental testing of the CFST column-to-foundation connection provided unique and valuable data and design expressions to support the use of CFST columns in bridge construction. Full realization of the system, however, requires development of a range of connections to the cap beam. This connection offers additional challenges including congested joint reinforcement and constraints on cap beam width and height, which are parameters that have not been thoroughly investigated. In addition, optimizing accelerated bridge construction requires exploring use of precast element in the construction of the superstructure. In an effort to meet these diverse requirements, the continuing phase of this research program includes investigation of the CFST column-to-cap beam connection.

Several CFST column-to-cap beam connections are proposed, as shown in Fig 4.4. Fig. 4.4a shows a fully restrained moment connection, which is similar to the CFST column-to-footing connection described above. This connection uses the recessed connection, with a void into a precast inverted-t beam (as shown; note an RC cap beam can also be utilized). The tube is placed in the void after the precast cap beam is placed, and the recess between the tube and corrugated pipe is filled with high strength fiber reinforced grout. The connections shown in Fig. 4.4b and Fig. 4.4c are partial strength connections in which reinforcing bars are developed into the CFST and the cap beam. The longitudinal reinforcing ratio will be less than the effective reinforcing ratio of the CFST and therefore the full CFST strength will not be developed. These bars provide the axial, moment and shear transfer. These connections could be integrated into a precast inverted-t cap beam using ducts or a void similar to that proposed for the embedded connection.

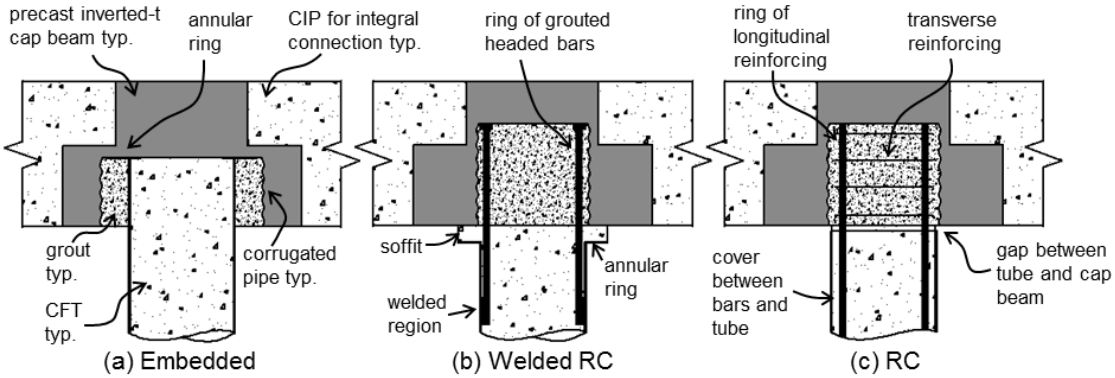

Figure 4.4 Proposed CFST pier cap beam connections**.**

A preliminary series of nonlinear analyses were performed on the cap beam connections shown in Fig. 4.4a and Fig. 4.4b using the commercially available finite element analysis software ABAQUS. Only a brief description of the model is included here; however a detailed overview can be found in (25). An overview of the numerical model is shown in Fig. 4.5a. Model geometry included the CFST-to-cap connection, the CFST, the reinforced concrete cap beam, and two longitudinal girders. The cap beam, longitudinal girders, and deck were reinforced according to provisions in the 2010 Caltrans Seismic Design Criteria (26). A half model was developed taking advantage of symmetry in the plane parallel to the direction of loading and the center of the specimen; this increased computational efficiency. The end nodes at the top of the cap beam were fully restrained to simulate the boundary conditions of future experimental tests, and lateral loading was applied by assigning displacements Δ_x along the x-axis to the top nodes of the concrete fill and steel tube. The loading direction was parallel to the longitudinal direction of the bridge as this was determined to be the critical direction. A constant axial load of $0.1P_o$ was applied to the bottom of the column.

The 4-node shell element with reduced integration (S4R), 2-node truss element (T3D2), and 8-node solid element with reduced integration (C3D8R) were used to model steel tube, reinforcing steel, and concrete elements, respectively. Gap elements were used at every nodal point that was geometrically common between the steel tube and concrete fill elements to simulate bond stress between the concrete by combining the confining contact stress with a coefficient of friction to develop shear stresses at the interface; penetration of the concrete element by the steel element was prevented. The reinforcing steel and concrete components in the footing were spatially assembled, and interactive constraint relationships were defined using the ABAQUS Embedded constraint to perfectly embed the reinforcing bar in the concrete. This constraint does not allow for relative slip between the reinforcing bar and concrete components.

Moment drift relationships for the embedded and welded RC connection are plotted in Fig. 4.5b and Fig. 4.5c. Both connection types exceeded the theoretical moment capacity of the CFST with little strength degradation through 5% drift. This suggests that these connections can achieve strength and ductility performance objectives within the geometry and reinforcing constraints of the cap beam.

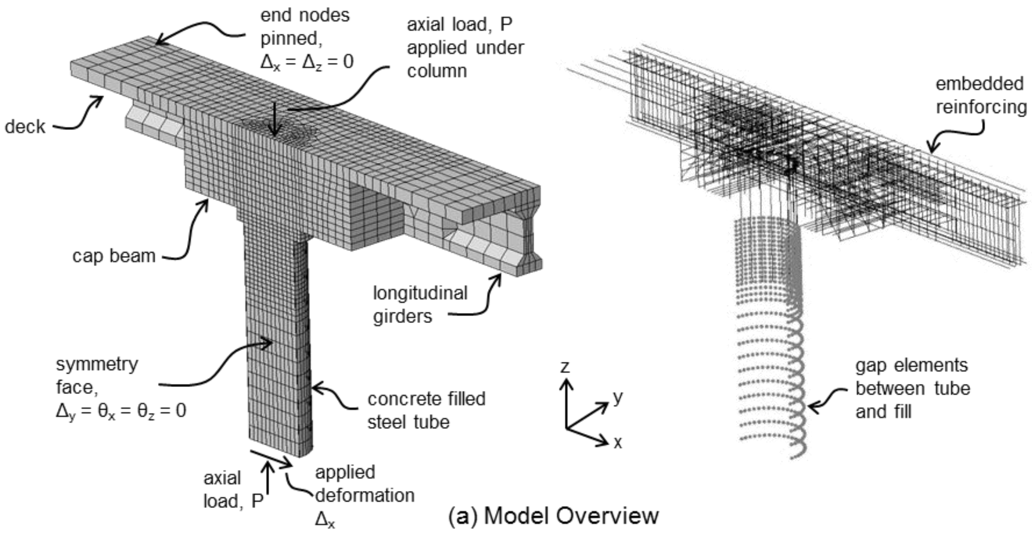

(a) Model Overview

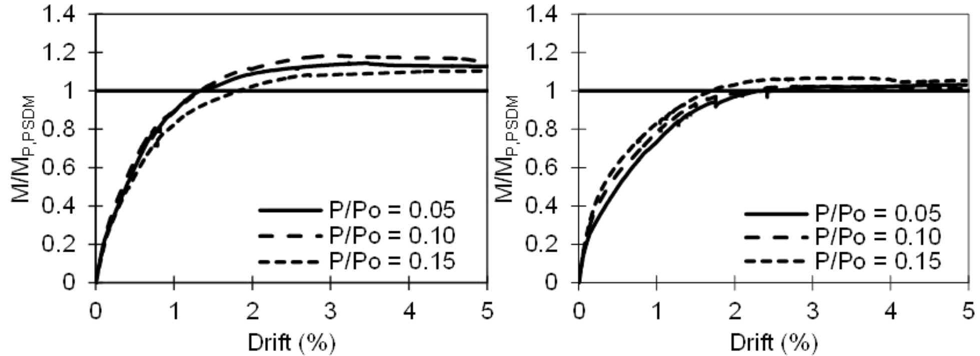

(b) Embedded Connection

(c) Welded RC Connection

Figure 4.5 (a) Cap beam numerical model overview and (b) moment drift relationships for the embedded and welded RC connection.

4.3 Future Work

During the coming year experimental research to follow up analytical studies described in the previous section will be undertaken to substantiate or refute conclusions drawn from the analysis. In addition, these experiments will provide for calibrating and improving the analytical models and further advancing the understanding of CFST performance. Further work will also continue toward improving current AASHTO CFST design provisions and toward adopting these research recommendations into professional practice.

Chapter 5

SUMMARY AND CONCLUSIONSS

CFST construction represents a practical, efficient, and effective construction method for various structural applications, including bridges. It permits rapid construction, because the steel tube is placed quickly, serves as formwork and reinforcement, eliminates the need for shoring, and facilitates placement of the concrete. Further, it is economically efficient because of: 1) the optimum location of the steel in the cross section, 2) excellent and uniform confinement of the concrete provided by the steel tube, 3) restraint of spalling of the concrete by the circular steel tube, and 4) the restraint provided by the concrete to limit local buckling of the tube.

The report provides evaluation of geometric, stiffness and strength expressions for optimization and design of CFST sections. The proposed limit on the D/t ratio is intended to ensure the full plastic section capacity can be achieved. Current design provisions provide very different predictions for the flexural stiffness, EI_{eff}, of circular CFST. Tests show that this flexural stiffness depends on the axial compressive load and a modified stiffness model was evaluated and is proposed for use in design. The axial capacity of the section is computed using the sectional properties and the member stability including geometric nonlinearities. The capacity of the CFST under combined loading can be computed using one of two methods, the plastic stress distribution method (PSDM) or the strain-compatibility method. Evaluation of the two methods indicates that the PSDM provides a more reliable method for estimating the expected moment capacity with the actual capacity results is 1.24 times the predicted moment capacity for any given compressive load.

A proposed revision to the AASHTO LRFD specification is discussed. The major provisions in these draft articles are summarized.

Finally, different embedded and reinforced connections were proposed and evaluated to connection CFST columns to both foundations and cap-beam components. The foundation connections were evaluated experimentally, which has resulted in robust design expressions. The cap beam connection development is preliminary but nonlinear analyses show that they are promising the meet the engineering performance and design objectives.

REFERENCES

11. Roeder, C.W, Lehman, D.E., and Thody, R. (2009) "Composite Action in CFT Components and Connections," AISC, *Engineering Journal*, Chicago, IL (*approved for publication*)
12. Roeder, C.W., Cameron, B., and Brown, C.B., (1999) Composite action in concrete filled tubes, *Structural Engineering*, ASCE, Vol 125, No. 5, May 1999, pgs 477-84.
13. AASHTO (2012) "AASHTO LRFD Bridge Design Specification," American Association of State Highway and Transportation Officials, Washington, D.C.
14. AISC (2005) "Specifications for Structural Steel Buildings" ANSI/AISC Standard 360-05, American Institute of Steel Construction, Chicago, IL.
15. Roeder, C.W., Lehman, D.E., and Bishop, E. (2010) "Strength and Stiffness of Circular Concrete Filled Tubes," ASCE, *Journal of Structural Engineering*, Vol 135, No. 12, pgs 1545-53, Reston, VA.
16. Bishop, E. S. (2009) "Evaluation of the Flexural Resistance and Stiffness Models for Circular Concrete-filled Steel Tube Members Subjected to Combined Axial-Flexural Loading," a thesis submitted in partial fulfillment of Master of Science in Civil Engineering, University of Washington, Seattle, WA.
17. Boyd, P.F., Cofer, W.F., and Mclean, D.I., (1995) "Seismic Performance of Steel-Encased Concrete Columns under Flexural Loading." *ACI Structural Journal,* Vol. 92, No. 3, pp. 355–364.
18. Elchalakani, M., Zhao, X.L., and Grzebieta, R.H. (2001) "Concrete-Filled Circular Steel Tubes Subjected to Pure Bending," *Journal of Constructional Steel Research*, Vol. 57, pp. 1141-1168.
19. Elremaily, A., and Azizinamini, A. (2002) "Behavior and Strength of Circular Concrete-Filled Tube Columns," *Journal of Constructional Steel Research*, Vol. 8, pp. 1567-1591.
20. Fujimoto, T., Mukai, A., Nishiyama, I., and Sakino, K., (2004) "Behavior of Eccentrically-Loaded Concrete-Filled Steel Tubular Columns," *Journal of Structural Engineering,* Vol. 130, No. 2, pp. 203-212.
21. Furlong, R.W. (1967), "Strength of Steel-Encased Concrete Beam Columns," *Journal of the Structural Division*, ASCE, Vol. 93, No. ST5, pp. 113-124.
22. Han, L.H, Lu, H., Yao, G.H., and Liao, F.Y. (2006) "Further Study on the Flexural Behaviour of Concrete-Filled Steel Tubes," *Journal of Constructional Steel Research*, Vol. 62, pp. 554-565.
23. Lehman, D.E. and Roeder, C.W. (2012) "Foundation Connection for Circular Concrete Filled Tubes," *Journal of Constructional Steel Research,* Vol. 78, November 2012, pgs. 212-25, Elsevier.
24. Kingsley, A. (2005). "Experimental and Analytical Investigation of Embedded Column Base Connections for Concrete Filled High Strength Steel Tubes." a thesis submitted in partial fulfillment of Master of Science in Civil Engineering, University of Washington, Seattle, WA.

25. Chronister, A. (2007). “Experimental Investigation of High Strength Concrete Filled Steel Tubes in Embedded Column Base Foundation Connections.” Unpublished data , University of Washington, Seattle, WA.
26. Williams, T.S. (2006). “Experimental Investigation of High Strength Concrete Filled Steel Tubes in Embedded Column Base Foundation Connections.” a thesis submitted in partial fulfillment of Master of Science in Civil Engineering, University of Washington, Seattle, WA.
27. Lee, J. (2011) “Experimental investigation of Embedded Connections for Concrete Filled Tube Column Connection to Combined Axial-Flexural Loading,” a thesis submitted in partial fulfillment of the degree of Master of Science in Cicil Engineering, University of Washington, Seattle, WA.
28. Marson, J. and Bruneau, M. (2004) “Cyclic Testing of Concrete-Filled Circular Steel Bridge Piers Having Encased Fixed-Base Detail,” *ASCE Journal of Bridge Engineering*, Vol. 9, No. 1, pp. 14-23.
29. Morino, S., Sakino, K., Mukai, A., and Yoshioka, K., (1997) *Experimental Studies of CFT Column Systems – U.S.-Japan Cooperative Earthquake Research*, ASCE, New York, NY, pp. 1106-1110
30. O’Shea, M.D., and Bridge, R.Q., (2000) “Design of Circular Thin-Walled Concrete Filled Steel Tubes” *Journal of Structural Engineering*, Vol. 126, No. 11, pp. 1295-1303
31. Prion, H.G.L., and Boehme, J. (1994) “Beam-Column Behaviour of Steel Tubes Filled with High Strength Concrete,” *Canadian Journal of Civil Engineering*, Vol. 21, pp. 207-218.
32. Thody, R. (2006). “Experimental Investigation of the Flexural Properties of High-Strength Concrete-Filled Steel Tubes.” a thesis submitted in partial fulfillment of Master of Science in Civil Engineering, University of Washington, Seattle, WA.
33. Wheeler, A., and Bridge, R., (2006) “The Behavior of Circular Concrete-Filled Thin-Walled Steel Tubes In Flexure,” *Composite Construction in Steel and Concrete V*, Proceedings of the 5th International Conference, Vol. 39, pp. 412-423.
34. Zhang, G.W., Xiao, Y., and Kunnath, S., (2009) “Low-Cycle Fatigue Damage of Circular Concrete-Filled Tube Columns,” *ACI Structural Journal*, Vol. 106, No. 2, pp 151-159
35. Moon, J., Lehman, D.E., and Roeder, C.W. (2013) "Strength of Circular Concrete Filled Tubes (CFT) with and without Internal Reinforcement Under Combined Loading," *Journal of Structural Engineering*, ASCE, Reston, VA, DOI:10.1061(ASCE)ST1943-541X.000078.
36. Caltrans, (2010) “Seismic Design Criteria Version 1.6,” California Department of Transportation.